Modelling of Mobile-To-Mobile MIMO Channels

by

Ali Chelli

Thesis in partial fulfilment of the degree of
Master in Technology in
Information and Communication Technology

Agder University College
Faculty of Engineering and Science

Grimstad
Norway

May 2007

Abstract

Mobile-to-Mobile (M2M) communications are expected to play are expected to play an important role in various fields including ad hoc networks and intelligent transportation systems. In such systems, extremely reliable links are required. To cope with problems faced during the development and performance investigation of future Mobile-to-Mobile multi-input multi-output (MIMO) communication systems, a solid knowledge of the underlying multipath fading channel characteristics is essential.

This master thesis focuses on the modelling, analysis, and simulation of M2M single-input single-output (SISO) and M2M MIMO channels derived from a geometric street scattering model. Starting from this geometrical model, the corresponding reference and simulation models are derived by applying the generalized concept of deterministic channel modelling. The statistical properties of both the reference and the simulation model are studied with emphasis on the amplitude distribution and the correlation properties, which include the temporal, spatial, and frequency correlation functions. The obtained theoretical results are confirmed by MATLAB simulations.

Preface

This project concludes two years of master study in Information and Communication Technology (ICT) at Agder University College (AUC), Faculty of Engineering and Science in Grimstad, Norway. This project has been carried out from January to June 2007.

I am deeply grateful to my supervisor Prof. Mattihas Pätzold for his guidance and precious advices during the fulfillment of this project.

I would like also to thank the head of Master studies, Mr Stein Bergsmark, and the Master studies coordinator Sissel Andreassen for their contributions.

Ali Chelli

Grimstad, May2007

Contents

List of Figures

List of Tables

Chapter 1

Introduction

According to the World Health Organization report [1], more than one million persons were killed in 2004 due to road crashes. In addition, almost 50 million persons were injured due to the same cause. Moreover, predictions estimate that this statistics will increase by about 65% in the next 20 years. This drastic situation must motivate efforts toward preventive solutions. In fact, car safety became an issue directly after the invention of automobile itself. A big progress has been achieved in this domain since the beginning of car production. Modern cars are obviously much safer then ancient cars. ABS system, airbag, and seatbelt are a necessity in every car today. However, psychological studies have proven that, the safer the car is, the more risky the driver behaviour becomes. On the other hand, the high speed of modern cars makes crashes more dangerous. A close look at the available safety measures reveals that they become affective only after the crash itself. This fact motivates the introduction of new safety systems that prevent from accident rather then minimizing their impact. Such futurist systems are under investigation by many car companies. The principle of such systems consists in detecting accidents threat and sending a warning to the driver. If no action is taken, the safety system takes the necessary measures automatically. For instance, if the car is too near to another vehicle, then there is an accident threat. This threat is detected by the safety system by measuring the distance with neighbouring cars. Afterward, a warning message is sent to the

driver. If the driver does not take the necessary measures, the safety system intervenes to avoid the accident. To enable this new safety system, the car must be able to communicate with other vehicles via inter-vehicle communications system.

1.1 Inter-Vehicle Communications (IVC) State of Art

There is a growing belief that IVC could help people to drive more safely. This fact has motivated industrial and research groups to investigate the IVC technology and the potential applications that could be introduced thanks to IVC. Currently there are several projects in Europe and in the United States focusing on the development of the IVC technology. In the following, we present European and American projects investigating the IVC technology. Moreover, the Dedicated Short Range Communication (DSRC) standard designed for IVC is presented. Finally, the potential applications that could be introduced thanks to IVC are discussed.

1.1.1 European Projects

In the context of the European Transport Policy, the European commission has declared that it aims to reduce road crashes fatalities to 50% by 2010. This target could be reached by embedding safety application in cars. One of the key technologies for the achievement of this objective is IVC. Currently there are several ongoing projects in Europe focusing on the development of IVC technology such as PReVENT, CAR 2 CAR Communication Consortium, FleetNet, ADASE (Advanced Driver Assistance Systems in Europe), and CarTALK 2000. In the following, the PReVENT project and the CAR 2 CAR Communication Consortium are presented.

1.1.1.1 The PReVENT Project

The European research project PReVENT [2] aims to increase road safety. To achieve this goal several technologies are integrated together such as sensing technology, positioning technology (GPS), and IVC technology. The PReVENT project provides drivers with safety applications, which aims to prevent them from crashes or mitigate their effects. Moreover, safety applications help drivers to keep safe distance from the neighbouring cars, to maintain a safe speed, and avoid overtakingin critical situation. The PReVENT systems plan to be interoperable on a European scale.

1.1.1.2 The CAR-2-CAR Communication Consortium

In contrast to the PReVENT project, where IVC is only a part of the picture, the CAR-2-CAR Communication Consortium project is totally devoted to IVC. The latter is used to increase road traffic safety and efficiency. The CAR-2-CAR Communication Consortium [3] was set up by a group of carmakers among them Audi, BMW, Honda, and Renault. The consortium includes also the electronic company Philips.

The CAR-2-CAR communication consortium has a set of objective to achieve. First, this organization aims to set up a European standard for car-2-car communication. A second objective consists in promoting the allocation of an exclusive band for CAR-2-CAR communication. Another mission of the consortium is to push toward worldwide standard interoperability in CAR-2-CAR communication. A major concern is given to standardization and interoperability since CAR-2-CAR applications will yield best benefits to users, only if different CAR-2-CAR communication systems are interoperable.

1.1.2 American Projects

The reduction of road crash fatalities is the top priority of the United States Department of Transportation. In the United States, road crashes kill 115 and injure 8700 every day. The health care given to accident victims has the biggest cost compared to any other cause of illness or injury. In this context, the "Intelligent Transportation System" (ITS) was launched [4]. This national program in the United States has as objective to improve safety by avoiding road crashes. In addition, ITS aims to improve the efficiency of the transportation system by eliminating travel delays. This goal can be achieved using many technologies such as sensing technology, and IVC technology. ITS is supported by the U.S. government through the U.S. Department of Transportation (USDOT) and non-governmental organization such as Intelligent Transportation Society of America (ITS America). The latter has supported intelligent transportation system in the U.S. for more than 15 years. ITS America members are active participant in the deployment of the "Intelligent Transportation System". Moreover, industry groups such as Vehicle Safety Communications (VSC) Consortium are trying to enhance safety and mitigate congestion, by providing safety systems based on IVC technology.

1.1.2.1 **Vehicle Safety Communications (VSC) Consortium**

The VSC Consortium [5] was funded by seven carmakers including BMW, Ford, DaimlerChrysler, General Motors, Nissan, Toyota, and Volkswagen. This consortium cooperates with the U.S. Department of Transportation in the VSC Project. This project has several objectives such as estimating the potential safety application that could be provided based on IVC. In addition, the project aims to identify the communications requirement for the proposed safety applications. Moreover, this project evaluates IVC technology and their ability to meet the needs of safety applications.

A further task of this project is to present suggestions to standardization bodies, focusing on IVC, to make the appropriate changes in order to meet the requirements of safety applications. Furthermore, this project investigates technical problems that may influence the deployment of vehicle safety applications.

1.1.3 The Dedicated Short Range Communication Standard

The Dedicated Short Range Communication (DSRC) standard is designed for IVC. The DSRC is still under development. The first draft specification of DSRC was developed by ASTM [6]. This draft is now under investigation by three IEEE working groups:

- The IEEE 802.11p task group is focusing on the standardization of the Wireless Access for Vehicular Environment (WAVE). This task group focus on the design of the physical layer (PHY) and the medium access layer (MAC) [7].
- The IEEE 1609.4 task group is focusing on multi-channel coordination [8].
- The IEEE 1609.3 task group is focusing on network layer protocols and offered services [9].

The development of DSRC has been motivated by the allocation of 75 MHz of spectrum in the 5.9 GHz band by the Federal Communication Commission (FCC) in the U.S., for intelligent transportation services [10]. The latter aims to provide safety and non-safety application based on vehicle-to-vehicle and vehicle-to-infrastructure communications. These kinds of application are introduced in the context of "Intelligent Transportation System". There is a growing belief that the DSRC standard will dominate the future vehicular communications market. The DSRC is based on IEEE 802.11a Physical layer (PHY). While the DSRC Medium Access Control (MAC) protocol is similar to the IEEE 802.11 standard. One could wonder why the DSRC is

developed in lieu of the DSRC standard. In fact, many reasons have motivated the development of DSRC —versus the IEEE 802.11 standard— to provide IVC.

Actually, the IEEE 802.11 uses an unlicensed band (2.4 GHz or 5 GHz). This band is also being used by the Bluetooth standard. The proliferation of devices working in this band along with the widespread of WiFi technology can cause high interference level. This fact could be very harmful to IVC since the radio link must be extremely reliable. In addition to reliability, safety applications necessitate a short response time. The use of unlicensed band increases the number of users trying to access the communication channel resulting in high latency. This fact makes the IEEE 802.11 standard non-suitable for IVC, especially for safety applications.

Moreover, the IEEE 802.11 was designed for indoor environment where the terminals have a low speed. In contrast, in IVC, the terminals are moving very fast in outdoor environment. In this context, it is also worth to remind that in IVC both the transmitter and the receiver are moving as opposed to the IEEE 802.11 where it is assumed that only the receiver is in motion. All these facts lead to a change in the underlying multi-path radio channel, making the IEEE 802.11 non-suitable for IVC.

The 75 MHz (5.850-5.925) spectrum allocated for DSRC is split into seven 10MHz channels. One channel is dedicated to control while six channels are service channels [6], as shown in Figure.1.1. The channel 180 and 182 are optionally combined to offer 20MHz spectrum for wideband services. The channel 172 is devoted to IVC. The DSRC/IEEE 802.11p PHY uses Orthogonal Frequency Division Multiplexing (OFDM) technique. Some key parameters of DSRC/IEEE 802.11p PHY are illustrated in Table1.1.

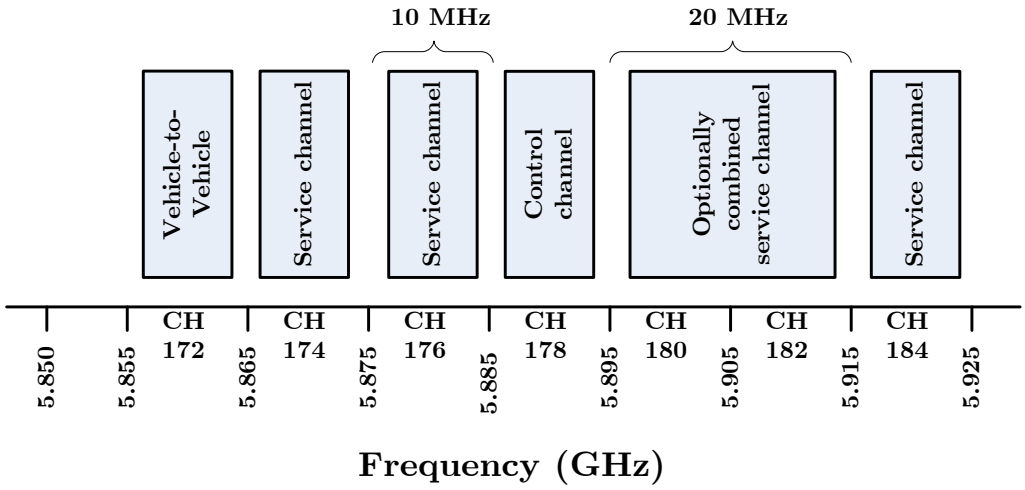

Figure 1.1: Frequency allocation of DSRC/IEEE 802.11p.

Data Rate (Mb/s)	3, 4, 5, 6, 9, 12, 18, 24, 27
Modulation	BPSK, QPSK, 16-QAM, 64-QAM
Coding Rate	1/2, 2/3, 3/4
OFDM Symbol Duration	8μs
Guard Interval	1.6 μs
Subcarrier Spacing	156.25 KHz
Signal Bandwidth	10 MHz

Table 1.1: Key parameters in the DSRC/IEEE 802.11p PHY

1.1.4 Inter-Vehicle Technology Applications

IVC introduces a wide range of applications. These applications could be mainly classified into three categories:

1. Cooperative driver-assistance applications
2. Local floating car data applications
3. User communication and information services

1.1.4.1 Cooperative Driver-Assistance Applications

Cooperative driver assistance systems exploit the sensor data exchanged between cars. The received data can be handled in two ways: either displayed to the driver, or used by the driver assistance application as an input to control the car. For instance, the user can be informed about unexpected obstacle. Thus, he can be prepared to face problems. In addition, the driver assistance application can detect near threat and avoid crashes. For instance, the application can receive a notification on emergency braking from the car ahead. In this case, the application sends a warning to the driver. If no action is taken, the driver assistance application intervenes to avoid collision. This class of application include two types of collision avoidance systems:

- Intersection Collision Avoidance Systems supervise the vehicle speed and its position relatively to the intersection. In addition, the system monitors the speed and position of other vehicles in the neighborhood using IVC technology. In case of imminent collision, the system advises the driver of appropriate actions to avoid the crash. It is worth to mention that one of three accidents is an intersection accident.
- Rear-End Collision Avoidance Systems detect the presence and velocity of cars ahead, and send warnings to the driver in order to avoid collisions. Rear-end collisions represents one-forth of accidents. The National Highway Traffic Safety Administration (NHTSA) in U.S. estimates that this system will lead to a 49 percent drop of rear-end crashes.

Obviously, the driver assistance application contributes efficiently in increasing the travellers' safety.

1.1.4.2 **Local Floating Car Data Applications**

The floating car data service exists today in Europe. This service consists in sending messages about traffic conditions to the subscribed members. This service is characterized by a centralized architecture. In fact, the service centre collects information from cars, treat the data, and broadcast the results to all service members. For instance, if there is traffic jam in a given location, cars present there sends a message to the service centre. The latter broadcast the information. Hence, congestion can be avoided. To achieve this service, a radio cellular transmission system and an expensive service centre are needed. This high cost could be avoided using IVC.

In a two-direction route, cars can receive important information about the road ahead from cars coming from the opposite direction. Cars can even send request to ask about traffic flow in the road ahead. The car that has received information about traffic status, for example, must broadcast this data. In fact, the transmission system for IVC has a limited coverage. Then cars that are interested in given information may be located out of the coverage zone. A Car that has received a message must broadcast it in order to convey information to other cars. This kind of application leads to good performance especially when the penetration of IVC is high.

In order to improve driving safety, the cooperative driver assistance application handles immediate situation by suggesting driving actions. This can be categorized as a short-term decision. In contrast, the local floating car data application handles information related to traffic condition in further distances. This information does not influence directly the car driving, but may lead to a change in the route to go. This decision is considered as a long-term decision.

1.1.4.3 User Communication and Information Services

This class includes all possible applications that run on the top of TCP or UDP protocol. It includes entertainment applications such as online games. For example, passengers on backseat can play online games with passengers in other cars. In addition, IVC technology does not only allow communicating with other vehicles but also with the roadside. This feature could be very useful for the development of various applications. For instance, shops, supermarket, and restaurants that are placed on the road could use this feature to advertise their products and services. Moreover, internet access point could be positioned on the roadside to provide car passengers with internet access.

1.2 Background

In mobile radio, communication, the line-of-sight condition is not often fulfilled due to the obstacles located between the transmitter and the receiver. The transmitted signal undergoes different physical phenomena such as reflection, diffraction, and scattering. These phenomena lead to signal distortion which makes it difficult to retrieve the information in the receiver side. To overcome this problem several techniques are used such as equalization, modulation and coding. For instance, to find out the appropriate coding scheme to be used for a given communication system a detailed knowledge of the underlying fading channel is essential. Therefore, channel modelling is necessary for the design, development, and optimization of any communication system.

1.2.1 Generalized Concept of Deterministic Channel Modelling

In real-world, the received signal is a superposition of waves coming from all directions due to the multipath propagation. This effect is due to an infinite number

of scattering objects. Consequently, an ideal model for this phenomenon cannot be realized since an infinite number of scattering object need to be considered in the simulation. To overcome this problem, different approaches have been proposed in literature. An overview covering approaches to model spatiotemporal channel models is given in [11]. An optical-ray tracing approach is used in [12]. The main drawback of this approach is the high computational effort required in the simulation.

To overcome this complexity the deterministic channel modelling concept has been introduced in [13,14]. Later, the fundamental concept of deterministic channel modelling has been generalized in [15]. The principle of the generalized channel modelling consists in the following six steps:

1. A geometrical scattering model is developed assuming an infinite number N of scatters.
2. Starting from the geometrical scattering model a stochastic reference model is derived.
3. Derivation of an ergodic simulation model from the reference model by using a finite number N of scatters.
4. Derivation of the deterministic simulation model by fixing all model parameters of the stochastic simulation model.
5. Computation of the simulation model parameters by using appropriate computation method, e.g., the Lp-norm method (LPNM).
6. Generation of one (or some few) sample function by using the deterministic channel model with fixed parameters.

1.2.2 Mobile-to-Mobile Channel Modelling

In IVC, the transmitter and the receiver are on the move. This fact makes the statistical properties of the underlying radio channel different from typical cellular channels. Hence, new channel models are required for IVC. So far, Mobile-to-Mobile (M2M) channel modelling has been the topic of several papers. Early studies of M2M channels have focussed on single-input single-output (SISO) systems in [15,16]. The time-varying transfer function of the M2M channel has been developed in [16]. Moreover, analytical expression for the space-time correlation function and the power spectral density (PSD) of the complex envelope are provided in [16]. In [17], analytical expression for the level crossing rate (LCR) and the average duration of fades (ADF) are presented. In [18], a channel model for IVC is presented. A ray-optical approach is used to model wave propagation. The resulting channel impulse response can be used for system simulation. In addition, simulation results are compared to measurements from real-world M2M channels at 5.2 GHz. In [19], a simulation model design procedure for single-input single-output (SISO) M2M channels is introduced. The geometrical two ring scattering model constitutes the starting point in [20] for the derivation of a reference model of a narrowband M2M multi-input multi-output (MIMO) channel. The corresponding simulation model is presented in [21].

1.3 Thesis Definition

In this thesis, an original M2M SISO channel model is investigated. Afterward this model is extended to an M2M MIMO channel model. This extension is driven by the fact that MIMO channels are attracting more and more attention thanks to their large capacity. In fact, MIMO systems employ multiple transmit and multiple receive antennas resulting in better system performance and larger capacity over

traditional SISO channels. Furthermore, multi-element antennas can be placed on car roofs. This fact makes MIMO channels very attractive for IVC. In IVC, both the transmitter and the receiver are moving. This fact makes the statistical properties of the underlying radio channel different from typical cellular channels. Hence, new channel model are required for M2M communications. The latter are expected to play an important role in various fields including ad hoc networks and intelligent transportation systems. In such systems, extremely reliable links are required. To cope with problems faced during the development and performance investigation of future M2M MIMO communication systems, a solid knowledge of the underlying multipath fading channel characteristics is essential.

This master thesis focuses on the modelling, analysis, and simulation of M2M SISO and M2M MIMO channels derived from geometric scattering model. In this model, we assume that the transmitter and the receiver are surrounded by an infinite number of scatters. The scattering environment is modelled by a new street scattering model. For this model, scatters are laying on the right and/or left hand side of the street.

Starting from this geometrical model, the corresponding reference and simulation models are derived by applying the generalized concept of deterministic channel modelling. The statistical properties of both the reference and the simulation model are studied with emphasis on the amplitude distribution and the correlation properties, which include the temporal, spatial, and frequency correlation functions. The obtained theoretical results are confirmed by MATLAB simulations.

1.4 Thesis Overview

This thesis is organized as follows. In Chapter 2, the geometrical street model is presented and the relationship between the angle of arrival and departure is estab-

lished. The SISO reference model is investigated in Chapter 3. First, the reference model is derived. Afterward, statistical properties including the probability density function, the autocorrelation function, the power spectral density, the level crossing rate, and the average duration of fades are studied. In Chapter 4, the SISO simulation model is derived. We first develop the stochastic simulation model. The latter is the starting point for the derivation of the deterministic simulation model. Moreover, parameter computation methods are presented. In Chapter 5, the SISO model is extended with respect to multi-cluster and frequency selectivity. The MIMO channel is investigated in Chapter 6. In Chapter 7, we draw the conclusion.

Chapter 2

The Geometrical Model

Measurement data can be used to derive channel models. Nevertheless, this type of data is not frequently available. To overcome this problem, geometric scattering model can be exploited to derive channel models. In literature, one can find several geometric scattering models such as the one ring model [15], the two ring model [20], and the elliptical model [22]. In this thesis, a new single bounce geometrical street scattering model is introduced. This model is qualified as a single bounce model due to the assumption that a scattering object results in a single reflected wave when hit by an incident wave. In real-world, a scattering object results in many scattered waves having different directions. The single bounce assumption has been considered in several geometrical models presented in literature. This assumption results in model simplification without affecting the correctness of the model.

2.1 The Geometric Street Scattering Model

The statistical properties of the fading channel depend mainly on the arrangement of scatters around the transmitter and the receiver. The geometric scattering model is the starting point for the derivation of the M2M SISO channel model. To develop our channel model, a new geometrical single bounce street model is introduced. This model is illustrated in Figure.2.1, where the scatters $S^{(n)}$ $(n = 1, 2, \ldots, N)$ lay on the left and/or the right hand side of the street.

The angle of departure (AOD) and the angle of arrival (AOA) are denoted by α_n and θ_n, respectively. In this chapter, it is assumed that the scatters constitute a single cluster having a limited length L. This assumption leads to the limitation of the AOD α_n within the interval $[\alpha_{\min}, \alpha_{\max}]$. Moreover, the transmitter (receiver) is located at a distance h_{T1} (h_{R1}) from the left hand side of the street, and at a distance h_{T2} (h_{R2}) from the right hand side of the street. The distance between the transmitter and the receiver is denoted by D. The symbol MS_T, in Figure.2.1, denotes the mobile transmitter, while MS_R plays the role of the mobile receiver. In addition, the transmitter and receiver are equipped with a single omnidirectional antenna. In our model, we assume that the propagation occurs in the horizontal plan. The angle between the direction of motion of the transmitter and the x-axis is denoted by ψ_T, whereas ψ_R stands for the angle between the direction of motion of the receiver and the x-axis. The transmitter and the receiver are moving with a speed v_T and v_R, respectively.

2.2 Relation Between the AOD and the AOA

To investigate the statistical properties of the channel model, the exact relationship between the AOA and the AOD has to be taken into account. This relationship is derived in Appendix A. The AOA θ_n can be expressed in terms of the AOD α_n according to the relation

$$\theta_n = g(\alpha_n) = \begin{cases} -\pi + g_1(\alpha_n) & \text{if } -\pi \leq \alpha_n \leq -\arctan(\frac{h_{T2}}{D}) \\ g_1(\alpha_n) & \text{if} -\arctan(\frac{h_{T2}}{D}) \leq \alpha_n \leq 0 \\ g_2(\alpha_n) & \text{if } 0 \leq \alpha_n \leq \arctan(\frac{h_{T1}}{D}) \\ \pi + g_2(\alpha_n) & \text{if } \arctan(\frac{h_{T1}}{D}) \leq \alpha_n \leq \pi \end{cases} \tag{2.1}$$

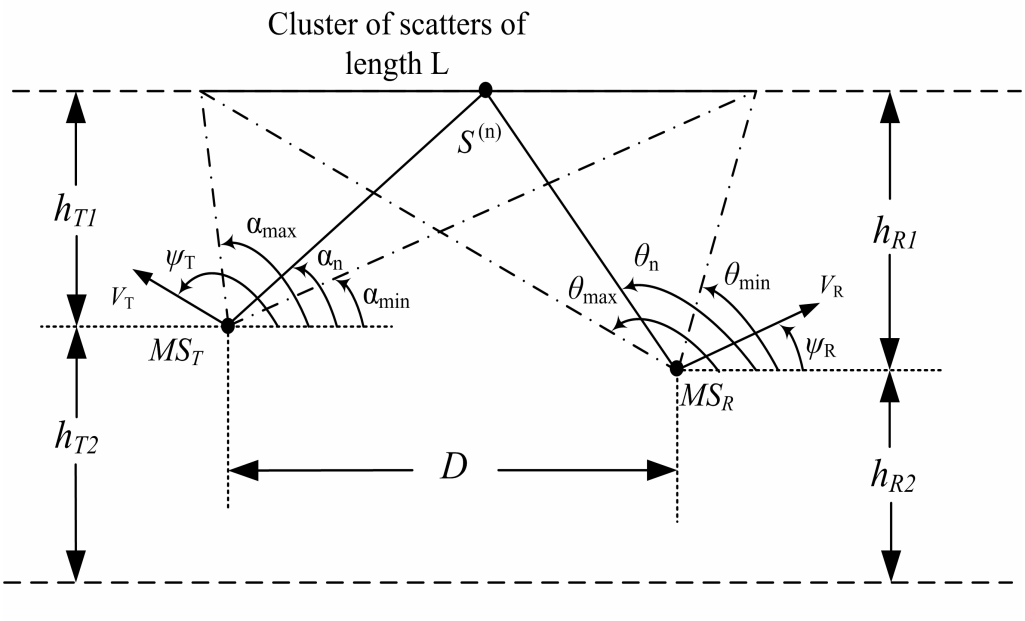

Figure 2.1: Geometric street scattering model for SISO channel.

where

$$g_1(\alpha_n) = \arctan\left(\frac{h_{R2}\cdot\tan(\alpha_n)}{h_{T2}+D\cdot\tan(\alpha_n)}\right) \tag{2.2}$$

$$g_2(\alpha_n) = \arctan\left(\frac{h_{R1}\cdot\tan(\alpha_n)}{h_{T1}-D\cdot\tan(\alpha_n)}\right) \tag{2.3}$$

while the AOD α_n can be expressed as

$$\alpha_n = h(\theta_n) = \begin{cases} -\pi + h_1(\theta_n) & \text{if } -\pi \le \theta_n \le -\pi + \arctan(\frac{h_{R2}}{D}) \\ h_1(\theta_n) & \text{if} -\pi + \arctan(\frac{h_{R2}}{D}) \le \theta_n \le 0 \\ h_2(\theta_n) & \text{if } 0 \le \theta_n \le \pi - \arctan(\frac{h_{R1}}{D}) \\ \pi + h_2(\theta_n) & \text{if } \pi - \arctan(\frac{h_{R1}}{D}) \le \theta_n \le \pi \end{cases} \tag{2.4}$$

where

$$h_1(\theta_n) = \arctan\left(\frac{h_{T2}\cdot\tan(\theta_n)}{h_{R2}-D\cdot\tan(\theta_n)}\right) \tag{2.5}$$

$$h_2(\theta_n) = \arctan\left(\frac{h_{T1}\cdot\tan(\theta_n)}{h_{R1}+D\cdot\tan(\theta_n)}\right). \tag{2.6}$$

Since the exact relation between the AOD α_n and the AOA θ_n is determined, thus the statistical properties of the SISO M2M channel model can now be investigated. The derivation of the statistical properties of the SISO M2M channel model will constitute the object of the next chapter.

Chapter 3

The SISO Reference Model

In this chapter, the reference model for the M2M SISO channel is derived, starting from the geometrical street model. Afterward, the statistical properties of the reference model are analyzed. Analytical expression for the probability density, the power spectral density, and the autocorrelation function are provided. Moreover, the expressions of the level crossing rate and the average duration of fades are determined.

3.1 Derivation of the Reference Model

The geometrical street model presented in previous chapter describes the scattering geometric street model for the M2M SISO channel, which constitutes the starting point for the derivation of the corresponding reference model. From the geometric street model illustrated in Figure.2.1, it can be seen that the n^{th} plane wave emitted from the transmit antenna travels over the n^{th} scatter $S^{(n)}(n = 1, 2, \ldots, N)$ before arriving at the receive antenna. It is assumed that the number of scatters is infinite. Consequently, the diffuse component as seen from the receiver side is composed of an infinite number of homogenous plane waves. Considering the geometrical model in Figure.2.1, the link between the transmit antenna and the receive antenna can be described by its complex channel gain given by

$$g(\vec{r}_T, \vec{r}_R) = \lim_{N\to\infty} \sum_{n=1}^{N} c_n e^{j\left(\beta_n + \vec{k}_T^{(n)}\cdot\vec{r}_T - \vec{k}_R^{(n)}\cdot\vec{r}_R - k_0 D_n\right)} \tag{3.1}$$

where c_n and β_n denote the gain and the phase shift introduced by the scatter $S^{(n)}$, respectively. The gain c_n is assumed to be constant and is given by

$$c_n = \sqrt{\frac{2\sigma_0^2}{N}} \tag{3.2}$$

where $2\sigma_0^2$ is the mean power of the received scattered components. Furthermore, it is assumed that the phase shifts β_n are independent, identically distributed (i.i.d.) random variables, each having a uniform distribution over the interval $[0, 2\pi)$.

The second phase component in (3.1), $\vec{k}_T^{(n)} \cdot \vec{r}_T$, expresses the influence of the transmitter movement on the channel gain. The symbol $\vec{k}_T^{(n)}$ denotes the wave vector pointing in the propagation direction of the n^{th} transmitted plane wave, and $\vec{r}_T$ is the spatial translation vector of the transmitter. The scalar product $\vec{k}_T^{(n)} \cdot \vec{r}_T$ can be expressed as

$$\vec{k}_T^{(n)} \cdot \vec{r}_T = 2\pi f_{T_{\max}} \cos(\alpha_n - \psi_T)t \tag{3.3}$$

where $f_{T_{\max}} = v_T/\lambda$ stands for the maximum Doppler frequency due to the transmitter movement. The symbol v_T represents the transmitter speed, while λ denotes the wavelength.

The third phase component in (3.1), $\vec{k}_R^{(n)} \cdot \vec{r}_R$, expresses the influence of the receiver movement on the channel gain. The symbol $\vec{k}_R^{(n)}$ denotes the wave vector pointing in the propagation direction of the n^{th} received plane wave, and $\vec{r}_T$ is the spatial translation vector of the receiver. The scalar product $\vec{k}_R^{(n)} \cdot \vec{r}_R$ can be expressed as

$$\vec{k}_R^{(n)} \cdot \vec{r}_R = -2\pi f_{R_{\max}} \cos(\theta_n - \psi_R)t \tag{3.4}$$

where $f_{R_{\max}} = v_R/\lambda$ stands for the maximum Doppler frequency due to the receiver movement. The symbol v_R represents the receiver speed.

The term $k_0 D_n$ in (3.1) is due to the total travelled distance and can be expressed as

$$k_0 D_n = \frac{2\pi}{\lambda}\left(D_T^{(n)} + D_R^{(n)}\right) \tag{3.5}$$

where $D_T^{(n)}$ corresponds to the distance from the transmit antenna to the scatter $S^{(n)}$, and $D_R^{(n)}$correspond to the distance from the scatter to the receive antenna. The quantity $D_T^{(n)}$ is given by $D_T^{(n)} = h_{T1}/\sin(\alpha_n)$, whereas $D_R^{(n)}$ is given by $D_R^{(n)} = h_{R1}/\sin(\theta_n)$.

After substituting (3.2)–(3.5) in (3.1), the complex channel gain in (3.1) can be expressed as

$$g(t) = \lim_{N\to\infty}\sqrt{\frac{2\sigma_0^2}{N}}\sum_{n=1}^{N} d_n \cdot e^{j\left(2\pi(f_T^{(n)}+f_R^{(n)})t+\beta_n\right)} \tag{3.6}$$

where

$$d_n = e^{-j\frac{2\pi}{\lambda}((h_{T1}/\sin(\alpha_n))+(h_{R1}/\sin(\theta_n)))} \tag{3.7}$$

$$f_T^{(n)} = f_{T_{\max}}\cos(\alpha_n - \psi_T) \tag{3.8}$$

$$f_R^{(n)} = f_{R_{\max}}\cos(\theta_n - \psi_R). \tag{3.9}$$

By applying the expected operator on the diffuse component in (3.6), it can be proven that the mean value of the complex channel gain $g(t)$ is equal to 0. While, the mean power of the complex channel gain $g(t)$ is given by

$$Var\{g(t)\} = E\{g^*(t)g(t)\} \tag{3.10}$$

where $E\{\cdot\}$ is the expectation operator. It can easily be proven that the mean power of the complex channel gain $g(t)$ is equal to $2\sigma_0^2$. Hence, invoking the central limit theorem, we can conclude that the envelop $|g(t)|$ follows a Rayleigh distribution.

3.2 Probability Density Function (PDF)

3.2.1 Probability Density Function of the AOD

In this chapter, It is assumed that the scatters constitute a single cluster having a limited length L as shown in Figure.2.1 on page 17. This assumption leads to the limitation of the AOD α_n within the interval $[\alpha_{\min}, \alpha_{\max}]$. Under the assumption that the transmitter is equipped with an omnidirectional antenna, the AOD α_n are uniformly distributed over the interval $[\alpha_{\min}, \alpha_{\max}]$. Hence, the probability density function of the AOD α_n can be expressed as

$$p_{\alpha_n}(\alpha_n) = \begin{cases} \dfrac{1}{\Delta\alpha} & \text{if } \alpha_{\min} \leq \alpha_n \leq \alpha_{\max} \\ 0 & \text{otherwise} \end{cases} \tag{3.11}$$

where $\Delta\alpha = |\alpha_{\max} - \alpha_{\min}|$.

3.2.2 Probability Density Function of the AOA

The AOA θ_n can be expressed in terms of the AOD α_n as $\theta_n = g(\alpha_n)$ according to (2.1). Based on this relationship and since the expression of the PDF of the AOD α_n is given by (3.11), then the PDF of the AOA θ_n denoted by $p_{\theta_n}(\theta_n)$ can be derived. Using the transformation of random variable fundamental theorem, it is possible to express $p_{\theta_n}(\theta_n)$ as

$$p_{\theta_n}(\theta_n) = \frac{p_{\alpha_n}(\alpha_1)}{|g'(\alpha_1)|} \tag{3.12}$$

where $g'(\alpha_n)$ denotes the derivative of $g(\alpha_n)$, and α_1 is the root of the equation $\theta_n = g(\alpha_n)$.

Using the transformation of random variable fundamental theorem, The PDF $p_{\theta_n}(\theta_n)$ of the AOA θ_n can be expressed as

$$p_{\theta_n}(\theta_n) = \begin{cases} \dfrac{1}{\Delta\alpha} \dfrac{h_{R2} \cdot h_{T2}}{\sin^2(\theta_n)\left[\left(h_{R2} \cdot \cot(\theta_n) - D\right)^2 + h_{T2}^2\right]} & \text{if } \ -\pi \leq \theta_n \leq 0 \\ \dfrac{1}{\Delta\alpha} \dfrac{h_{R1} \cdot h_{T1}}{\sin^2(\theta_n)\left[\left(h_{R1} \cdot \cot(\theta_n) + D\right)^2 + h_{T1}^2\right]} & \text{if } \ 0 \leq \theta_n \leq \pi. \end{cases} \tag{3.13}$$

The derivation of the PDF $p_{\theta_n}(\theta_n)$ of the AOA θ_n can be found in Appendix B. It should be noted here that the parameters influencing the PDF $p_{\theta_n}(\theta_n)$ of the AOA θ_n doesn't include the speed of the transmitter and the receiver neither their directions of motion.

3.2.3 Numerical and Simulation Results

In this section, we present some illustrative examples for the PDF of the AOA. In the first scenario, an infinite length cluster of scatters located on the left hand side of the street. In this scenario, we consider that both the transmitter and the receiver are at the same distance from left side of the street, i.e. $h_{T1} = h_{R1}$. Under the given conditions, the expression of the PDF of the AOA becomes

$$p_{\theta_n}(\theta_n) = \frac{1}{\Delta\alpha} \frac{1}{\sin^2(\theta_n)\left[\left(\cot(\theta_n) + D/h_{T1}\right)^2 + 1\right]}. \tag{3.14}$$

We study for the described scenario the influence of the ratio D/h_{T1} on the PDF of the AOA. the obtained results are presented in Figure.3.1

Observing Figure.3.1, we can conclude that the ratio D/h_{T1} has a big influence on the PDF of the AOA. If we fix the value of the term h_{T1}, the results obtained by varying the distance D are similar to those depicted in Figure.3.1. Hence, the illustrated results shows also the influence of the distance between the transmitter and the receiver on the PDF of the AOA. We can see from Figure.3.1 (a) that the PDF of the AOA has a sinusoidal shape. This scenario occur if the transmitter and the receiver are very near to each other. As the distance D increases as shown in 3.1 (b), a main lobe appear near to π, while a side lobe can be observed a side lobe near to 0. If we increase the distance more and more, the PDF of the AOA approaches a Dirac function, as shown in Figure.3.1 (c). In Figure.3.1 (d), we can observe a perfect Dirac function located at π.

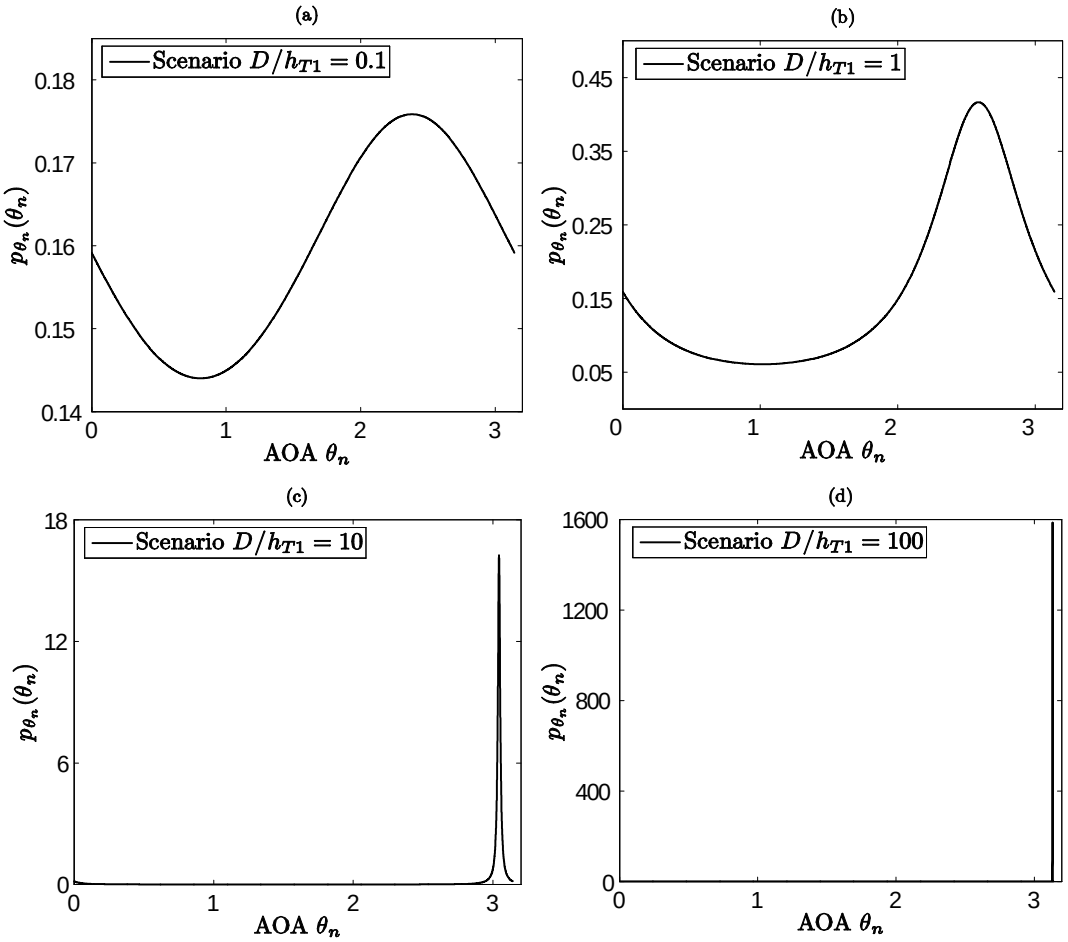

Figure 3.1: The PDF of AOA for various values of h_{T1}/D; scenario of an infinite length scatter located on the left hand side of the street

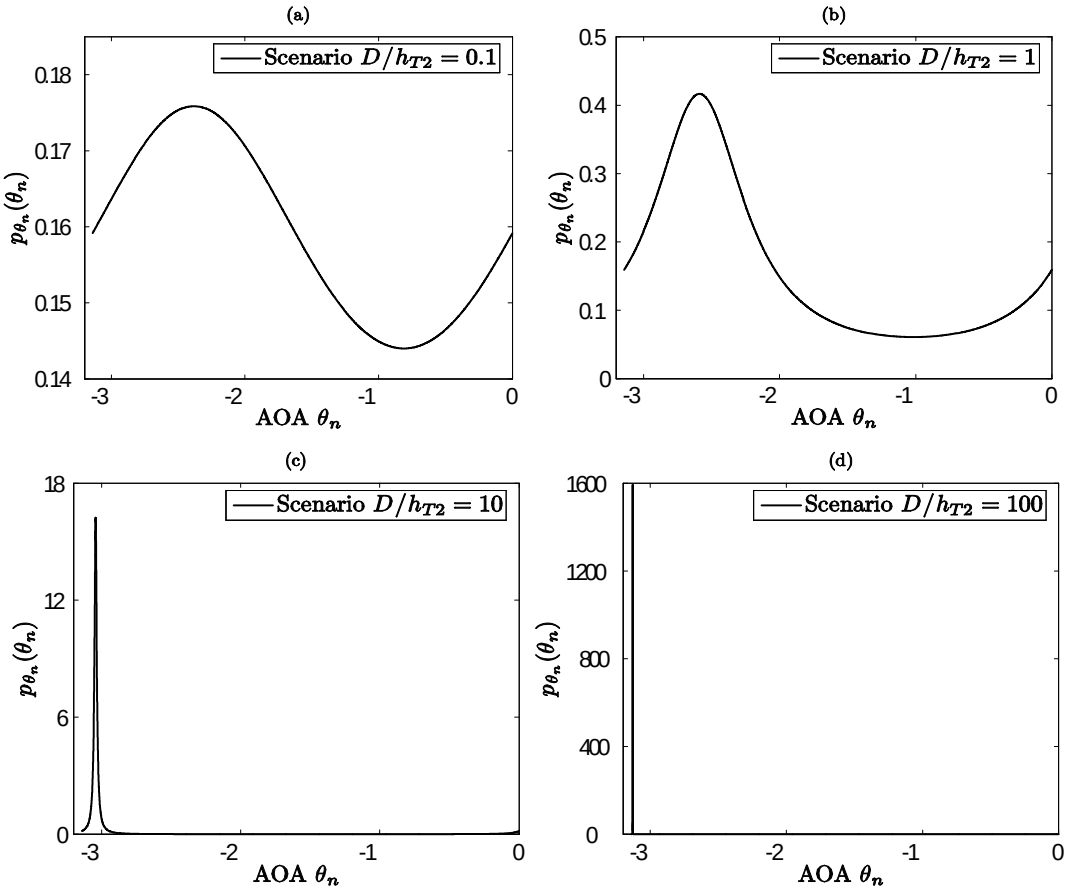

Figure 3.2: The PDF of AOA for various values of h_{T1}/D; scenario of an infinite length scatter located on the right hand side of the street

In Figure.3.2, represents the PDF of the AOA for the case where an infinite length cluster of scatters is located on the right hand side of the street. Both the transmitter and the receiver are located at the same distance from the right edge of the street, i.e., $h_{T2} = h_{R2}$. Note also, that for a given value of the ratio D/h_{T2} that is equal to D/h_{T1}, the curves in Figure.3.2 and in Figure.3.1 are symmetric. This fact can be also proved by using the analytical expression of the PDF of the AOA, given that the distances h_{T1}, h_{T2}, h_{R1}, and h_{R2} are equals.

We consider now some scenarios where the cluster of scatters has a finite length (see Figure.2.1 on page 17). To simulate such scenario we need to provide mainly the length of the cluster L in addition to the angle $\alpha_{\max}$ and the distance h_{T1}. The position of the cluster is totally defined by this three parameters, since the angle $\alpha_{\min}$ can be expressed in terms of L, h_{T1}, and $\alpha_{\max}$ as

$$\alpha_{\min} = \begin{cases} \operatorname{arccot}(\dfrac{L}{h_{T1}} + \cot(\alpha_{\max})) & \text{if } \alpha_{\max} \geq 0 \\ \operatorname{arccot}(\dfrac{L}{h_{T1}} + \cot(\alpha_{\max})) - \pi & \text{if } \alpha_{\max} < 0. \end{cases} \tag{3.15}$$

In Figure.3.3 the influence of the parameter h_{R1} on the PDF of the AOA is illustrated. We remind that h_{R1} represents the distance between the receiver and the left hand side of the street. In the current scenario a cluster of scatter having a length of $L = 10\ m$ is considered. The maximum angle of departure $\alpha_{\max}$ is equal to $\pi/2$, while the distance D is equal to 5 m, and h_{T1} is equal to 5 m. In Figure.3.3, the curve with solid line represents the PDF of the AOA in case that $h_{R1} = 3\ m$. Note here that $h_{R1} < h_{T1}$, this scenario can happen in reality if we have to cars driving in two different columns of a road and trying to communicate using IVC. The curve with dashed line is obtained for a value of $h_{R1} = 5\ m$ which is the same value as h_{T1}. this scenario can happen if we have one care behind another one. This scenario is

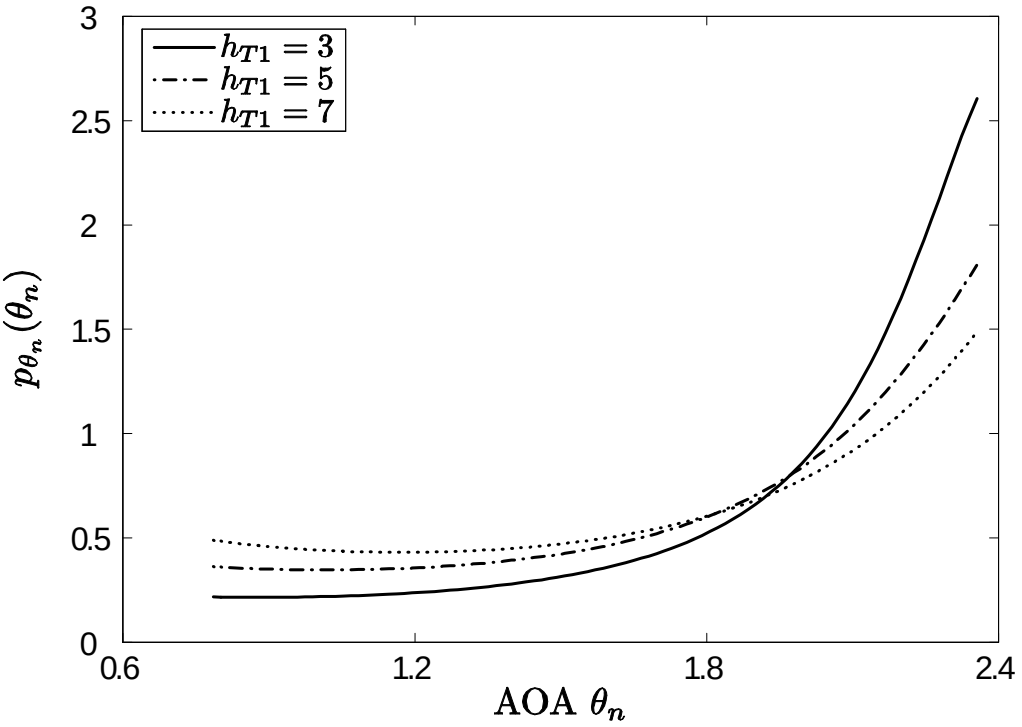

Figure 3.3: Influence of h_{T1} on the PDF of AOA.

mainly needed to avoid collision with the car ahead by using safety warnings. The curve with dotted line is obtained for a value of $h_{R1} = 7\ m$, i.e., $h_{R1} > h_{T1}$. One can see from the three curves that for this scenario the probability of having a wave arriving from an angle 134.6° — correspond to 2.35 radium, which is the end point for all curves depicted in Figure.3.3— is the highest. Moreover, the probability of having a wave arriving from an angle 44.7°— correspond to 0.78 radium, which is the end point for all curves depicted in Figure.3.3— is the lowest. furthermore, as we decrease the value of h_{R1}, the probability of having a wave arriving from an angle 134.6° decreases, but the probability of having a wave arriving from an angle 44.7° increases.

In order to verify the correctness of the obtained results, we use the Monte Carlo Method. First a uniformly distributed random variable defined over the interval $[\alpha_{\min}, \alpha_{\max}]$ is generated. Using the relation between the AOA and the AOD according to equation.2.1 on page 16, a random variable representing the AOA can be generated. To obtain the PDF of the AOA the function histogram of Matlab is used. We generate one million samples to guarantee the precision of the results. The obtained results are illustrated in Figure.3.4. In the current scenario the parameters $\alpha_{\max}$, L, h_{T1}, h_{R1} and D are equal to $\pi/2$, 10 m, 5 $m, 5m$ and $5m$, respectively. In the Figure.3.4, a good fitting between the simulation and the theoretical PDF of the AOA can be observed. Hence, the correctness of the model is verified.

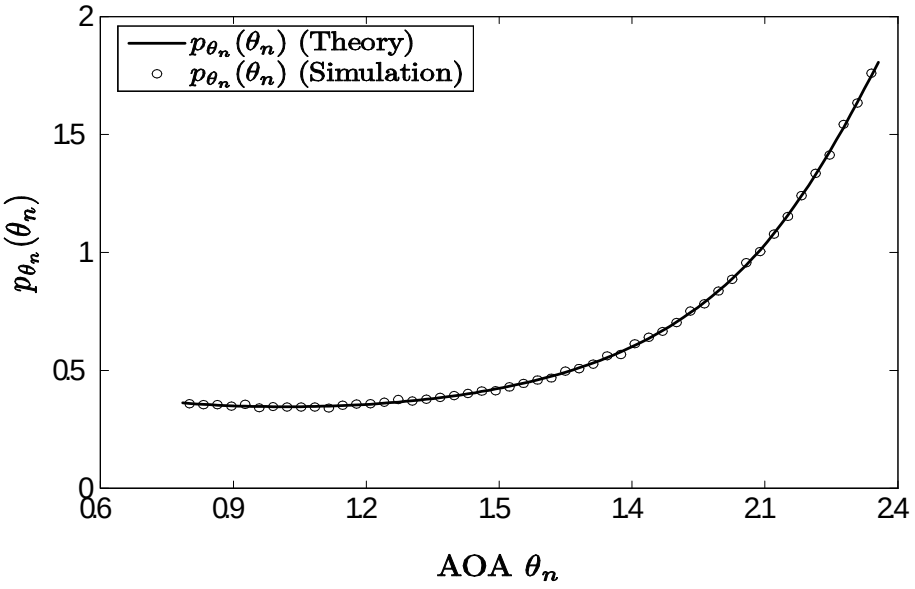

Figure 3.4: Theoretical and simulation results for the PDF of AOA $p_{\theta_n}(\theta_n)$.

3.3 Doppler Power Spectral Density(PSD)

For mobile-to-mobile channels the transmitter and the receiver are on the move. This motion results in Doppler effect that causes a frequency shift for each wave. A wave transmitted at an AOD α_n and arriving to the receiver at an AOA θ_n undergoes a Doppler shift according to the relation

$$\begin{aligned} f &= f_T + f_R \\ &= f_{T\max}\cos(\alpha_n - \psi_T) + f_{R\max}\cos(\theta_n - \psi_R). \end{aligned} \tag{3.16}$$

In this case, the term f_T represents the Doppler shift due to the motion of the transmitter, while the term f_R represents the Doppler shift due to the motion of the transmitter. The terms ψ_T and ψ_R represents the direction of motion of the transmitter and the receiver, respectively. The maximum Doppler shift due to the movement of the transmitter is denoted by $f_{T\max}$. It can be expressed in term of the transmitter speed v_T, the speed of light c_0, and the carrier frequency f_c according to

$$f_{T\max} = \frac{v_T}{c_0} f_c. \tag{3.17}$$

The maximum Doppler shift due to the movement of the receiver is denoted by $f_{R\max}$. It can be expressed in term of the receiver speed v_R, the speed of light c_0, and the carrier frequency f_c according to

$$f_{R\max} = \frac{v_R}{c_0} f_c. \tag{3.18}$$

In the frequency domain, the Doppler effect results in an expansion of the transmitted signal spectrum. In the time domain the Doppler effect implicates that the impulse response of the channel becomes time-variant.

The expression (3.16) implicates that the Doppler shift is a function of the AOD α_n and the AOA θ_n, which are random variables in our model. hence the Doppler shift

f is also a random variable. Since the AOA θ_n can be expressed in terms of the AOD α_n according to (2.1), then f is a function of the AOD α_n. Hence, the PDF $p_f(f)$ of the Doppler frequencies f can be derived for any given $p_{\alpha_n}(\alpha_n)$ using the fundamental theorem of transformation of random variables. In order to derive the expression of $p_f(f)$, we need first to find the roots of the equation $f = h(\alpha_n)$. The function h is obtained by substituting θ_n according to 2.1, in the equation.3.16. unfortunately, a close form solution doesn't exists for the roots. furthermore the number of roots depend of the considered scenario as shown in Figure.3.5. for the illustrated scenario the value of $\alpha_{\max}$, L, h_{R1}, h_{T1} and D are equal to $\pi/2$, 20 m, $5m$ and 3 m, respectively. In addition, we consider that both the transmitter and the receiver have a speed of 110 Km/h. The carrier frequency f_c is equal to 900 MHz. For the scenario depicted in Figure.3.5 (a), the direction of motion of the transmitter ψ_T and the direction of motion of the receiver ψ_R are equal to π and $\pi/2$, respectively. in Figure.3.5 (b), the direction of motion of the transmitter ψ_T and the direction of motion of the receiver ψ_R are equal to 0 and π, respectively. one can see from those two scenarios that the shape of the Doppler frequency change drastically for the same range of the AOD α_n. Moreover, for some values of f , the equation $f = h(\alpha_n)$ has 3 roots and for other values 2 or 1 root. For all the listed reasons the PDF $p_f(f)$ of the Doppler frequencies f will be evaluated analytically.

The Doppler power spectral density(PSD) $S_{gg}(f)$ is proportional to the PDF $p_f(f)$ of the Doppler frequencies f, we can write

$$S_{gg}(f) = 2\sigma_0^2 \cdot p_f(f) \tag{3.19}$$

where $2\sigma_0^2$ is the mean power of the received scattered components. Using (3.16), it can be proved that the Doppler PSD $S_{gg}(f)$ is bounded depending on the length of the cluster of scatters L. Hence, the maximum (minimum) Doppler frequency

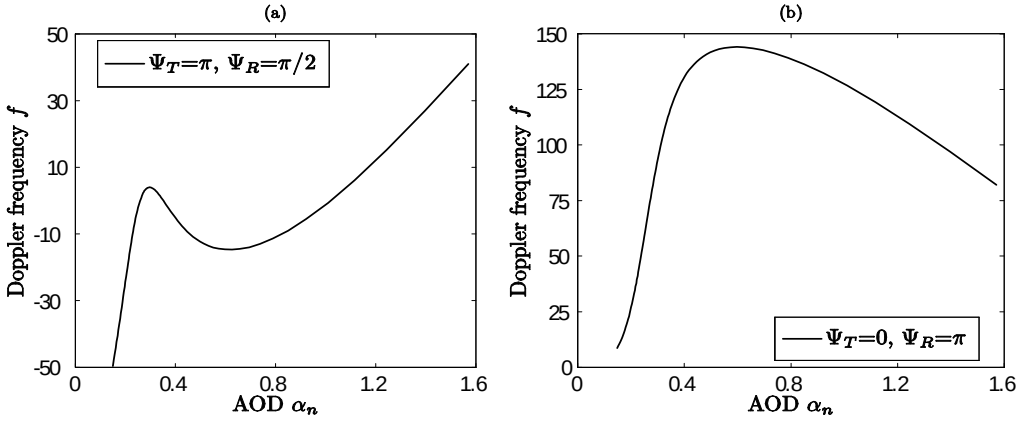

Figure 3.5: Variation of the Doppler frequency f for various values of ψ_T and ψ_R.

$f_{\max}(-f_{\max})$ given by $f_{\max} = f_{T\max} + f_{R\max}$ $(-f_{\max} = -f_{T\max} - f_{R\max})$ is not always reached.

3.3.1 Numerical and Simulation Results

In this section, we present some illustrative examples for the Doppler PSD. For all the scenarios listed in this section some parameters remain constant . These parameters are the speed of the transmitter and the receiver which is equal to 110 Km/h, the direction of motion of the transmitter and the receiver denoted by ψ_T and ψ_R ,respectively, which is equal to 0. The carrier frequency has been set to 900MHz.

First, we start by studying the influence of the distance D separating the transmitter form the receiver on the PSD of Doppler frequencies. For the considered scenario we choose the parameters $\alpha_{\max} = 3\pi/4$, $L = 30m$, $\sigma_0^2 = 1$, and $h_{R1} = h_{T1} = 10m$. The obtained results are illustrated in Figure.3.6.

One can conclude from the Figure.3.6 that the contribution of negative frequency increases as the distance D increases, while the contribution of positive frequencies decreases as D decreases. This fact can be explained by considering the influence of D

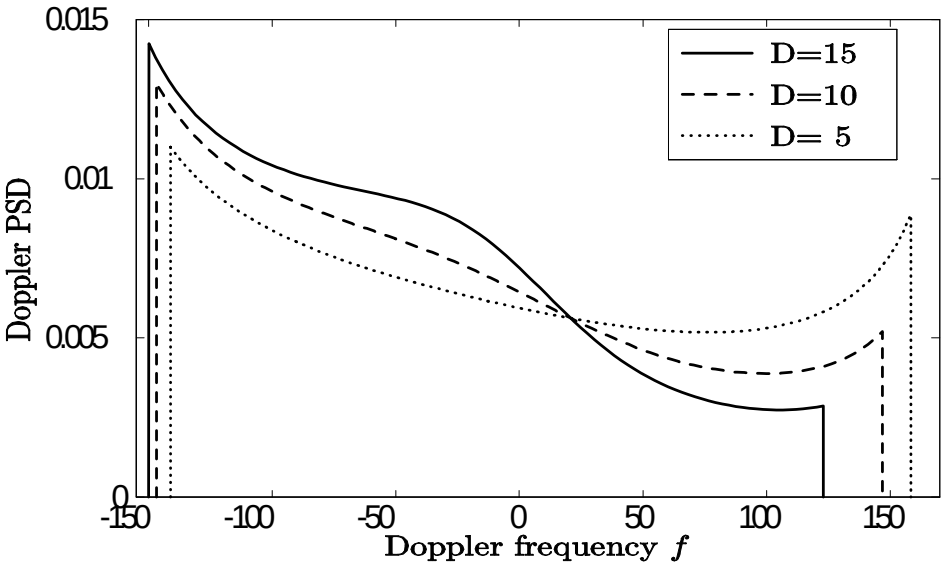

Figure 3.6: The Doppler PSD for various values of D.

on the PDF of the AOA. Let consider again the Figure.3.1, in this figure the influence of D on the PDF of the AOA is illustrated. From this Figure, one can conclude that the probability of the event " the AOA superior to $\pi/2$" increases as the distance D increases. This remark is of importance since all values of the AOA superior to $\pi/2$ results in negative contribution in the Doppler PSD. This effect can be observed in Figure.3.6, where an increase in the contribution of the negative frequencies can be seen as the distance D increases.

We consider now influence of the distance h_{T1} separating the transmitter form the left hand side of the street on the PSD of Doppler frequencies. For this purpose we considered a scenario where the simulation parameters are given by $\alpha_{\max} = \pi/2$, $L = 20m$, and $h_{R1} = 5m$, $\sigma_0^2 = 1$, and $D = 10$. The obtained results are illustrated in Figure.3.7. It can be seen from this figure the contribution of the negative frequen-

cies increases as the quantity h_{T1} decreases, while the contribution of the positive frequencies decreases as h_{T1} decreases. This fact can be explained by the influence of the parameter h_{T1} on the PDF of the AOA. From Figure.3.3, one can conclude the probability of the event "the AOA superior to $\pi/2$" increases as the distance h_{T1} decreases. This remark is of importance, since all values of the AOA superior to $\pi/2$ results in negative contribution in the Doppler PSD. This effect can be observed in Figure.3.7, where an increase in the contribution of the negative frequencies can be seen as the distance h_{T1} decreases.

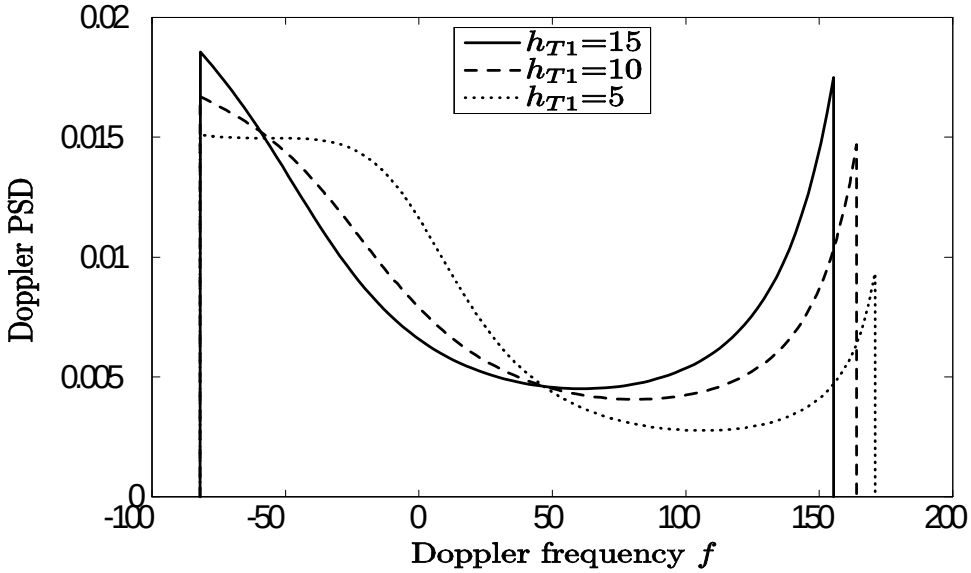

Figure 3.7: The Doppler PSD for various values of h_{T1}.

In order to verify the correctness of the obtained results, we use the Monte Carlo Method. In fact, the Doppler frequencies f can be expressed as a function of the AOD α_n, which is uniformly distributed over the interval $[\alpha_{\min}, \alpha_{\max}]$. To simulate the Doppler PSD, we start fist by generating the AOD α_n. Using the relation between the

AOD α_n and the Doppler frequencies f, a random variable representing the Doppler frequencies can be generated. To obtain the PDF $p_f(f)$ of the Doppler frequencies f the function histogram of Matlab is used. Afterward using the relation (3.19), the Doppler PSD can be found. We generate one million samples to guarantee the precision of the results. The obtained results are illustrated in Figure.3.8. In the current scenario the parameters $\alpha_{\max}$, L, h_{T1}, h_{R1} and D are equal to $\pi/2$, 20 m, 15 $m, 10m$ and $10m$, respectively. In the Figure.3.4, a good fitting between the simulation and the theoretical Doppler PSD can be observed. Hence, the correctness of the model is verified.

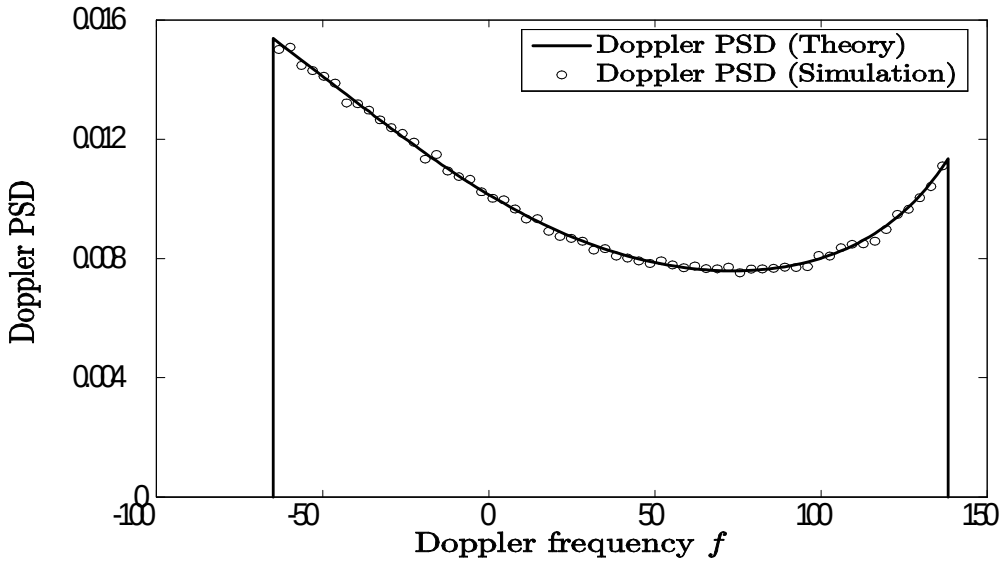

Figure 3.8: Theoretical and simulation results for the PSD of the Doppler frequencies f.

One can remarks a general feature for all the presented scenario is that the shape of the PSD is asymmetrical.

Two characteristics quantities can be derived from the Doppler PSD. The first quantity is the average Doppler shift $B_{gg}^{(1)}$, which is a measure of the center of gravity of the Doppler PSD $S_{gg}(f)$. The second quantity is ,which is a measure of the range of values of the Doppler frequencies f over which $S_{gg}(f)$ is essentially nonzero. The average Doppler shift $B_{gg}^{(1)}$ is defined as

$$\begin{aligned} B_{gg}^{(1)} &: = \frac{\int_{-\infty}^{\infty} f \cdot S_{gg}(f)df}{\int_{-\infty}^{\infty} S_{gg}(f)df} \\ &= \frac{\int_{-\infty}^{\infty} f \cdot 2\sigma_0^2 \cdot p_f(f)df}{\int_{-\infty}^{\infty} 2\sigma_0^2 \cdot p_f(f)df} \\ &= \frac{\int_{-\infty}^{\infty} f \cdot p_f(f)df}{\underbrace{\int_{-\infty}^{\infty} p_f(f)df}_{=1}} \\ &= \int_{f_l}^{f_u} f \cdot p_f(f)df \end{aligned} \tag{3.20}$$

where the symbols f_l and f_u denote the maximum and the minimum Doppler shift that can be reached for a given scenario. These two values depend mainly on the length of the cluster of scatters L. the latter leads to the limitation of the Doppler PSD to a relatively narrow band $[f_l, f_u]$. Since the Doppler PSD is generally asymmetrical, the average Doppler shift is then nonzero.

The Doppler spread $B_{gg}^{(2)}$ is defined as

$$\begin{aligned} B_{gg}^{(2)} &: = \sqrt{\frac{\int_{-\infty}^{\infty} (f - B_{gg}^{(1)})^2 \cdot S_{gg}(f)df}{\int_{-\infty}^{\infty} S_{gg}(f)df}} \\ &= \sqrt{\int_{f_l}^{f_u} (f - B_{gg}^{(1)}) \cdot p_f(f)df}. \end{aligned} \tag{3.21}$$

3.4 Autocorrelation Function (ACF)

The study of the ACF is of great importance. In fact the value of the ACF at the origin correspond to the mean power of the received scattered components. Furthermore, the shape of the ACF around the origin gives an idea about how fast the channel changes. if the ACF is flat around the origin, then the channel changes fast. on the contrary if the ACF changes fast drop of the ACF can be seen around the origin, then the channel changes fast. The ACF of the complex channel gain $g(t)$ is defined as

$$r_{gg}(\tau) := E\{g^*(t)g(t+\tau)\}. \tag{3.22}$$

where $(\cdot)^*$denotes the complex conjugation, while $E\{\cdot\}$ is the expectation operator. The expression of the complex channel gain $g(t)$ is given by(3.6). Hence, the ACF can be evaluated by substituting $g(t)$ in (3.22)

$$\begin{aligned} r_{gg}(\tau) &= E\{g^*(t)g(t+\tau)\} \\ &= \lim_{N\to\infty}\lim_{M\to\infty}\frac{2\sigma_0^2}{N}E\left\{\begin{array}{c}\sum_{n=1}^{N}\sum_{m=1}^{M} d_n^*\cdot e^{-j\left(2\pi(f_T^{(n)}+f_R^{(n)})t+\beta_n\right)} \\ \cdot d_m\cdot e^{j\left(2\pi(f_T^{(m)}+f_R^{(m)})(t+\tau)+\beta_m\right)}\end{array}\right\} \\ &= \lim_{N\to\infty}\lim_{M\to\infty}\frac{2\sigma_0^2}{N}E\left\{\begin{array}{c}\sum_{n=1}^{N}\sum_{m=1}^{M} d_n^*\cdot e^{-j\left(2\pi(f_T^{(n)}+f_R^{(n)})t\right)} \\ \cdot d_m\cdot e^{j\left(2\pi(f_T^{(m)}+f_R^{(m)})(t+\tau)\right)}.e^{-j(\beta_n-\beta_m)}\end{array}\right\} \end{aligned} \tag{3.23}$$

Let consider the random variable ξ given by $\xi = (\beta_n - \beta_m) \bmod 2\pi$. The random variable ξ is uniformly distributed over the interval $[0, 2\pi)$ for all values of m and n expect for $m = n$. When $m = n$, the random variable ξ is always equal to 0. Hence, we can write

$$E\{\xi\} = \left\{\begin{array}{lll} 0 & \text{if} & n \neq m \\ 1 & \text{if} & n = m \end{array}\right. \tag{3.24}$$

This fact allow us to simplify the expression of the ACF as follow

$$\begin{aligned} r_{gg}(\tau) &= \lim_{N\to\infty} \frac{2\sigma_0^2}{N} E\left\{ \sum_{n=1}^{N} d_n^* \cdot e^{-j\left(2\pi(f_T^{(n)}+f_R^{(n)})t\right)} \cdot d_n \cdot e^{j\left(2\pi(f_T^{(n)}+f_R^{(n)})(t+\tau)\right)} \right\} \\ &= \lim_{N\to\infty} \frac{2\sigma_0^2}{N} E\left\{ \sum_{n=1}^{N} e^{j\left(2\pi(f_T^{(n)}+f_R^{(n)})\tau\right)} \right\}. \end{aligned} \tag{3.25}$$

where the quantities $f_T^{(n)}$ and $f_R^{(n)}$ are given by (3.8) and (3.9), respectively. The expectation operator has now to be applied on the remaining random variables α_n. We remind that the AOA θ_n can be expressed in terms of the AOD α_n according to (2.1). As the number of scatters tends to infinity the discrete random variables α_n and θ_n become continuous random variables denoted by α and θ, respectively. The AOA θ can be expressed in terms of α according to (2.1). The infinitesimal power of the diffuse component corresponding to the differential angle $d\alpha$ is proportional to $p_\alpha(\alpha)\, d\alpha$, where $p_\alpha(\alpha)$ denotes the distribution of α. As $N \to \infty$, this infinitesimal contribution must be equal to $1/N = p_\alpha(\alpha)\, d\alpha$. Consequently, it follows from (3.25) that the ACF of the SISO reference model can be expressed as

$$r_{gg}(\tau) = 2\sigma_0^2 \int_{\alpha_{\min}}^{\alpha_{\max}} e^{j(2\pi(f_T(\alpha)+f_R(\theta(\alpha)))\tau)} p_\alpha(\alpha)\, d\alpha. \tag{3.26}$$

The expression $\theta(\alpha)$ emphasis the fact that the AOA θ can be expressed in terms of the AOD α according to (2.1).

The channel gain $g(t)$ is complex then it could be written in the form

$$g(t) = g_I(t) + j g_Q(t) \tag{3.27}$$

where $g_I(t)$ and $g_Q(t)$ are the inphase and the quadrature components of the channel gain, respectively. The autocorrelation functions $r_{g_I g_I}(\tau)$ and $r_{g_I g_Q}(\tau)$ can be

expressed as

$$r_{g_I g_I}(\tau) = 1/2 \ \mathrm{Re}\{r_{gg}(\tau)\} \quad (3.28)$$

$$r_{g_I g_Q}(\tau) = 1/2 \ \mathrm{Im}\{r_{gg}(\tau)\}. \quad (3.29)$$

Since $r_{g_I g_Q}(\tau)$ is nonzero, then the inphase and the quadrature components of the channel gain are correlated.

3.4.1 Numerical Results

In this section some numerical results are presented for various scenarios. In order to eliminate the effect of the speed of the transmitter and the receiver on the ACF the temporal separation τ is normalized. In typical cellular channel where only the receiver is moving the normalization consists in multiplying τ by $f_{\max}$, where $f_{\max} = (v/c_0)f_0$. But since we have an M2M channel then the normalization differs from the one used in typical cellular channels. In fact, we can distinguish between two cases. if the transmitter and the receiver have the same speed, then the quantity $f_{T\max} = f_{R\max}$. For this situation, the normalization could be done by multiplying τ by either $f_{T\max}$ or $f_{R\max}$, since they are equal. However, if the transmitter and the receiver have different speeds, no solution has been found. One may think to use the relative speed to normalize the temporal separation which is a fallacy. For instance, if the transmitter and the receiver have the same speed and the same direction of motion, then the relative speed is equal to zero. If we use the relative speed to normalize the temporal separation τ, we will multiply τ by 0. In the following scenarios, only cases where the transmitter and the receiver have similar speed are considered. In order to illustrate the influence of different parameters on the absolute value of the ACF we present in the following obtained results for various scenarios. In the Figure.3.9(a), we illustrate the influence of the length of the cluster of scatters L on the absolute

value of the ACF. In the current scenario, the parameters $\alpha_{\max}$, h_{T1}, h_{R1}, D, σ_0^2, ψ_R, ψ_T are equal to $\pi/2$, 10 m, 10 m, $20m$, 0.5, π and 0, respectively. From Figure.3.9(a), it can be seen the as we decrease the length of the cluster the ACF becomes more flat around the origin. Hence, the channel changes slowly in case that the length of the cluster is small. On the contrary, if the length of the cluster increases the channel changes fast.

In the Figure.3.9(b), we illustrate the influence of the position of the cluster of scatter given by $\alpha_{\max}$ on the absolute value of the ACF. By varying the value of $\alpha_{\max}$, we are in fact shifting the cluster along the left edge of the street. In the current scenario the parameters L, h_{T1}, h_{R1}, D, σ_0^2, ψ_R, ψ_T are equal to 10 m, 10 m, 10 m, $20m$, 0.5, 0 and 0, respectively. From Figure.3.9(b), it can be seen the as we decrease the value of $\alpha_{\max}$ the ACF becomes more flat around the origin. Hence, the channel changes slowly in case that the value of $\alpha_{\max}$ is small. On the contrary, if the the value of $\alpha_{\max}$ is near to π the channel changes fast.

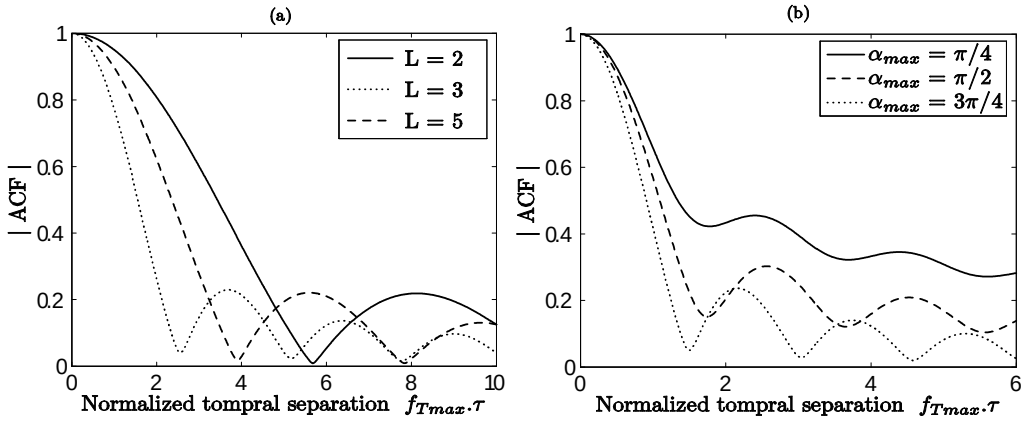

Figure 3.9: Absolute value of ACF: (a) for various values of L and (b) or various values of $\alpha_{\max}$.

In the Figure.3.10(a), we illustrate the influence of the position of the receiver relatively to the left hand side of the street, given by h_{R1}, on the absolute value of the ACF. By varying the value of h_{R1}, we are in fact shifting the the receiver along a line perpendicular to the left edge of the street. In the current scenario the parameters $\alpha_{\max},\ L,\ h_{T1},\ D, \sigma_0^2,\ \ \psi_R,\ \psi_T$ are equal to $\pi/2,\ 40\ m,\ 20\ m,\ 1\ m,\ 0.5,\ 0$ and 0, respectively. From Figure.3.9(a), it can be seen the as we increase the value of h_{R1} the ACF becomes more flat around the origin. Hence, the channel changes slowly for big values of h_{R1}. On the contrary, if the the value of h_{R1} is small the channel changes fast.

In the Figure.3.10(b), we illustrate the influence of the position of the transmitter relatively to the left hand side of the street, given by h_{T1}, on the absolute value of the ACF. By varying the value of h_{T1}, we are in fact shifting the the transmitter along a line perpendicular to the left edge of the street. In the current scenario the parameters $\alpha_{\max},\ L,\ h_{R1},\ D, \sigma_0^2,\ \ \psi_R,\ \psi_T$ are equal to $\pi/2,\ 40\ m,\ 20\ m,\ 1\ m,\ 0.5,\ 0$ and 0, respectively. From Figure.3.10(b), it can be seen the as we increase the value of h_{T1} the ACF becomes more flat around the origin. Hence, the channel changes slowly for big values of h_{T1}. On the contrary, if the the value of h_{T1} is small the channel changes fast.

Hence, the variation of h_{R1} or h_{T1} leads to the same effect. Nevertheless, the variation of h_{R1} has stronger influence on the absolute value of the ACF, as it can be seen from Figure.3.10.

In the Figure.3.11, we illustrate the influence of the direction of motion of the receiver given by ψ_R on the absolute value of the ACF. In the current scenario the parameters $\alpha_{\max},\ L,\ h_{R1}$,$h_{T1},\ D, \sigma_0^2,\ \psi_T$ are equal to $\pi/2,\ 20\ m,\ 10\ m,\ 10\ m,\ 20\ m,\ 0.5$, and 0, respectively. From Figure.3.11, it can be seen that for a value of ψ_R equals to π the most flat ACF is obtained. Hence the channel changes slowly if the

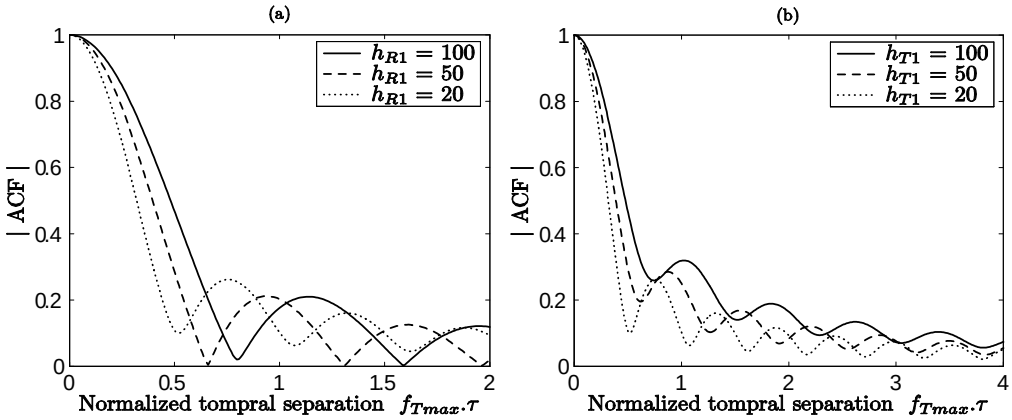

Figure 3.10: Absolute value of ACF: (a) for various values of h_{R1} and (b) or various values of h_{T1}.

transmitter and the receiver are moving toward each other. For a value of ψ_R equals to $\pi/2$, a very fast drop can be seen around the origin then the channel changes fast for this case. The plot of the ACF for a value of ψ_R equals to $3\pi/4$, shows that we can't reach a general conclusion about the effect of ψ_R on the absolute value of the ACF. In other words, we can't say that an increase in the value of ψ_R leads to a faster channel changes.

3.5 Level-Crossing Rate (LCR)

Let denote by $\zeta(t)$ the envelope of The channel gain $g(t)$, i.e., $\zeta(t) = |g(t)|$. The LCR, denoted by $N_\zeta(r)$, is the average number of crossings per second at which the envelope $\zeta(t)$ crosses a specified signal level r with positive (or negative) slope. The LCR is defined as

$$N_\zeta(r) = \int_0^\infty \dot{x}\ p_{\zeta\dot{\zeta}}(r, \dot{x}) d\dot{x} \tag{3.30}$$

where $p_{\zeta\dot{\zeta}}(r, \dot{x})$ denotes the joint probability density function of the process $\zeta(t)$ and its time derivative $\dot{\zeta}(t)$. In Section 3.1, it has been shown that the envelope $\zeta(t)$

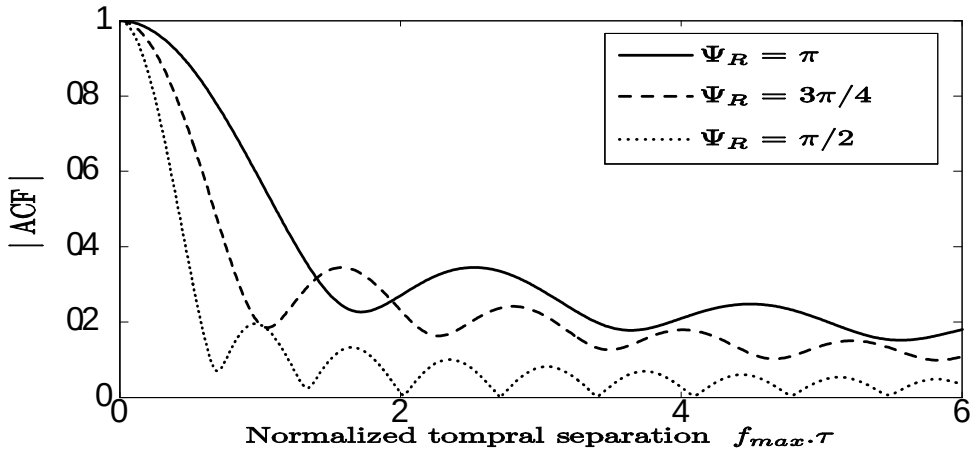

Figure 3.11: Absolute value of ACF for various values of ψ_R .

follows a Rayleigh distribution. Hence, the LCR of the Rayleigh process $\zeta(t)$ can be expressed as

$$N_\zeta(r) = \sqrt{\frac{\beta}{2\pi}} \cdot \frac{r}{\psi_0} e^{-\frac{r^2}{2\psi_0}} \tag{3.31}$$

where

$$\beta = -\ddot{\psi}_0 - \frac{\dot{\phi}_0^2}{\psi_0}. \tag{3.32}$$

The quantities ψ_0, $\ddot{\psi}_0$, and $\dot{\phi}_0$ are given by

$$\begin{aligned} \psi_0 &= r_{g_I g_I}(0) \\ &= \frac{1}{2}\,\mathrm{Re}\left\{r_{gg}(0)\right\} \\ &= \sigma_0^2 \end{aligned} \tag{3.33}$$

$$\begin{aligned} \ddot{\psi}_0 &= \frac{d^2}{d\tau^2} r_{g_I g_I}(\tau)\Big|_{\tau=0} \\ &= \frac{1}{2}\frac{d^2}{d\tau^2}\,\mathrm{Re}\left\{r_{gg}(\tau)\right\}\Big|_{\tau=0} \end{aligned} \tag{3.34}$$

$$\begin{aligned}\dot{\phi}_0 &= \frac{d^2}{d\tau^2} r_{g_I g_Q}(\tau)\Big|_{\tau=0} \\ &= \frac{1}{2}\frac{d^2}{d\tau^2}\,\mathrm{Im}\left\{r_{gg}(\tau)\right\}\Big|_{\tau=0} \end{aligned} \tag{3.35}$$

Hence, the LCR can now be evaluated. In order to illustrate the influence of different parameters on the LCR we present in the following obtained results for various scenarios. In the Figure.3.12(a), we illustrate the influence of the length of the cluster of scatters L on the LCR. In the current scenario, the parameters $\alpha_{\max}$, h_{T1}, h_{R1}, D, σ_0^2, ψ_R, ψ_T are equal to π, 5 m, 5 m, $15m$, 0.5, 0 and 0, respectively. From Figure.3.12(a), it can be seen the as we decrease the length of the cluster the LCR decreases. Hence, the channel changes slowly in case that the length of the cluster is small. On the contrary, if the length of the cluster increases the channel changes fast. which confirm the result obtained in the previous section.

In the Figure.3.12(b), we illustrate the influence of the position of the cluster of scatter given by $\alpha_{\max}$ on the LCR. In the current scenario the parameters L, h_{T1}, h_{R1}, D, σ_0^2, ψ_R, ψ_T are equal to 10 m, 10 m, 10 m, $2m$, 0.5, 0 and 0, respectively. From Figure.3.12(b), it can be seen that as we decrease the value of $\alpha_{\max}$ the LCR decreases. Hence, the channel changes slowly in case that the value of $\alpha_{\max}$ is small. On the contrary, the channel changes fast for large values of $\alpha_{\max}$. This statement confirm the result obtained when we have studied the ACF.

3.6 Average Duration of Fades (ADF)

The ADF, denoted by $T_{\zeta_-}(r)$, is the expected value for the length of time intervals over which the envelope $\zeta(t)$ is below a specified signal level r. The ADF is defined

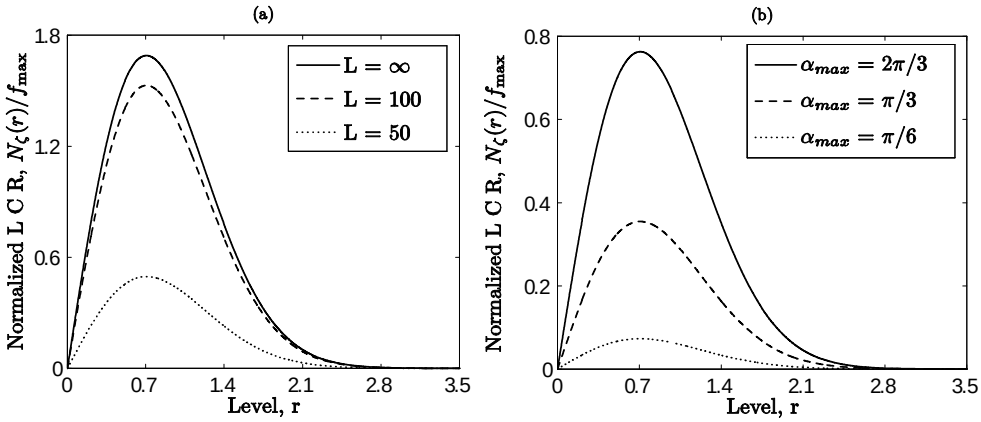

Figure 3.12: Normalized LCR: (a) for various values of L and (b) or various values of $\alpha_{\max}$.

as

$$T_{\zeta_-}(r) = \frac{F_{\zeta_-}(r)}{N_\zeta(r)} \tag{3.36}$$

where

$$F_{\zeta_-}(r) = \int_0^r p_\zeta(x)dx \tag{3.37}$$

Since $\zeta(t)$ follows a Rayleigh process, we can write

$$F_{\zeta_-}(r) = 1 - e^{-(r^2/2\psi_0)} \tag{3.38}$$

Hence, the ADF can be expressed as

$$T_{\zeta_-}(r) = \sqrt{\frac{2\pi}{\beta}} \cdot \frac{\psi_0}{r} \left(e^{(r^2/2\psi_0)} - 1\right) \tag{3.39}$$

In order to illustrate the influence of different parameters on the ADF we present in the following obtained results for various scenarios. In the Figure.3.13(a), we illustrate the influence of the length of the cluster of scatters L on the ADF. In the current scenario, the parameters $\alpha_{\max}$, h_{T1}, h_{R1}, D, σ_0^2, ψ_R, ψ_T are equal to π, 5 m, 5 m, $15m$, 0.5, 0 and 0, respectively. From Figure.3.13(a), it can be seen that as we

increase the length of the cluster the LCR increases. The maximum value of the ADF is reached for an infinite length cluster.

In the Figure.3.13(b), we illustrate the influence of the position of the cluster of scatter given by $\alpha_{\max}$ on the LCR. In the current scenario the parameters L, h_{T1}, h_{R1}, D, σ_0^2, ψ_R, ψ_T are equal to 10 m, 10 m, 10 m, $2m$, 0.5, 0 and 0, respectively. From Figure.3.13(b), it can be seen that as we decrease the value of $\alpha_{\max}$ the ADF decreases.

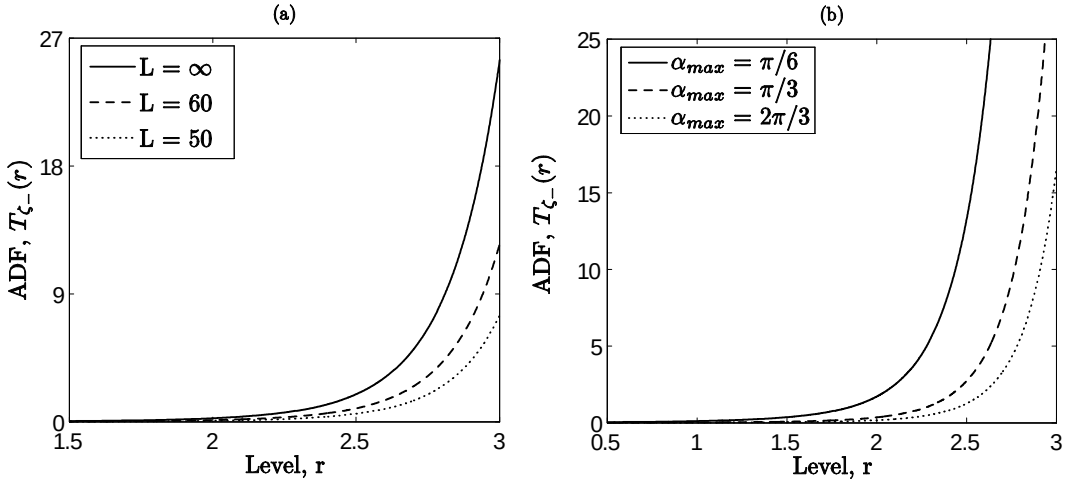

Figure 3.13: ADF: (a) for various values of L and (b) or various values of $\alpha_{\max}$.

Chapter 4

The SISO Simulation Model

Computer simulations are essential for the design optimization and test of mobile communication systems. In order to perform the necessary simulations for a given communication system, the realization of a channel simulator is required. In the reference model, an infinite number of scatter is assumed. Hence, the reference model cannot be used to realize a channel simulator. To overcome this problem a stochastic simulation model is derived from the reference model by limiting the number of scatter to a finite value N. Furthermore, a deterministic channel model can be obtained from the stochastic simulation model, by fixing all model parameters. Finally, appropriate parameter computation methods are used to determine the model parameters, such that the statistical properties of the simulation model and the reference model fit together. This procedure is an application for the concept of deterministic channel modelling described in [14].

4.1 The Stochastic Simulation Model

A stochastic simulation model can be derived from the reference model described in Chapter 3 by considering a finite number of scatters N. Thus, the diffuse component can be expressed as

$$\hat{g}(t) = \sum_{n=1}^{N} c_n \cdot e^{j(2\pi f_n t + \beta_n)} \tag{4.1}$$

The phases β_n are still i.i.d. random variables, each with a uniform distribution on the interval $[0, 2\pi)$. The amplitude c_n and the frequency f_n are constant, Therefore, $\hat{g}(t)$ represents a stochastic process. The diffuse component $\hat{g}(t)$ can be seen as a finite sum-of-sinusoids with constant gains, constant Doppler frequencies, and random phases.

4.1.1 Statistical Properties

In this section, the statistical properties of the stochastic simulation model are derived. The mean value of the stochastic simulation model can be evaluated by applying the expectation operator on the phase shifts β_n.Hence, the mean value can be expressed as

$$\hat{m}_g = E\{\hat{g}(t)\} = 0 \tag{4.2}$$

The ACF of the stochastic simulation model, which is defined as

$$\begin{aligned} \hat{r}_{gg}(\tau) &: = E\{\hat{g}^*(t)\hat{g}(t+\tau)\} \\ &= E\left\{ \begin{array}{l} \sum_{n=1}^{N}\sum_{m=1}^{M} c_n e^{-j(2\pi f_n t)} \\ \cdot c_m e^{j(2\pi f_m (t+\tau))} \cdot e^{-j(\beta_n - \beta_m)} \end{array} \right\} \end{aligned} \tag{4.3}$$

Let consider the random variable ξ given by $\xi = (\beta_n - \beta_m) \bmod 2\pi$. The random variable ξ is uniformly distributed over the interval $[0, 2\pi)$ for all values of m and n expect for $m = n$. When $m = n$, the random variable ξ is always equal to 0. Hence, we can write

$$E\{\xi\} = \left\{ \begin{array}{lll} 0 & \text{if} & n \neq m \\ 1 & \text{if} & n = m \end{array} \right. \tag{4.4}$$

This fact allow us to simplify the expression of the ACF as follow

$$\hat{r}_{gg}(\tau) = \sum_{n=1}^{N} c_n^2 \; e^{j(2\pi f_n \tau)} \tag{4.5}$$

The mean value of the stochastic process $\hat{g}(t)$ is constant, and that the ACF of $\hat{g}(t)$ depends only on the time separation τ. Hence, the stochastic process $\hat{g}(t)$ is wide sense stationary.

Now we derive the PSD of the stochastic simulation model, which is the Fourier Transform of the ACF. Hence, the PSD can be written as

$$\begin{aligned} \hat{S}_{gg}(f) &= F\{\hat{r}_{gg}(\tau)\} \\ &= \int_{-\infty}^{+\infty} \hat{r}_{gg}(\tau) e^{-j2\pi f \tau} d\tau \\ &= \sum_{n=1}^{N} c_n^2 \; \delta(f - f_n) \end{aligned} \tag{4.6}$$

where $F\{\cdot\}$ denotes the Fourier transform and $\delta(\cdot)$ denotes the delta function.

The average Doppler shift of the stochastic simulation model can be expressed as

$$B_{gg}^{(1)} = \frac{\int_{-\infty}^{+\infty} f \hat{S}_{gg}(f) df}{\int_{-\infty}^{+\infty} \hat{S}_{gg}(f) df} \tag{4.7}$$

$$= \frac{\int_{-\infty}^{+\infty} f \sum_{n=1}^{N} c_n^2 \; \delta(f - f_n) df}{\int_{-\infty}^{+\infty} \sum_{n=1}^{N} c_n^2 \; \delta(f - f_n) df} \tag{4.8}$$

$$= \frac{\sum_{n=1}^{N} c_n^2 \; f_n}{\sum_{n=1}^{N} c_n^2} \tag{4.9}$$

The Doppler spread $B_{gg}^{(2)}$ of the stochastic simulation model can be expressed as

$$\begin{aligned} B_{gg}^{(2)} &= \sqrt{\frac{\int_{-\infty}^{+\infty} (f - B_{gg}^{(1)})^2 \hat{S}_{gg}(f) df}{\int_{-\infty}^{+\infty} \hat{S}_{gg}(f) df}} \\ &= \sqrt{\frac{\sum_{n=1}^{N} c_n^2 (f_n - B_{gg}^{(1)})^2}{\sum_{n=1}^{N} c_n^2}} \end{aligned} \tag{4.10}$$

The level-crossing rate of the stochastic simulation model can be expressed as

$$N_\zeta(r) = \sqrt{\frac{\beta}{2\pi}} \cdot \frac{r}{\psi_0} e^{-\frac{r^2}{2\psi_0}} \tag{4.11}$$

where

$$\beta = -\ddot{\psi}_0 - \frac{\dot{\phi}_0^2}{\psi_0}. \tag{4.12}$$

The quantities ψ_0, $\ddot{\psi}_0$, and $\dot{\phi}_0$ are given by

$$\begin{aligned} \psi_0 &= \hat{r}_{g_I g_I}(0) \\ &= \frac{1}{2}\operatorname{Re}\{\hat{r}_{gg}(0)\} \\ &= \frac{1}{2}\sum_{n=1}^{N} c_n^2 \end{aligned} \tag{4.13}$$

$$\begin{aligned} \ddot{\psi}_0 &= \frac{d^2}{d\tau^2}\hat{r}_{g_I g_I}(\tau)\Big|_{\tau=0} \\ &= \frac{1}{2}\frac{d^2}{d\tau^2}\operatorname{Re}\{\hat{r}_{gg}(\tau)\}\Big|_{\tau=0} \\ &= -\frac{1}{2}\sum_{n=1}^{N} c_n^2 (2\pi f_n)^2 \end{aligned} \tag{4.14}$$

$$\begin{aligned} \dot{\phi}_0 &= \frac{d^2}{d\tau^2}\hat{r}_{g_I g_Q}(\tau)\Big|_{\tau=0} \\ &= \frac{1}{2}\frac{d^2}{d\tau^2}\operatorname{Im}\{\hat{r}_{gg}(\tau)\}\Big|_{\tau=0} \\ &= \sum_{n=1}^{N} \pi c_n^2 f_n \end{aligned} \tag{4.15}$$

The ADF of the stochastic simulation model can be expressed as

$$T_{\zeta_-}(r) = \frac{F_{\zeta_-}(r)}{N_\zeta(r)} \tag{4.16}$$

$$= \sqrt{\frac{2\pi}{\beta}} \cdot \frac{\psi_0}{r}\left(e^{\frac{r^2}{2\psi_0}} - 1\right) \tag{4.17}$$

4.1.2 Ergodicity

In this section, we study the ergodicity of the stochastic process $\hat{g}(t)$. If a process is mean value ergodic, then it is possible to evaluate its mean value using temporal average over one sample function instead of averaging over the whole ensemble of sample functions. The same statement holds for the evaluation of the autocorrelation function if the process is autocorrelation ergodic.

We start first by checking the ergodicity with respect to the mean value. The statistical average $\hat{m}_g$ of $\hat{g}(t)$ has been evaluated in the previous section and is equal to 0. The temporal average $\tilde{m}_g$ of $\hat{g}(t)$ is defined as

$$\tilde{m}_g := \langle \hat{g}(t) \rangle$$

$$= \lim_{T \longrightarrow \infty} \frac{1}{2T} \int_{-T}^{T} \hat{g}(t)dt \tag{4.18}$$

$$= \lim_{T \longrightarrow \infty} \frac{1}{2T} \sum_{n=1}^{N} c_n \cdot \int_{-T}^{T} e^{j(2\pi f_n t + \beta_n)} dt$$

$$= 0 \tag{4.19}$$

where $\langle \cdot \rangle$ stands for the time average operator. Hence, $\tilde{m}_g = \hat{m}_g$ and the stochastic process $\hat{g}(t)$ is mean value ergodic.

Now let examine if the process $\hat{g}(t)$ is autocorrelation ergodic. The ACF of $\hat{g}(t)$ is given by

$$\hat{r}_{gg}(\tau) = \sum_{n=1}^{N} c_n^2 \; e^{j(2\pi f_n \tau)} \tag{4.20}$$

as shown in the previous section. The temporal ACF of $\hat{g}(t)$ is given by

$$\begin{aligned}
\tilde{r}_{gg}(\tau) &: = \langle \hat{g}^*(t)\hat{g}(t+\tau)\rangle \\
&= \lim_{T\longrightarrow\infty}\frac{1}{2T}\int_{-T}^{T}\hat{g}^*(t)\hat{g}(t+\tau)dt \qquad (4.21)\\
&= \lim_{T\longrightarrow\infty}\frac{1}{2T}\int_{-T}^{T}\sum_{n=1}^{N}\sum_{m=1}^{M} c_n e^{-j(2\pi f_n t+\beta_n)}\cdot c_m e^{j(2\pi f_m(t+\tau)+\beta_m)} \\
&= \sum_{n=1}^{N} c_n^2\ e^{j(2\pi f_n\tau)}. \qquad (4.22)
\end{aligned}$$

Hence, $\tilde{r}_{gg}(\tau) = \hat{r}_{gg}(\tau)$ and the stochastic process $\hat{g}(t)$ is mean autocorrelation ergodic.

4.2 The Deterministic Simulation Model

A sample function of the stochastic process $\hat{g}(t)$ is obtained by choosing constant phases β_n, determined by the outcomes of a random generator with uniform distribution over $[0, 2\pi)$. To realize a stochastic process, an infinite number of sample functions is needed, which makes it non-realizable. We can cope with this problem, since we are dealing with an ergodic stochastic process. In such a situation, a single sample function denoted by $\tilde{g}(t)$ is sufficient. The realization of $\tilde{g}(t)$ represents the *deterministic simulation model* for an M2M SISO frequency-nonselective Rayleigh fading channel. Time averages has to be used in order to analyse the properties of the deterministic MIMO channel simulator. For instance, the ACF of the deterministic simulation model is defined as

$$\begin{aligned}
\tilde{r}_{gg}(\tau) &: = \langle \tilde{g}^*(t)\tilde{g}(t+\tau)\rangle \\
&= \sum_{n=1}^{N} c_n^2\ e^{j(2\pi f_n\tau)}. \qquad (4.23)
\end{aligned}$$

4.3 Parameter Computation Method

In order to obtain a channel simulator that emulates the statistical fading behaviour of the M2M SISO channel with great deal of precision, parameter computation methods are invoked. A good parameter computation method is the one that lead to a good fitting between the statistical properties of the simulation model and the reference model. In our current problem the model parameters that has to be determined are only the Doppler frequencies f_n. The Doppler gains has the same expression as in the reference model and are given by (3.2). In the following we present the parameter computation methods used to determine the simulation model parameters for the SISO M2M channel.

4.3.1 Modified Method of Equal Area

The method of equal area (MEA) has been described in detail in [14]. To determine the value of the model parameters f_n, let consider the PSD $S_{gg}(f)$ of a complex channel gain $g(t)$. In our reference model, the PSD is generally asymmetrical and bounded within the interval $[f_l, f_u]$. To determine the value of the model parameters f_n, we divide the area under the PSD into N equal areas. This could be done by evaluating the set of frequencies $\{f_n\}_{n=1}^{N}$ in such a way that

$$\int_{f_l}^{f_n} S_{gg}(f)df = \frac{2\sigma_0^2 n}{N}, \qquad \forall n = 1,\ 2,\ ...,\ N \tag{4.24}$$

where $2\sigma_0^2$ is the mean power of the received scattered component. Numerical technics could be used to evaluate the Doppler frequencies f_n.

The Modified MEA is similar to the MEA method except the fact that we have to divide the area under the PSD into $2N$ subarea. Only the odd frequencies will be

used in the simulation model i.e.,

$$\int_{f_l}^{f_n} S_{gg}(f)df = \frac{2\sigma_0^2(2n-1)}{2N}, \qquad \forall n = 1,\ 2,\ ...,\ N. \tag{4.25}$$

The obtained set of Doppler frequencies $\{f_n\}_{n=1}^{N}$ is used in the simulation model.

4.3.2 *Lp*-Norm Method (LPNM)

The LPNM has been described in detail in [14]. To determine the set of frequencies $\{f_n\}_{n=1}^{N}$ using the LPNM method, It is required to minimize the following error norm:

$$E = \left\{ \frac{1}{\tau_{\max}} \int_0^{\tau_{\max}} |r_g(\tau) - \tilde{r}_g(\tau)|^p \, d\tau \right\}^{1/p} \tag{4.26}$$

the quantity $\tau_{\max}$ determine the range over which the approximation is $r_g(\tau) \approx \tilde{r}_g(\tau)$ is of interest.

4.4 Numerical and Simulation Results

In order to asses the performance of the MMEA and the LPNM method, we cosider a scenario where the parameters $\alpha_{\max}$, L, h_{T1}, h_{R1}, D, σ_0^2, ψ_R, ψ_T are equal to $\pi/2$, , 2 m, 10 m, 10 m, 20m, 0.5, 0 and 0, respectively. The results illustrated in Figure.4.1 are obtained using the MMEA. The results illustrated in Figure.4.2 are obtained using the *Lp*-norm method.

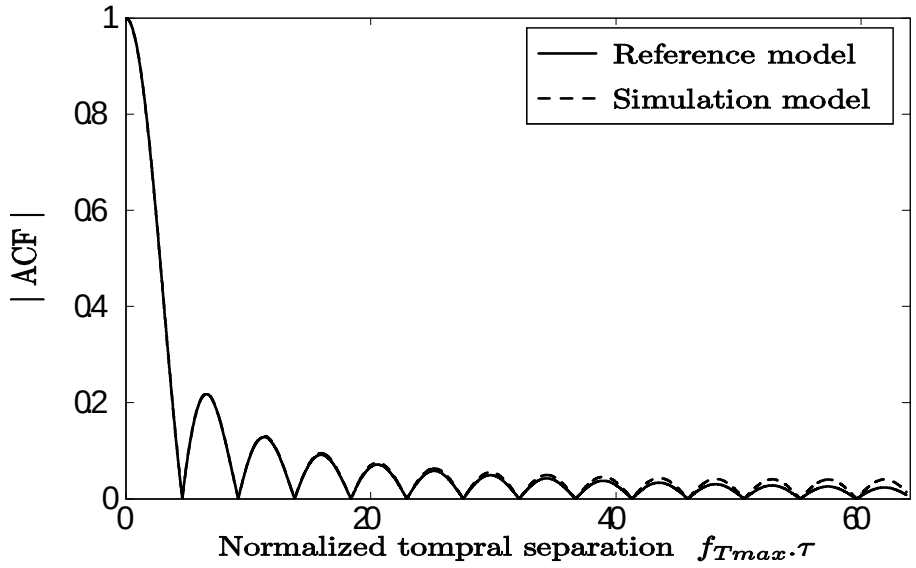

Figure 4.1: ACFs of the reference and the simulation model (MMEA $N = 25$).

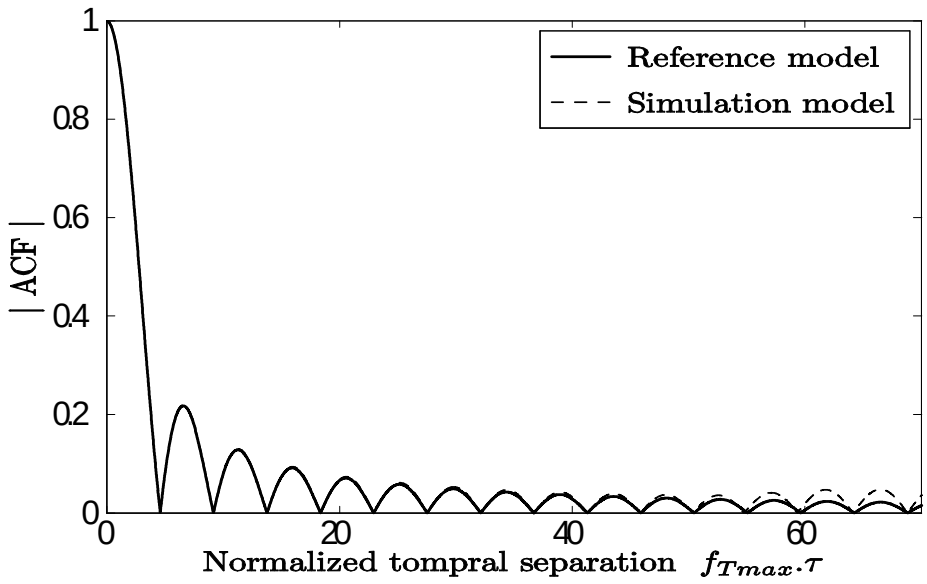

Figure 4.2: ACFs of the reference and the simulation model (Lp-norm method $N = 25$).

Chapter 5

Model Extension

In this chapter, we will illustrate how the proposed SISO channel model can be extended to multiple clusters of scatter as well as to frequency-selectivity.

5.1 Extension to Multiple Clusters of Scatters

We consider a propagation scenario where $\mathcal{C}$ clusters of scatters located on the left and/or right hand side of the street. In order to distinguish between different clusters a subscript $(\cdot)_c$ ($c = 1,\ 2,\ ...,\ \mathcal{C}$) is added to all affected symbols $g_c(t),\ \alpha_c,\ \theta_c$ etc. We start by deriving the statistical properties of the multi-cluster scenario. Afterward, numerical and simulation results are presented.

5.1.1 Statistical Properties

the PDF $p_\alpha(\alpha)$ of the AOD α in a multi-cluster propagation scenario can be expressed as

$$p_\alpha(\alpha) = \sum_{c=1}^{\mathcal{C}} b_c p_{\alpha_c}(\alpha_c). \tag{5.1}$$

where b_c is a weighting factor. Since the area under the PDF $p_\alpha(\alpha)$ is equal to 1, we need to impose the boundary condition $\sum_{c=1}^{\mathcal{C}} b_c = 1$. The expression of the weighting factor must reflect the contribution of each cluster in the received scattered

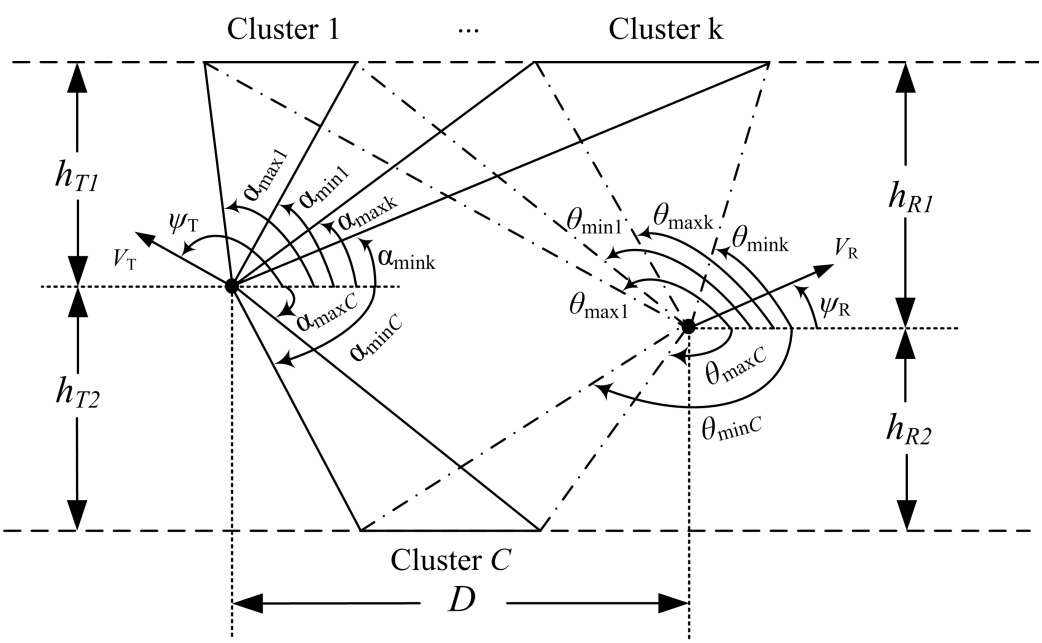

Figure 5.1: Geometrical street model with several clusters of scatters.

component. One may think that the contribution of each cluster is proportional to its length L, which is not right. In fact, if we place a cluster of a length L near to the transmitter (e.g.,$\alpha_{\max} \approx \pi/2$) it has higher contribution than a cluster of length L located far from the transmitter (e.g.,$\alpha_{\max} \approx \pi$). Since the transmitter is equipped with an omnidirectional antenna, we can conclude that the contribution of a given cluster is proportional to the angle of spreading $\Delta\alpha_c$ given by $\Delta\alpha_c = |\alpha_{\max\, c} - \alpha_{\min\, c}|$. Hence, we can express b_c as

$$b_c = \frac{\Delta\alpha_c}{\sum_{c=1}^{\mathcal{C}} \Delta\alpha_c}. \tag{5.2}$$

The PDF $p_\theta(\theta)$ of the AOA θ in a multi-cluster propagation scenario can be expressed as

$$p_\theta(\theta) = \sum_{c=1}^{\mathcal{C}} b_c p_{\theta_c}(\theta_c). \tag{5.3}$$

where b_c is the same weighting factor used for the PDF of the AOD α.

In a multi-cluster propagation scenario the complex channel gain denoted by $z(t)$ results from the superposition of the received scattered components of all $\mathcal{C}$ clusters. Hence, the complex channel gain $z(t)$ can be expressed as

$$z(t) = \sum_{c=1}^{\mathcal{C}} w_c g_c(t) \tag{5.4}$$

where w_c is a weighting factor. We impose the boundary condition $\sum_{c=1}^{\mathcal{C}} w_c = 1$, in order to normalize the mean power of $z(t)$ to $2\sigma_0^2$. A relation between b_c and w_c will be established later. Thus, the ACF in the multi-cluster case can be expressed as

$$\begin{aligned} r_{zz}(\tau) &= E\left\{z^*(t)z(t+\tau)\right\} \\ &= E\left\{\sum_{c=1}^{\mathcal{C}}\sum_{d=1}^{\mathcal{C}} w_c g_c^*(t) w_d g_d(t+\tau)\right\} \\ &= \sum_{c=1}^{\mathcal{C}}\sum_{d=1}^{\mathcal{C}} w_c w_d E\left\{g_c^*(t) g_d(t+\tau)\right\} \end{aligned} \tag{5.5}$$

Since the effect of different clusters are independent, we can write $E\left\{g_c^*(t)g_d(t+\tau)\right\} = E\left\{g_c^*(t)\right\} E\left\{g_d(t+\tau)\right\}$ if $c \neq d$. As shown in Section 3.1, the expected value of the channel gain is equal to zero. Hence, the expression of $r_{zz}(\tau)$ can be simplified as

$$r_{zz}(\tau) = \sum_{c=1}^{\mathcal{C}} w_c^2 \cdot r_{g_c g_c}(\tau) \tag{5.6}$$

$$= 2\sigma_0^2 \int_{\alpha_{\min}}^{\alpha_{\max}} e^{j(2\pi(f_T(\alpha)+f_R(\theta(\alpha)))\tau)} p_\alpha(\alpha)\, d\alpha. \tag{5.7}$$

The expression of the ACF $r_{g_c g_c}(\tau)$ is given by

$$r_{g_c g_c}(\tau) = 2\sigma_0^2 \int_{\alpha_{\min c}}^{\alpha_{\max c}} e^{j(2\pi(f_T(\alpha_c)+f_R(\theta_c(\alpha_c)))\tau)} p_{\alpha_c}(\alpha_c)\, d\alpha_c \tag{5.8}$$

Substituting (5.8) in (5.6), it can be proven that w_c and b_c are related according to the relation

$$w_c^2 = b_c. \tag{5.9}$$

The PSD $S_{zz}(f)$ can be obtained by applying the inverse Fourier transform on the ACF $r_{zz}(\tau)$. Hence, the PSD can be expressed

$$\begin{aligned} S_{zz}(f) &= F^{-1}\{r_{zz}(\tau)\} \\ &= F^{-1}\left\{\sum_{c=1}^{\mathcal{C}} w_c^2 \cdot r_{g_c g_c}(\tau)\right\} \\ &= \sum_{c=1}^{\mathcal{C}} w_c^2 \cdot S_{g_c g_c}(f) \end{aligned} \tag{5.10}$$

where $F^{-1}\{\cdot\}$ stands for the inverse Fourier transform.

5.1.2 Numerical and Simulation Results

To illustrate the statistical properties of a multi-cluster propagation case, we consider a scenario with two clusters. The first cluster is located on the left hand side of the street ($\alpha_{\max} = 90°$) having a length $L = 5m$. The second cluster is located on the right hand side of the street ($\alpha_{\max} = -21.81°$). The distance separating the transmitter and the receiver from both scatter is equal to $2m$. The value of $\tau_{\max} is$ equal to 0.055 s. For the described scenario, we represent the PDF of AOA and the power spectral density in Figure.5.2 and Figure.5.3 ,respectively. In addition, the ACF of the reference and the simulation model is illustrated in Figure.5.4 ,where the MMEA is used to determine the model parameters. In Figure.5.5 ,the ACF of the simulation model is obtained using the *Lp*-norm method. A better performance can be observed when using the *Lp*-norm method.

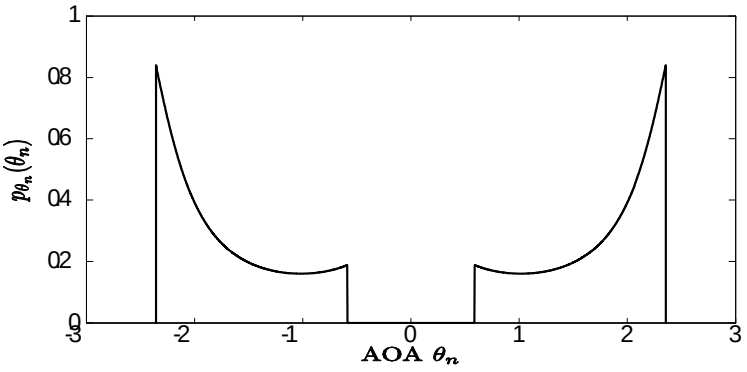

Figure 5.2: PDF of AOA for a multi-cluster scenario.

5.2 Extension to Frequency-Selectivity

So far, all the presented scenarios can be classified in the category of frequency non-selective channels. In real-world, the multipath propagation results in received waves having different propagation delays and different path gains. The hypothesis of frequency non-selectivity is justified only if the propagation delays can be neglected in comparison to the symbol duration. This statement holds for narrowband transmission systems. In wideband transmission systems the symbol duration is much smaller than in narrowband transmission systems. In such cases, we cannot any more neglect the propagation delays. This fact results in another category of channels so-called frequency non-selective channels. In this Section, a wide-sense stationary uncorrelated scattering (WSSUS) model is assumed.

5.2.1 The Reference Model

We consider a propagation scenario with $\mathcal{L}$ discrete propagation paths. In order to distinguish between different paths, a subscript $(\cdot)_\ell$ ($\ell = 1,\ 2,\ ...,\ \mathcal{L}$) is added to all affected symbols. The ℓth path introduces a gain a_ℓ and a propagation delay τ'_ℓ. The

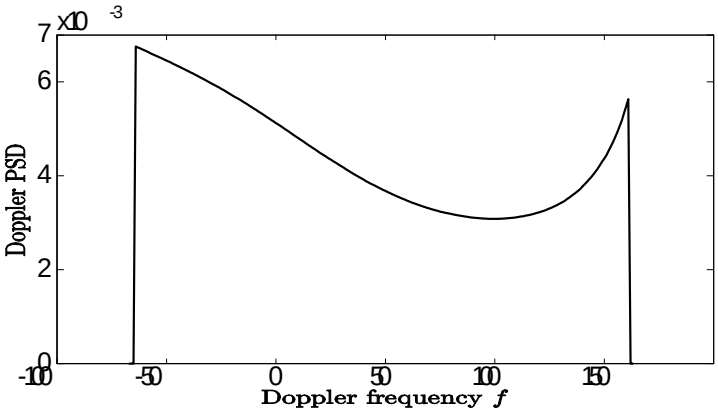

Figure 5.3: PSD for a multi-cluster scenario.

complex channel gain associated with the ℓth path is denoted by $g_\ell(t)$. The impulse response of the reference model can be expressed as

$$h(\tau', t) = \sum_{\ell=1}^{\mathcal{L}} a_\ell g_\ell(t) \delta(\tau' - \tau'_\ell) \tag{5.11}$$

where $\delta(\cdot)$ is the delta function.

The time-variant transfer function denoted by $H(f', t)$ can be obtained by applying the Fourier transform on the impulse response $h(\tau', t)$ with respect to τ'. Hence, using (5.11), we can write

$$H(f', t) = \sum_{\ell=1}^{\mathcal{L}} a_\ell g_\ell(t) e^{-j2\pi f' \tau'_\ell} \tag{5.12}$$

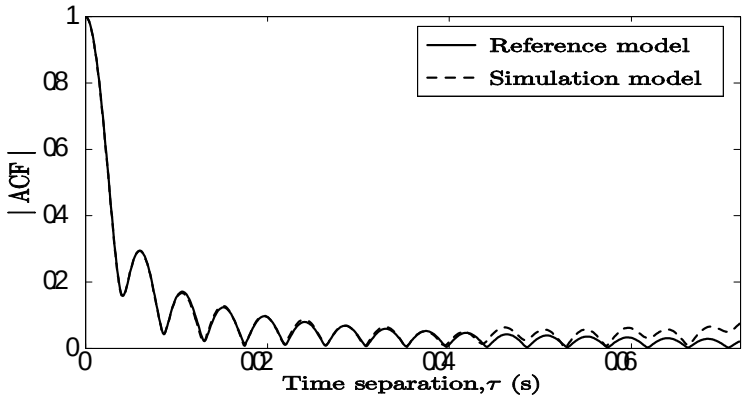

Figure 5.4: ACFs of the reference and the simulation model for a multi-cluster scenario (MMEA, $N = 25$).

Using the expression of $H(f', t)$, we can determine the frequency correlation function (FCF) denoted by $r_{\tau'}(\upsilon')$, which is defined as

$$r_{\tau'}(\upsilon') \quad : \quad = E\left\{H^*(f', t)H(f' + \upsilon', t)\right\} \tag{5.13}$$

$$= \quad E\left\{\sum_{\ell=1}^{\mathcal{L}} a_\ell g_\ell^*(t) e^{j2\pi f'\tau'_\ell} \sum_{k=1}^{\mathcal{L}} a_k g_k(t) e^{-j2\pi(f'+\upsilon')\tau'_k}\right\} \tag{5.14}$$

$$= \quad \sum_{\ell=1}^{\mathcal{L}} \sum_{k=1}^{\mathcal{L}} a_\ell a_k e^{j2\pi f'\tau'_\ell} e^{-j2\pi(f'+\upsilon')\tau'_k} E\left\{g_\ell^*(t) g_k(t)\right\} \tag{5.15}$$

Since a WSSUS model is assumed, different paths are uncorrelated and we can write

$$E\left\{g_\ell^*(t) g_k(t)\right\} = \begin{cases} 0 & \text{if} \quad \ell \neq k \\ 2\sigma_0^2 & \text{if} \quad \ell = k \end{cases} \tag{5.16}$$

Hence, it follows

$$r_{\tau'}(\upsilon') = 2\sigma_0^2 \sum_{\ell=1}^{\mathcal{L}} a_\ell^2 e^{-j2\pi\upsilon'\tau'_\ell}. \tag{5.17}$$

The values of a_ℓ and τ'_ℓ can be obtained from specification or measurement data. Inter-vehicle communication systems are intended to operate the 5.9 GHz band. For

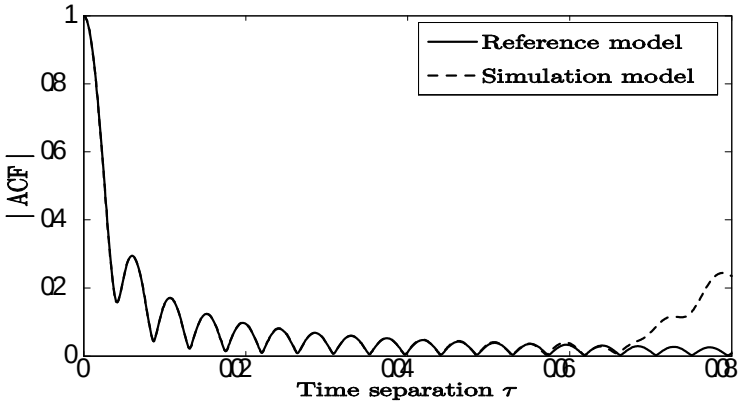

Figure 5.5: ACFs of the reference and the simulation model for a multi-cluster scenario (Lp-norm method, $N = 25$).

this band there exists no power delay profile specification. For this reason, we will use the COST 207 specification [23], originally designed for GSM. The choice of this specification is due to the fact that COST 207 is designed for outdoor propagation environment. In fact, inter-vehicle communication systems are intended to operate in an outdoor environment. The power delay profile of a 12-path channel model according to COST 207 is illustrated in Table.5.1.

Path	Delay (μs)	Fractional power	Path	Delay (μs)	Fractional power
1	0.0	0.092	7	1.3	0.046
2	0.1	0.115	8	1.7	0.074
3	0.3	0.231	9	2.3	0.051
4	0.5	0.127	10	3.1	0.032
5	0.8	0.115	11	3.2	0.018
6	1.1	0.074	12	5.0	0.025

Table 5.1: Specification of the PDP for Typical Urban channel according to COST 207 (12-path)

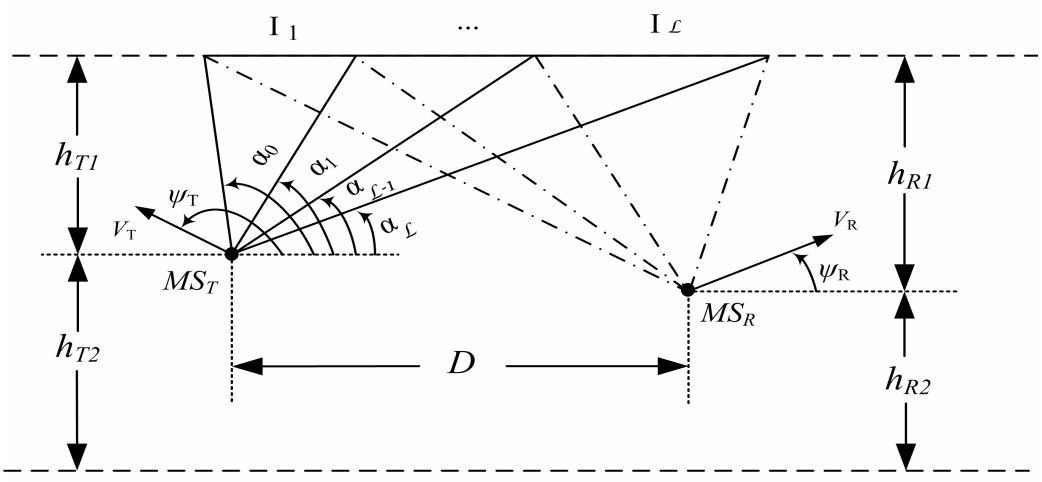

Figure 5.6: Partition of a cluster of scatters into $\mathcal{L}$ pairs.

5.2.2 The Simulation Model

In order to extend the simulation model to frequency selectivity let consider a cluster of length L. If we first assume that the channel is frequency non-selective, then the channel complex gain of the simulation model could be written as

$$\tilde{g}(t) = \sqrt{\frac{2\sigma_0^2}{N}} \sum_{n=1}^{N} d_n \cdot e^{j\left(2\pi(f_T^{(n)}+f_R^{(n)})t+\beta_n\right)}. \tag{5.18}$$

We remind that

$$d_n = e^{-j\frac{2\pi}{\lambda}((h_{T1}/\sin(\alpha_n))+(h_{R1}/\sin(\theta_n)))} \tag{5.19}$$

$$f_T^{(n)} = f_{T_{\max}} \cos(\alpha_n - \psi_T) \tag{5.20}$$

$$f_R^{(n)} = f_{R_{\max}} \cos(\theta_n - \psi_R). \tag{5.21}$$

Let partition the cluster into $\mathcal{L}$ pairs of segments I_ℓ ($\ell = 1,\ 2,\ ...,\ \mathcal{L}$) limited by α_ℓ and $\alpha_{\ell-1}$ as it is shown in Figure.5.6.

Each pair of segment correspond to a propagation path ℓ. In order to determine the gain a_ℓ and a propagation delay τ'_ℓ associated to each segment we use the following procedure. We first express the propagation delay as

$$\tau'_n = \frac{d_n}{c_0} \tag{5.22}$$

$$= \frac{e^{-j\frac{2\pi}{\lambda}((h_{T1}/\sin(\alpha_n))+(h_{R1}/\sin(\theta_n)))}}{c_0} \tag{5.23}$$

where c_0 is the speed of light. We remind that the AOD α_n and the AOA θ_n are related according to (2.1). Substituting θ_n in the expression of τ'_n, we can express τ'_n as a function of the AOD α_n $\tau'_n = h(\alpha_n)$. Hence, for a given τ'_ℓ we can determine the corresponding AOD α_ℓ. Unfortunately, no close form solution exists for α_ℓ, to overcome this problem numerical technics are used to evaluate α_ℓ. The angle α_ℓ determine the limit of each segment I_ℓ. Now, for all the AOD α_n within the interval $[\alpha_{\ell-1}, \alpha_\ell]$, we perform the following assignments:

$$\tau'_n \rightarrow \tau'_\ell \tag{5.24}$$

$$d_n \rightarrow d_{n,\ell} \tag{5.25}$$

$$f_T^{(n)} \rightarrow f_T^{(n,\ell)} \tag{5.26}$$

$$f_R^{(n)} \rightarrow f_R^{(n,\ell)} \tag{5.27}$$

$$\beta_n \rightarrow \beta_{n,\ell} \tag{5.28}$$

where $n = 1,\ 2,\ ...,\ N$ and $\ell = 1,\ 2,\ ..., \mathcal{L}$. Using this procedure, we are in fact gathering all the propagation delays τ'_n which are within the interval $\left[\tau'_{\ell-1}, \tau'_\ell\right]$ together. In fact, the difference between the delays $\tau'_{\ell-1} \leq \tau'_n \leq \tau'_\ell$ can be neglected. Hence, we assign to the corresponding propagation path a delay τ'_ℓ and a gain a_ℓ for all $\ell = 1, 2, ..., \mathcal{L}$. In this manner, we partition the N scatters $S^{(n)}$ into $\mathcal{L}$ pairs

of segment. Each pair contains N_ℓ scatters. We have to verify that the relation $\sum_{\ell=1}^{\mathcal{L}} N_\ell = N$ holds. The described procedure has been proposed in[**?**]. Following this procedure, the simulation model channel gain $\tilde{g}(t)$ given by (5.18) can be now used to express the impulse response of the frequency-selective SISO simulation model as

$$\tilde{h}(\tau', t) = \sum_{\ell=1}^{\mathcal{L}} a_\ell \sqrt{\frac{2\sigma_0^2}{N_\ell}} \sum_{n=1}^{N_\ell} d_{n,\ell} \cdot e^{j\left(2\pi(f_T^{(n,\ell)} + f_R^{(n,\ell)})t + \beta_{n,\ell}\right)} \delta(\tau' - \tau'_\ell) \tag{5.29}$$

The time-variant transfer function of the simulation model denoted by $\tilde{H}(f', t)$ can be obtained by applying the Fourier transform on the impulse response $\tilde{h}(\tau', t)$ with respect to τ'. Hence, we can write

$$\tilde{H}(f', t) = \sum_{\ell=1}^{\mathcal{L}} a_\ell \sqrt{\frac{2\sigma_0^2}{N_\ell}} \sum_{n=1}^{N_\ell} d_{n,\ell} \cdot e^{j\left(2\pi(f_T^{(n,\ell)} + f_R^{(n,\ell)})t + \beta_{n,\ell}\right)} e^{-j2\pi f' \tau'_\ell} \tag{5.30}$$

Using the expression of $\tilde{H}(f', t)$, we can determine the FCF of the simulation model, denoted by $\tilde{r}_{\tau'}(\upsilon')$, which is defined as

$$\begin{aligned} \tilde{r}_{\tau'}(\upsilon') &: = \left\langle \tilde{H}^*(f', t) \tilde{H}(f' + \upsilon', t) \right\rangle \\ &= 2\sigma_0^2 \sum_{\ell=1}^{\mathcal{L}} a_\ell^2 e^{-j2\pi\upsilon'\tau'_\ell}. \end{aligned} \tag{5.31}$$

One can observe that the FCF of the simulation model, given by (5.31), and the FCF of the reference model, given by (5.17), are equals. In Figure.5.7, the absolute value of the FCF is evaluated for both the reference model and the simulation model. From this figure a good fitting between the FCF of the reference model and the FCF of the simulation model can be seen. The values of the path gain a_l, and the path delay τ'_ℓ are obtained from COST 207 (12-path) shown in Table.5.1.

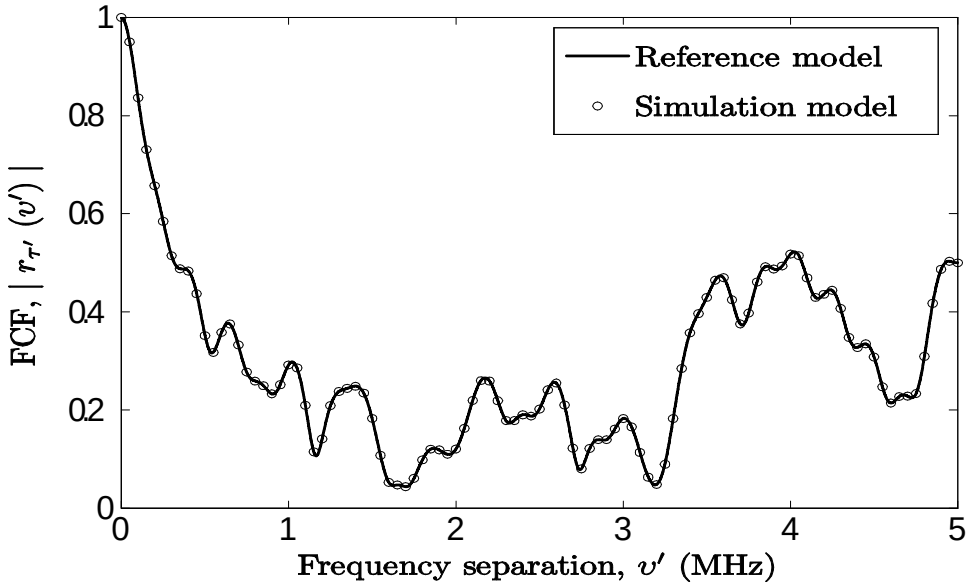

Figure 5.7: Absolute value of the FCFs $|r_{\tau'}(\upsilon')|$ (reference model) and $|\tilde{r}_{\tau'}(\upsilon')|$ (simulation model) according to the 12-path TU COST 207.

Chapter 6

The Mobile-to-Mobile MIMO Channel

In this chapter, an original M2M MIMO channel model is investigated. This investigation is driven by the fact that MIMO channels are attracting more and more attention thanks to their large capacity. This feature is needed for high data rate applications. The gain of capacity offered by MIMO channels over traditional SISO channels is illustrated in [24,25]. Furthermore, multielement antennas can be placed on car roofs, which makes MIMO channels very attractive for inter-vehicle communications. The scattering environment is modelled by the geometric street scattering model. This geometrical model allows the establishment of the exact relationship between the AOA and the AOD. This relationship is taken into account for the derivation of the reference model. Starting from the reference model, and applying the concept of deterministic channel modelling [14], a simulation model for an M2M channel is developed. Moreover, the statistical properties of both the reference and the simulation model are studied. Analytical solutions are provided for the 3D space-time CCF, the 2D space CCF, and the temporal ACF.

6.1 The Geometric Street Scattering Model

The geometrical street model for a MIMO M2M channel is the starting point for the derivation of the proposed M2M MIMO channel model. The geometrical street model for a MIMO channel is very similar to the geometrical model for a SISO channel. Nevertheless, it has to be mentioned that for MIMO channel the transmitter and the receiver are equipped with multielement antennas. The geometrical street model for a MIMO M2M channel is illustrated in Figure.6.1. The symbol MS_T in Figure.6.1 denotes the mobile transmitter, while MS_R plays the role of the mobile receiver. Moreover, the transmitter (receiver) is equipped with M_T (M_R) antenna elements, constituting a uniform linear antenna array. The antenna element spacing at the receiver and the transmitter antenna are denoted by δ_T and δ_R, respectively.

It is assumed that the transmitter antenna dimensions are small compared to the quantity $\min\{h_{T1}, h_{T2}\}$. Analogously, the receiver antenna dimension are small compared to the quantity $\min\{h_{R1}, h_{R2}\}$. Consequently, the following inequalities $(M_T - 1)\,\delta_T \ll \min\{h_{T1}, h_{T2}\}$ and $(M_R - 1)\delta_R \ll \min\{h_{R1}, h_{R2}\}$ hold. The angle γ_T (γ_R) describes the tilt angle of the transmit (receive) antenna array.

6.2 The Reference Model

6.2.1 Derivation of the Reference Model

The geometric street model presented in Figure.6.1 describes the scattering geometric street model for the M2M MIMO channel, which constitutes the starting point for the derivation of the reference model. From this figure it can be seen that the n^{th} plane wave emitted from the l^{th} transmit antenna element $A_T^{(l)}(l = 1, 2, \ldots, M_T)$ travels over the n^{th} scatter $S^{(n)}(n = 1, 2, \ldots, N)$ before arriving at the k^{th} receive an-

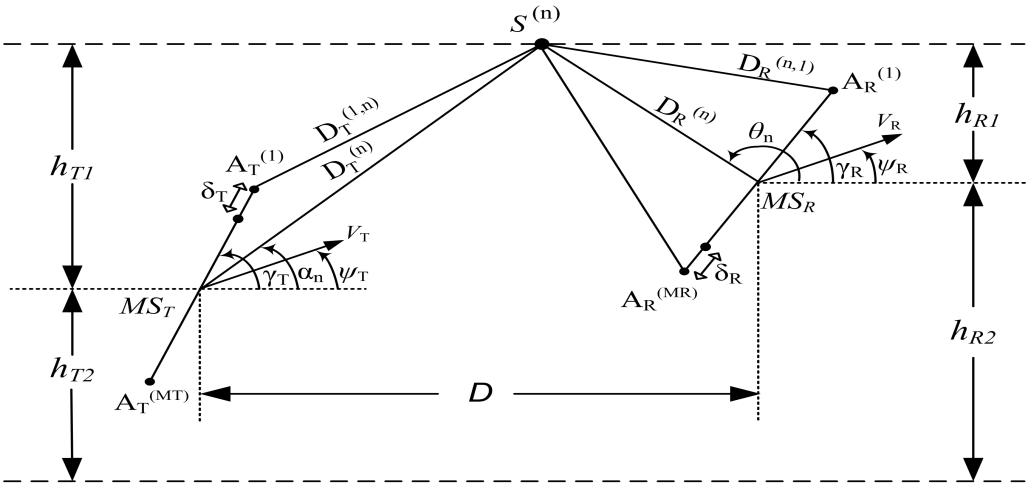

Figure 6.1: Geometric street scattering model for an $M_T \times M_R$ MIMO channel.

tenna element $A_R^{(k)}(k = 1, 2, \ldots, M_R)$. It is assumed that the number of scatters is infinite. Consequently, the diffuse component as seen from the receiver side is composed of an infinite number of homogenous plane waves. Considering the geometrical model in Figure.6.1, the link between the l^{th} transmit antenna element $A_T^{(l)}$ and the k^{th} receive antenna element $A_R^{(k)}$ can be described by its complex channel gain given by

$$g_{kl}(\vec{r}_T, \vec{r}_R) = \lim_{N\to\infty} \sum_{n=1}^{N} c_n e^{j\left(\beta_n + \vec{k}_T^{(n)} \cdot \vec{r}_T - \vec{k}_R^{(n)} \cdot \vec{r}_R - k_0 D_n\right)} \tag{6.1}$$

where c_n and β_n denote the gain and the phase shift introduced by the scatter $S^{(n)}$ respectively. Since $\delta_T \ll \min\{h_{T1}, h_{T2}\}$ holds, the waves emerging from different transmit antenna elements arrive at a particular scatter $S^{(n)}$ at approximately the same angle. Analogously, the waves emerging from a particular scatter $S^{(n)}$ arrive at different receive antenna elements at approximately the same angle, since $\delta_R \ll$

$\min\{h_{R1}, h_{R2}\}$. The gain c_n is assumed to be constant and given by

$$c_n = \sqrt{\frac{2\sigma_0^2}{N}} \tag{6.2}$$

where $2\sigma_0^2$ is the mean power of the received scattered components. Furthermore, it is assumed that the phase shifts β_n are independent, identically distributed (i.i.d.) random variables, each having a uniform distribution over the interval $[0, 2\pi)$.

The second phase component in (6.1), $\vec{k}_T^{(n)} \cdot \vec{r}_T$, expresses the influence of the transmitter movement on the channel gain. The symbol $\vec{k}_T^{(n)}$ denotes the wave vector pointing in the propagation direction of the n^{th} transmitted plane wave, and $\vec{r}_T$ is the spatial translation vector of the transmitter. The scalar product $\vec{k}_T^{(n)} \cdot \vec{r}_T$ can be expressed as

$$\vec{k}_T^{(n)} \cdot \vec{r}_T = 2\pi f_{T_{\max}} \cos(\alpha_n - \psi_T)t \tag{6.3}$$

where $f_{T_{\max}} = v_T/\lambda$ stands for the maximum Doppler frequency due to the transmitter movement. The symbol v_T represents the transmitter speed, while λ denotes the wavelength.

The third phase component in (6.1), $\vec{k}_R^{(n)} \cdot \vec{r}_R$, expresses the influence of the receiver movement on the channel gain. The symbol $\vec{k}_R^{(n)}$ denotes the wave vector pointing in the propagation direction of the n^{th} received plane wave, and $\vec{r}_T$ is the spatial translation vector of the receiver. The scalar product $\vec{k}_R^{(n)} \cdot \vec{r}_R$ can be expressed as

$$\vec{k}_R^{(n)} \cdot \vec{r}_R = -2\pi f_{R_{\max}} \cos(\theta_n - \psi_R)t \tag{6.4}$$

where $f_{R_{\max}} = v_R/\lambda$ stands for the maximum Doppler frequency due to the receiver movement. The symbol v_R represents the receiver speed.

The term $k_0 D_n$ in (6.1) is due to the total travelled distance and can be expressed as

$$k_0 D_n = \frac{2\pi}{\lambda}\left(D_T^{(l,n)} + D_R^{(n,k)}\right) \tag{6.5}$$

where $D_T^{(l,n)}$ denotes the distance from the l^{th} transmit antenna element $A_T^{(l)}$ to the scatter $S^{(n)}$, while $D_R^{(n,k)}$is the distance between the scatter $S^{(n)}$ to the k^{th} receive antenna element $A_R^{(k)}$. The assumptions $(M_T-1)\,\delta_T \ll \min\{h_{T1}, h_{T2}\}$, $(M_R-1)\delta_R \ll \min\{h_{R1}, h_{R2}\}$, and $\sqrt{1+x} \approx 1+x/2$ $(x \ll 1)$ allow us to approximate the previously described distances as follows:

$$D_T^{(l,n)} \approx D_T^{(n)} - (M_T - 2l + 1)\frac{\delta_T}{2}\cos(\alpha_n - \gamma_T) \tag{6.6}$$

$$D_R^{(n,k)} \approx D_R^{(n)} - (M_R - 2k + 1)\frac{\delta_R}{2}\cos(\theta_n - \gamma_R) \tag{6.7}$$

where $D_T^{(n)}$ and $D_R^{(n)}$correspond to the distances shown in Figure.6.1. The quantity $D_T^{(n)}$ is given by $D_T^{(n)} = h_{T1}/\sin(\alpha_n)$ whereas $D_R^{(n)}$ is given by $D_R^{(n)} = h_{R1}/\sin(\theta_n)$.

After substituting (6.2)–(6.5) in (6.1) and using the approximations in (6.6) and (6.7), the complex channel gain in $g_{kl}(t)$ can be expressed as

$$g_{kl}(t) = \lim_{N\to\infty}\sqrt{\frac{2\sigma_0^2}{N}}\sum_{n=1}^{N} d_n a_{ln} b_{kn} e^{j\left(2\pi(f_T^{(n)}+f_R^{(n)})t+\beta_n\right)} \tag{6.8}$$

where

$$d_n = e^{-j\frac{2\pi}{\lambda}\left(\frac{h_{T1}}{\sin(\alpha_n)}+\frac{h_{R1}}{\sin(\theta_n)}\right)} \tag{6.9}$$

$$a_{ln} = e^{j\pi\frac{\delta_T}{\lambda}(M_T-2l+1)\cos(\alpha_n-\gamma_T)} \tag{6.10}$$

$$b_{kn} = e^{j\pi\frac{\delta_R}{\lambda}(M_R-2k+1)\cos(\theta_n-\gamma_R)} \tag{6.11}$$

$$f_T^{(n)} = f_{T_{\max}}\cos(\alpha_n - \psi_T) \tag{6.12}$$

$$f_R^{(n)} = f_{R_{\max}}\cos(\theta_n - \psi_R). \tag{6.13}$$

The AOA θ_n can be expressed in terms of the AOD α_n according to (2.1). In fact, this relation has been developed for a SISO channel, although still hold for a MIMO channel. This statement results from the assumption that the waves emerging from different transmit antenna elements arrive at a particular scatter $S^{(n)}$ at approximately the same angle , since $\delta_T \ll \min\{h_{T1}, h_{T2}\}$. Moreover, the waves

emerging from a particular scatter $S^{(n)}$ arrive at different receive antenna elements at approximately the same angle, since $\delta_R \ll \min\{h_{R1}, h_{R2}\}$.

After studying the statistical properties of the diffuse component in (6.8), it can be proven that the mean value and the mean power of $g_{kl}(t)$ are equals to 0 and $2\sigma_0^2$, respectively. Hence, invoking the central limit theorem, we can conclude that the envelop $|g_{kl}(t)|$ follows a Rayleigh distribution.

By combining all the diffuse components $g_{kl}(t)$ $(k = 1, ..., M_R; l = 1, ..., M_T)$ of the $A_T^{(l)} - A_R^{(k)}$ link, we obtain the channel matrix $\mathbf{G}(t) := [g_{kl}(t)]$, which describes the reference model of the proposed M2M MIMO frequency-nonselective Rayleigh fading channel completely.

6.2.2 Correlation Functions of the Reference Model

The 3D space-time CCF of the links $A_T^{(l)} - A_R^{(k)}$ and $A_T^{(l')} - A_R^{(k')}$ is defined as the correlation between the channel gains $g_{kl}(t)$ and $g_{k'l'}(t)$ according to

$$\rho_{kl,k'l'}(\delta_T, \delta_R, \tau) := E\{g_{kl}^*(t) g_{k'l'}(t+\tau)\} \tag{6.14}$$

The expectation operator is first applied on the phase shifts β_n. This allow us to express the 3D space-time CCF as

$$\rho_{kl,k'l'}(\delta_T, \delta_R, \tau) = \lim_{N\to\infty} \frac{2\sigma_0^2}{N} \sum_{n=1}^{N} E\left\{ c_{ll'}^{(n)} d_{kk'}^{(n)} e^{j2\pi\left(f_T^{(n)} + f_R^{(n)}\right)\tau} \right\} \tag{6.15}$$

where

$$c_{ll'}^{(n)} = e^{j2\pi \frac{\delta_T}{\lambda}(l-l')\cos(\alpha_n - \gamma_T)} \tag{6.16}$$

$$d_{kk'}^{(n)} = e^{j2\pi \frac{\delta_R}{\lambda}(k-k')\cos(\theta_n - \gamma_R)} \tag{6.17}$$

and the quantities $f_T^{(n)}$ and $f_R^{(n)}$ are given by (6.12) and (6.13), respectively.

The expectation operator has now to be applied on the remaining random variables α_n. We remind that the AOA θ_n can be expressed in terms of the AOD α_n according

to (2.1). As the number of scatters tends to infinity the discrete random variables α_n and θ_n become continuous random variables denoted by α and θ, respectively. The AOA θ can be expressed in terms of α according to (2.1). The infinitesimal power of the diffuse component corresponding to the differential angle $d\alpha$ is proportional to $p_\alpha(\alpha)\, d\alpha$, where $p_\alpha(\alpha)$ denotes the distribution of α. As $N \to \infty$, this infinitesimal contribution must be equal to $1/N = p_\alpha(\alpha)\, d\alpha$. Consequently, it follows from (6.15) that the 3D space-time CCF of the reference model can be expressed as

$$\begin{aligned} \rho_{kl,k'l'}(\delta_T, \delta_R, \tau) &= \int_{\alpha_{\min}}^{\alpha_{\max}} c_{ll'}(\delta_T, \alpha) d_{kk'}(\delta_R, g(\alpha)) \\ &\quad 2\sigma_0^2 . e^{j2\pi(f_T(\alpha)+f_R(g(\alpha)))\tau} p_\alpha(\alpha)\, d\alpha \end{aligned} \tag{6.18}$$

where

$$c_{ll'}(\delta_T, \alpha) = e^{j2\pi \frac{\delta_T}{\lambda}(l-l')\cos(\alpha-\gamma_T)} \tag{6.19}$$

$$d_{kk'}(\delta_R, \theta) = e^{j2\pi \frac{\delta_R}{\lambda}(k-k')\cos(g(\alpha)-\gamma_R)} \tag{6.20}$$

$$f_T(\alpha) = f_{T_{\max}} \cos(\alpha - \psi_T) \tag{6.21}$$

$$f_R(g(\alpha)) = f_{R_{\max}} \cos(g(\alpha) - \psi_R). \tag{6.22}$$

The function $g(\alpha)$ expresses the relation between the AOA θ and the AOD α according to (2.1).

The temporal ACF of the channel gain $g_{kl}(t)$ is defined as $r_{g_{kl}}(\tau) := E\{g_{kl}^*(t) g_{k'l'}(t+\tau)\}$. The temporal ACF can be derived from the 3D space-time CCF by setting the antenna spacing to zero, i.e.,

$$\begin{aligned} r_{g_{kl}}(\tau) &= \rho_{kl,k'l'}(0, 0, \tau) \\ &= 2\sigma_0^2 \int_{\alpha_{\min}}^{\alpha_{\max}} e^{j2\pi(f_T(\alpha)+f_R(g(\alpha)))\tau} p_\alpha(\alpha)\, d\alpha. \end{aligned} \tag{6.23}$$

It has to be mentioned that the temporal ACFs $r_{g_{kl}}(\tau)$ of the channel gains $g_{kl}(t)$ are identical for all links $A_T^{(l)} - A_R^{(k)}$. This statement holds also for the one-ring model presented in [15] as well as for the elliptical model in [22].

The 2D space-time CCF $\rho_{kl,k'l'}(\delta_T, \delta_R)$ is defined as $\rho_{kl,k'l'}(\delta_T, \delta_R) := E\{g_{kl}^*(t) g_{k'l'}(t)\}$, which is equal to the 3D space-time CCF $\rho_{kl,k'l'}(\delta_T, \delta_R, \tau)$ by setting τ to zero, i.e., $\rho_{kl,k'l'}(\delta_T, \delta_R) = \rho_{kl,k'l'}(\delta_T, \delta_R, 0)$. Therefore,

$$\begin{aligned} \rho_{kl,k'l'}(\delta_T, \delta_R) &= 2\sigma_0^2 \int_{\alpha_{\max}}^{\alpha_{\max}} c_{ll'}(\delta_T, \alpha) \\ &\quad d_{kk'}(\delta_R, g(\alpha)) p_\alpha(\alpha)\, d\alpha. \end{aligned} \tag{6.24}$$

In case of isotropic scattering, the AOD are uniformly distributed over the interval $[\alpha_{\min}, \alpha_{\max}]$. Thus, the probability density function of the AOD is given by $p_\alpha(\alpha) = 1/\Delta\alpha$, where $\Delta\alpha = |\alpha_{\max} - \alpha_{\min}|$.

The common reference model described above is non-realizable since the number of scatters N is infinite. Nevertheless, the reference model constitutes the basis for the development of a simulation model, as we will see in the next section.

6.3 The Simulation Model

In this section, a stochastic simulation model is developed. Starting from the reference model and limiting the number of scatters N to a finite number, we can obtain a stochastic simulation model. The corresponding deterministic simulation model is obtained by fixing all model parameters. Finally, appropriate parameter computation methods are used to determine the model parameters, such that the statistical properties of the simulation model and the reference model fit together. This procedure is an application for the concept of deterministic channel modelling described in [14].

6.3.1 The Stochastic Simulation Model

A stochastic simulation model can be derived from the reference model by considering a finite number of scatters N. Thus, the diffuse component of the link $A_T^{(l)} - A_R^{(k)}$ can be expressed as

$$\hat{g}_{kl}(t) = \sqrt{\frac{2\sigma_0^2}{N}} \sum_{n=1}^{N} d_n a_{ln} b_{kn} e^{j\left(2\pi(f_T^{(n)} + f_R^{(n)})t + \beta_n\right)} \tag{6.25}$$

for $k = 1, ..., M_R$, $l = 1, ..., M_T$, where d_n, a_{ln}, b_{kn}, $f_T^{(n)}$ and $f_R^{(n)}$ are given by (6.9)–(6.13).

The phases β_n are still i.i.d. random variables, each with a uniform distribution on the interval $[0, 2\pi)$. The AODs α_n and the AOAs θ_n are constant. Therefore, $\hat{g}_{kl}(t)$ represents a stochastic process. The diffuse component $\hat{g}_{kl}(t)$ can be seen as a finite sum-of-sinusoids with constant gains, constant Doppler frequencies, and random phases. This category of stochastic processes is wide sense stationary and ergodic, as proven in Chapter 4.

The 3D space-time CCF between $\hat{g}_{kl}(t)$ and $\hat{g}_{k'l'}(t)$ is defined as

$$\hat{\rho}_{kl,k'l'}(\delta_T, \delta_R, \tau) := E\{\hat{g}_{kl}^*(t)\hat{g}_{k'l'}(t+\tau)\}. \tag{6.26}$$

By applying the expectation operator on the random phases β_n, the 3D space-time CCF of the stochastic simulation model can expressed as

$$\begin{aligned} \hat{\rho}_{kl,k'l'}(\delta_T, \delta_R, \tau) &= \frac{2\sigma_0^2}{N} \sum_{n=1}^{N} d_{kk'}(\delta_R, g(\alpha_n)) \\ &\quad c_{ll'}(\delta_T, \alpha_n) e^{j2\pi(f_T(\alpha_n) + f_R(g(\alpha_n)))\tau}. \end{aligned} \tag{6.27}$$

The realization of the channel matrix, defined as $\hat{\mathbf{G}}(t) := [\hat{g}_{kl}(t)]$, is called *the stochastic simulation model* for an M2M MIMO frequency-nonselective Rayleigh fading channel.

6.3.2 The Deterministic Simulation Model

A sample function of the stochastic process $\hat{g}_{kl}(t)$ is obtained by choosing constant phases β_n, determined by the outcomes of a random generator with uniform distribution over $[0, 2\pi)$. To realize a stochastic process, an infinite number of sample functions is needed, which makes it non-realizable. We can cope with this problem, since we are dealing with an ergodic stochastic process. In such a situation, a single sample function denoted by $\tilde{g}_{kl}(t)$ is sufficient. Since $\tilde{g}_{kl}(t)$ is deterministic and time-variant, it follows that the channel matrix $\widetilde{\mathbf{G}}(t) := [\tilde{g}_{kl}(t)]$ is also deterministic and time-variant. The realization of $\widetilde{\mathbf{G}}(t)$ represents the *deterministic simulation model* for a M2M MIMO frequency-nonselective Rayleigh fading channel. Time averages has to be used in order to analyse the properties of the deterministic MIMO channel simulator. For instance, the 3D space-time CCF between $\tilde{g}_{kl}(t)$ and $\tilde{g}_{k'l'}(t)$ is defined as

$$\tilde{\rho}_{kl,k'l'}(\delta_T, \delta_R, \tau) := \langle \tilde{g}^*_{kl}(t) \tilde{g}_{k'l'}(t+\tau) \rangle \tag{6.28}$$

It can be proven that (6.28) results in

$$\tilde{\rho}_{kl,k'l'}(\delta_T, \delta_R, \tau) = \hat{\rho}_{kl,k'l'}(\delta_T, \delta_R, \tau) \tag{6.29}$$

where $\hat{\rho}_{kl,k'l'}(\delta_T, \delta_R, \tau)$ is the 3D space-time CCF of *the stochastic simulation model* given by (6.27). Hence, the proposed MIMO channel simulator is ergodic with respect to the 3D space-time CCF.

The 2D space-time CCF $\tilde{\rho}_{kl,k'l'}(\delta_T, \delta_R)$ is defined as

$$\tilde{\rho}_{kl,k'l'}(\delta_T, \delta_R) := \langle \tilde{g}^*_{kl}(t) \tilde{g}_{k'l'}(t) \rangle \,. \tag{6.30}$$

Moreover, the temporal ACF of the deterministic process $\tilde{g}_{kl}(t)$ can be determined as

$$\begin{aligned} \tilde{r}_{g_{kl}}(\tau) &:= \langle \tilde{g}_{kl}^{*}(t)\tilde{g}_{kl}(t+\tau)\rangle \\ &= \frac{2\sigma_0^2}{N}\sum_{n=1}^{N} e^{j2\pi(f_T(\alpha_n)+f_R(g(\alpha_n)))\tau}. \end{aligned} \tag{6.31}$$

6.3.3 Parameter Computation Method

In the simulation model, the Doppler gains have the same expression as in the reference model, and are given by (6.2). Then, the only parameters to be determined are the Doppler frequencies. The latter are closely related to the AOAs and AODs. Since the AOAs can be expressed in terms of the AODs, we need to focus on the computation of the AODs $\alpha_n\,(n = 1,\ ...,\ N)$. In order to evaluate the set of AOD $\{\alpha_n\}_{n=1}^{N}$, we use first the Modified Method of Equal Area and then the *Lp*-norm method (LPNM).

6.3.3.1 Modified Method of Equal Area

The method of equal area (MEA) has been described in detail in [14]. To determine the value of the AODs α_n for the simulation model, let consider the PDF $p_\alpha(\alpha)$ of the AOD α given by

$$p_\alpha(\alpha) = \begin{cases} \dfrac{1}{\Delta\alpha} & \text{if } \alpha_{\min} \le \alpha \le \alpha_{\max} \\ 0 & \text{otherwise.} \end{cases} \tag{6.32}$$

To determine the value of the model parameters α_n, we divide the area under the PDF into N equal areas. This could be done by evaluating the set of AODs $\{\alpha_n\}_{n=1}^{N}$ in such a way that

$$\int_{\alpha_{\min}}^{\alpha_n} p_\alpha(\alpha)d\alpha = \frac{1}{\Delta\alpha}\frac{n}{N}, \qquad \forall n = 1,\ 2,\ ...,\ N \tag{6.33}$$

The Modified MEA is similar to the MEA method except the fact that we have to divide the area under the PDF into $2N$ subarea. Only the odd AOD will be used in the simulation model i.e.,

$$\int_{\alpha_{\min}}^{\alpha_n} p_\alpha(\alpha)d\alpha = \frac{1}{\Delta\alpha}\frac{(2n-1)}{2N}, \qquad \forall n = 1,\ 2,\ ...,\ N. \tag{6.34}$$

Hence, the model parameters can be expressed as

$$\alpha_n = \frac{\Delta\alpha}{N}(n - \frac{1}{2}) + \alpha_{\min}, \qquad \forall n = 1,\ 2,\ ...,\ N. \tag{6.35}$$

6.3.3.2 *Lp*-Norm Method (LPNM)

The LPNM has been described in detail in [14]. To determine the set of AOD $\{\alpha_n\}_{n=1}^{N}$ using the LPNM method, It is required to minimize the following error norm:

$$E_1^{(p)} := \left\{ \frac{1}{\tau_{\max}} \int_0^{\tau_{\max}} |r_{g_{kl}}(\tau) - \tilde{r}_{g_{kl}}(\tau)|^p \, d\tau \right\}^{1/p} \tag{6.36}$$

$$E_2^{(p)} := \left\{ \frac{1}{\delta_{T_{\max}}\delta_{R_{\max}}} \int_0^{\delta_{T_{\max}}} \int_0^{\delta_{R_{\max}}} \left|\rho_{kl,k'l'}(\delta_T, \delta_R) - \tilde{\rho}_{kl,k'l'}(\delta_T, \delta_R)\right|^p d\delta_T d\delta_R \right\}^{1/p} \tag{6.37}$$

where $p = 1, 2, ...$, while the quantities $\tau_{\max}, \delta_{T_{\max}}$ and $\delta_{R_{\max}}$ determine the maximum range over which the approximations $r_{g_{kl}}(\tau) \approx \tilde{r}_{g_{kl}}(\tau)$ and $\rho_{kl,k'l'}(\delta_T, \delta_R) \approx \tilde{\rho}_{kl,k'l'}(\delta_T, \delta_R)$ are of interest.

To optimize the model parameters $\alpha_n (n = 1,\ 2,\ ...,\ N)$, two ways could be used. One way is to use the Fletcher-Powell algorithm [26] to perform a joint distribution of both error norms $E_1^{(p)}$ and $E_2^{(p)}$. Another way consists in replacing α_n in (6.31) by α'_n, which allows the minimization of the error norms $E_1^{(p)}$ and $E_2^{(p)}$ independently. The latter alternative is applied in order to assess the performance of the proposed

M2M MIMO channel simulator. It is worth mentioning that the LPNM has been successfully used for the one-ring model[15], and the two-ring model[21].

6.4 Performance Evaluation and Simulation Results

The channel simulator has as a purpose to emulate the statistical fading behaviour of the M2M MIMO channel with a great deal of precision. The performance of the channel simulator can be assessed through the comparison of its statistical properties to those of the reference model. The ACF and the 2D space CCF can be considered as suitable statistical quantities for this assessment.

In order to illustrate the performance of our channel simulator, we consider two simulation scenarios. In the first scenario we assign to the variables $\alpha_{\max}$, L, h_{T1}, h_{R1}, D, σ_0^2, ψ_R, ψ_T, γ_T, γ_R ,$f_{T\max}$, $f_{R\max}$ the values $\pi/2$, 10m, 5m, 5m, 5m, 0.5, 0, 0, $\pi/2$, $\pi/2$, $91Hz$, $91Hz$, respectively.

Figure.6.2 illustrates both the ACF of the reference model ($r_{g_{11}}(\tau)$) and the ACF of the simulation model ($\tilde{r}_{g_{11}}(\tau)$). The MMEA method is used to optimize the simulation model parameters, where $N = 25$, and $\tau_{\max} = 0.06\ s$. A good fitting between the two ACFs can be observed. Moreover, Figure.6.2 demonstrates that the actual simulation results match with the theoretical results of $\tilde{r}_{g_{11}}(\tau)$ according to (6.31).

In Figure.6.3, the Lp-norm method is used to optimize the simulation model parameters by minimizing the error norm $E_1^{(p)}$, where $N = 25$, $p = 2$, and $\tau_{\max} = 0.06\ s$. A good fitting between the ACF of the reference model ($r_{g_{11}}(\tau)$) and the ACF of the simulation model ($\tilde{r}_{g_{11}}(\tau)$) can be observed. The Lp-norm method results in better fitting than the MMEA.

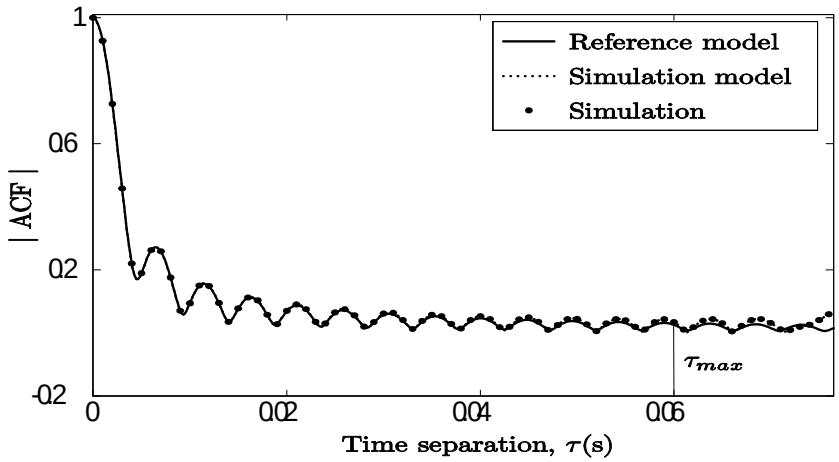

Figure 6.2: Time ACFs $r_{g_{11}}(\tau)$ (reference model) and $\tilde{r}_{g_{11}}(\tau)$ (simulation model) with $N = 25$ (MMEA, $\tau_{\max} = 0.06\ s$, $f_{T\max} = f_{R\max} = 91Hz$).

The 2D space CCF of the reference model $\rho_{11,22}(\delta_T, \delta_R)$ is evaluated according to (6.24), taking into account the parameters listed above. The obtained results are shown in Figure.6.4. The absolute error between the 2D space CCFs of the reference model ($\rho_{11,22}(\delta_T, \delta_R)$) and the simulation model ($\tilde{\rho}_{11,22}(\delta_T, \delta_R)$) is defined as $\varepsilon_{11,22}(\delta_T, \delta_R) = \left|\rho_{11,22}(\delta_T, \delta_R) - \tilde{\rho}_{11,22}(\delta_T, \delta_R)\right|$. In Figure.6.5, we illustrate the absolute error $\varepsilon_{11,22}(\delta_T, \delta_R)$, the shown results are obtained using the MMEA. The results obtained using the *Lp*-norm method are illustrated in Figure.6.6, the illustrated absolute error is obtained by minimizing the error norm $E_2^{(p)}$ using the *Lp*-norm method. A better fitting is obtained using the *Lp*-norm method. For this case the maximum absolute error is equal to 10^{-3} in the range $\delta_T = \delta_R = 3\lambda$.

In a second scenario, we just change the receiver antenna tilt γ_T to $\pi/4$. The obtained result for the 2D CCF are illustrated in Figure.6.7. In Figure.6.8, we illustrate the absolute error. In this case we use the MMEA to evaluate model parameters. In

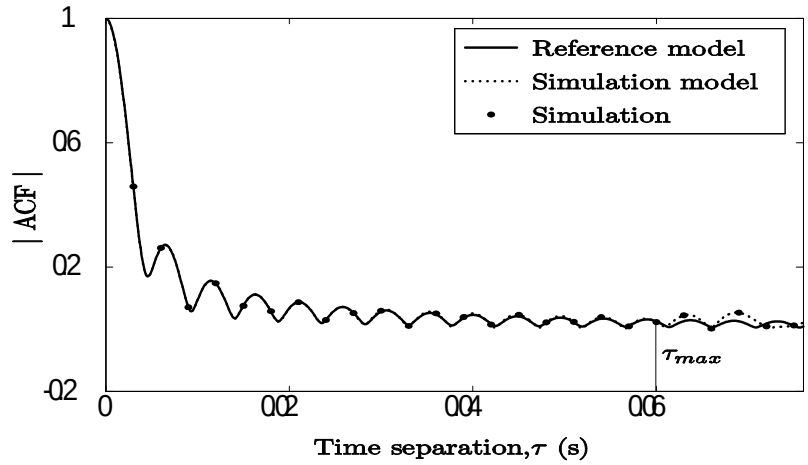

Figure 6.3: Time ACFs $r_{g_{11}}(\tau)$ (reference model) and $\tilde{r}_{g_{11}}(\tau)$ (simulation model) with $N = 25$ (Lp-norm method, $p = 2$, $\tau_{\max} = 0.06$ s, $f_{T\max} = f_{R\max} = 91Hz$).

Figure.6.9, we illustrate the absolute error. In this case we use the Lp-norm method to evaluate model parameters.

Consequently, the simulation model and the reference model have almost identical temporal and spatial correlation properties.

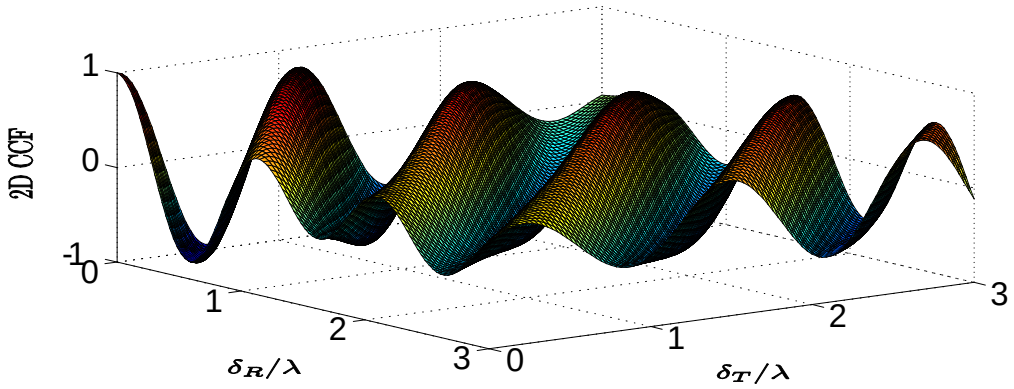

Figure 6.4: The 2D space CCF $\rho_{11,22}(\delta_T, \delta_R)$ of the reference model ($\gamma_T = \pi/2,\ \gamma_R = \pi/2$).

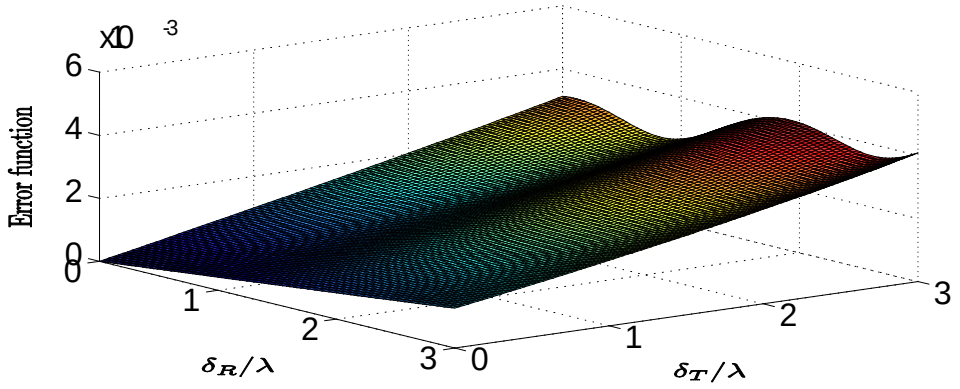

Figure 6.5: Absolute error $\varepsilon_{11,22}(\delta_T, \delta_R)$ (MMEA, $N = 25$, $\gamma_T = \pi/2,\ \gamma_R = \pi/2$).

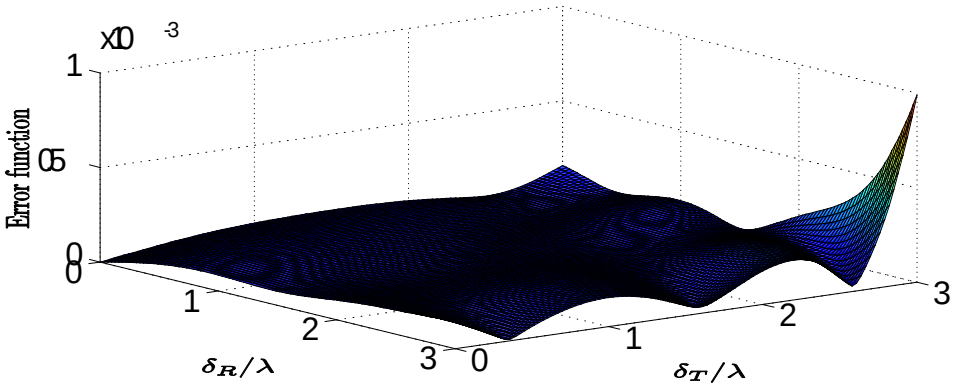

Figure 6.6: Absolute error $\varepsilon_{11,22}(\delta_T, \delta_R)$ (Lp-norm method, $N = 25$, $p = 2$, $\gamma_T = \pi/2, \gamma_R = \pi/2$).

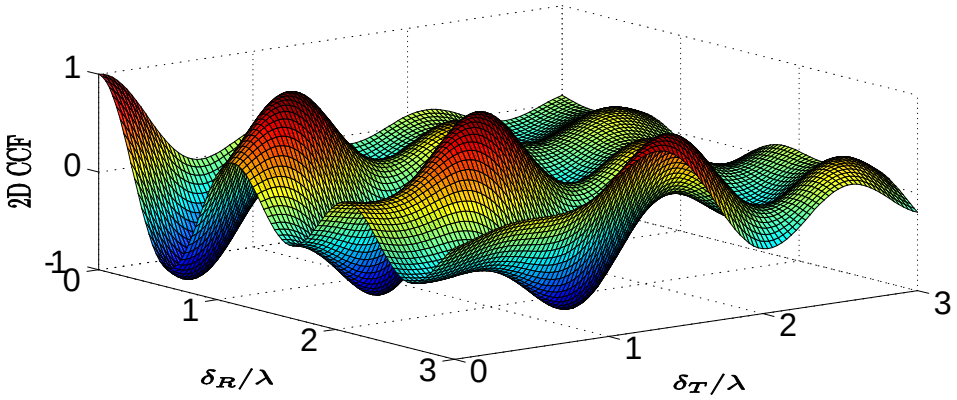

Figure 6.7: The 2D space CCF $\rho_{11,22}(\delta_T, \delta_R)$ of the reference model ($\gamma_T = \pi/2,\ \gamma_R = \pi/4$).

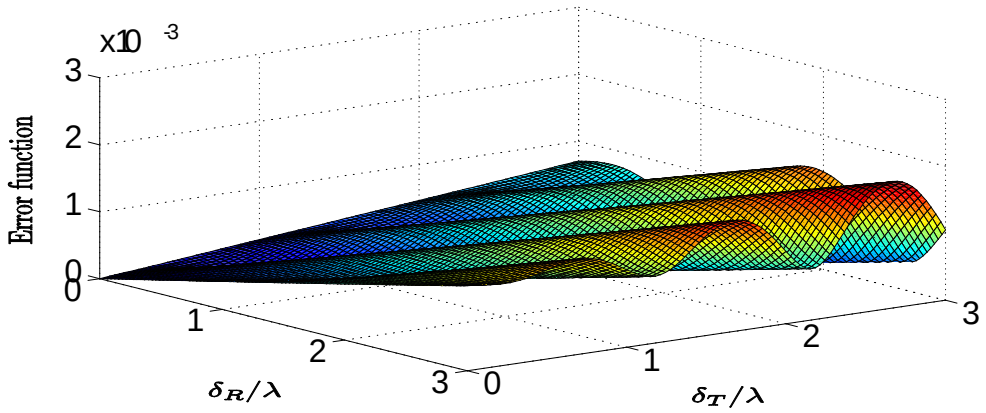

Figure 6.8: Absolute error $\varepsilon_{11,22}(\delta_T, \delta_R)$ (MMEA, $N = 25$, $\gamma_T = \pi/2, \gamma_R = \pi/4$).

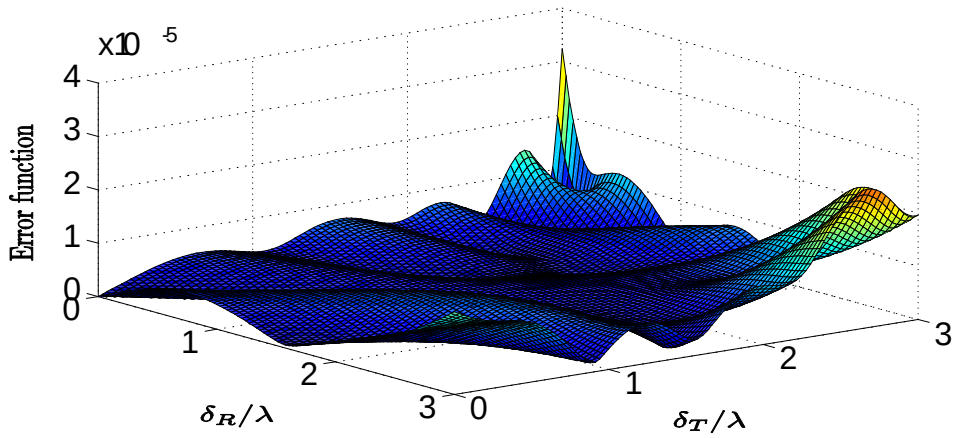

Figure 6.9: Absolute error $\varepsilon_{11,22}(\delta_T, \delta_R)$ (Lp-norm method, $N = 25$, $p = 2$, $\gamma_T = \pi/2, \gamma_R = \pi/4$).

Chapter 7

Conclusions

In this thesis, an original narrowband M2M SISO channel model has been derived starting from an authentic geometric street scattering model. The reference model for the M2M SISO channel and the corresponding simulation model have been developed in this thesis. We have studied the statistical properties of the reference and simulation model. The performance of the developed channel simulator has been assed by comparing the statistical properties of both the simulation and the reference model. The quality of the provided channel simulator has been proved.

Moreover, the M2M SISO channel model has been extended to an M2M MIMO channel model. Starting from the reference model of the MIMO channel where an infinite number of scatters is assumed, the simulation model has been derived using the generalized concept of deterministic channel modelling. The performance of the MIMO channel simulator has been assessed through the comparison of its statistical properties of the simulation model and the reference model. It has been shown that the proposed channel simulator emulates the behaviour of the underlying fading channel with a great deal of precision.

Moreover, the proposed channel simulators are very useful for the test, design, and analysis of futurist inter-vehicle communication systems.

The presented MIMO channel can be extended with respect to multi-cluster and frequency selectivity. In addition, the capacity of the proposed channel model can be studied.

Appendix A
Relation Between the AOD and the AOA

In this appendix, the exact relationship between the AOA and the AOD is derived, by considering the location of the scattering object and geometrical properties. The position of the scattering object has a direct influence on this relationship. In fact, three cases have to be distinguished. The first case corresponds to the situation where the scattering object is located behind the transmitter and the receiver. The second case corresponds to the situation where the scattering object is between the transmitter and the receiver. The third case corresponds to the situation where the scattering object is in front of the transmitter and the receiver. Moreover, for each of the three mentioned cases, we have to distinguish between two situations. In the first situation, the scatter is on the left hand side of the street. In the second situation, the scatter is on the right hand side of the street.

A.1 Scattering Object Located Behind the Transmitter and the Receiver

This case corresponds to the situation where the scattering object is located behind the transmitter and the receiver. We first consider the situation where the scatter $S^{(n)}$ is on the left hand side of the street, as shown in Figure.A.1.

Based on Figure.A.1, the AOA θ_n can be expressed in terms of the AOD α_n and vice versa. We start first by expressing the AOA θ_n in terms of the AOD α_n. The angle β_n, illustrated in Figure.A.1, is supplementary to θ_n, then $\tan(\theta_n) = -\tan(\beta_n)$.

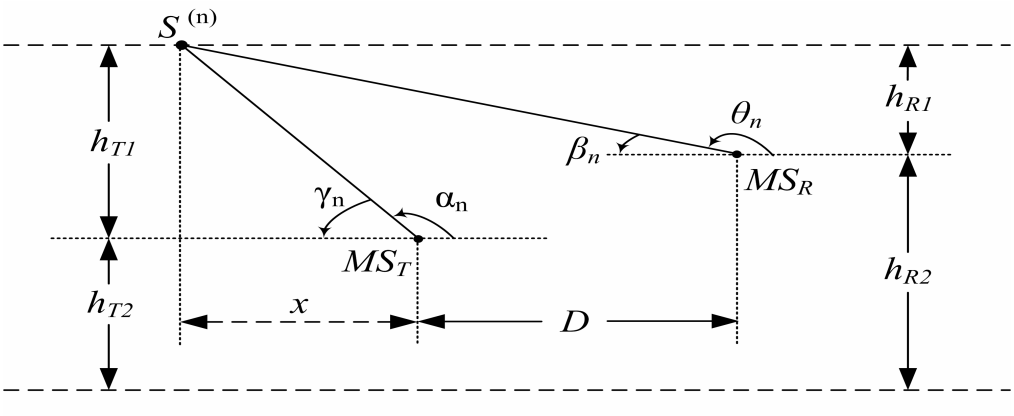

Figure A.1: Scenario of scatter behind the transmitter and the receiver on the left hand side of the street.

Based on trigonometry rules, the quantity $\tan(\beta_n)$ can be expressed as $\tan(\beta_n) = h_{R1}/(D+x)$. On the other hand, the angles α_n and γ_n are supplementary, thus $\tan(\alpha_n) = -\tan(\gamma_n)$. In addition, the quantity $\tan(\gamma_n)$ can be expressed as $\tan(\gamma_n) = h_{T1}/x$, then $x = -h_{T1}/\tan(\alpha_n)$. Substituting x in the expression of $\tan(\beta_n)$, we obtain $\tan(\beta_n) = (h_{R1} \cdot \tan(\alpha_n)/(D \cdot \tan(\alpha_n) - h_{T1}))$. Hence, the AOA θ_n can be expressed in terms of α_n according to

$$\theta_n = \pi + \arctan\left(\frac{h_{R1} \cdot \tan(\alpha_n)}{h_{T1} - D \cdot \tan(\alpha_n)}\right). \tag{A.1}$$

Next, we express the AOD α_n in terms of the AOA θ_n. The amount $\tan(\gamma_n)$ is given by $\tan(\gamma_n) = h_{T1}/x$, while $\tan(\theta_n) = -h_{R1}/(D+x)$. Hence, $\tan(\gamma_n) = -h_{T1} \cdot \tan(\theta_n)/(D \cdot \tan(\theta_n) + h_{R1})$. Since α_n and γ_n are supplementary, then α_n can be expressed as

$$\begin{aligned} \alpha_n &= \pi - \arctan\left(\frac{-h_{T1} \cdot \tan(\theta_n)}{D \cdot \tan(\theta_n) + h_{R1}}\right) \\ &= \pi + \arctan\left(\frac{h_{T1} \cdot \tan(\theta_n)}{D \cdot \tan(\theta_n) + h_{R1}}\right). \end{aligned} \tag{A.2}$$

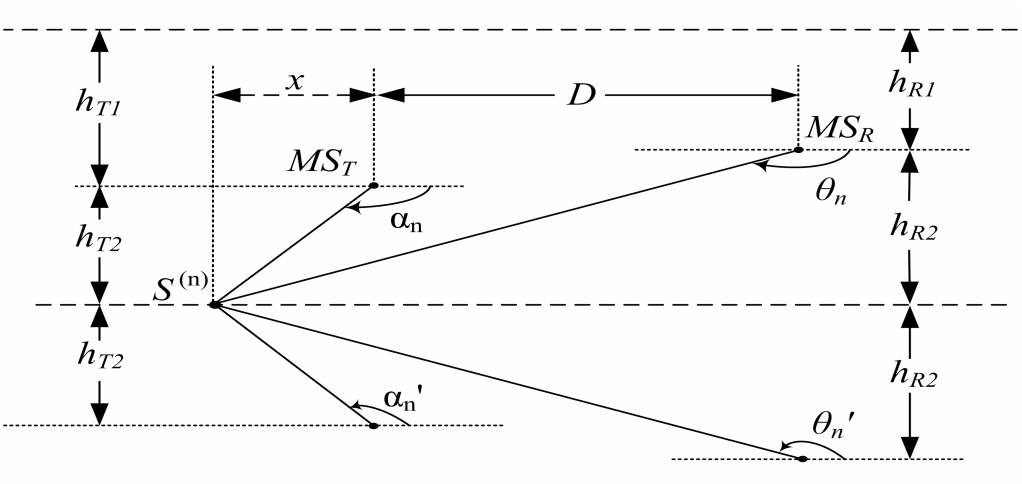

Figure A.2: Scenario of scatter behind the transmitter and the receiver on the right hand side of the street.

In Figure.A.2, the scatter $S^{(n)}$ is located on the right hand side of the street behind the transmitter and the receiver. Based on this figure, a relationship between the AOD α_n and the AOA θ_n can be established. The bottom part of Figure.A.2 is fictive, it is only depicted to show that this case is symmetric to the situation represented in Figure.A.1. In fact, the angles α_n and θ_n can be expressed as $\alpha_n = -\alpha_n'$ and $\theta_n = -\theta_n'$. The angle θ_n' can be expressed in terms of α_n' according to (A.1). Note that the terms $h_{T1}$and h_{R1} in (A.1) has to be replaced by h_{T2} and h_{R2}, respectively. Hence, we can write

$$\begin{aligned}
\theta_n &= -\theta_n' \\
&= -\pi - \arctan\left(\frac{h_{R2}\cdot\tan(\alpha_n')}{h_{T2} - D\cdot\tan(\alpha_n')}\right) \\
&= -\pi - \arctan\left(\frac{-h_{R2}\cdot\tan(\alpha_n)}{h_{T2} + D\cdot\tan(\alpha_n)}\right) \\
\theta_n &= -\pi + \arctan\left(\frac{h_{R2}\cdot\tan(\alpha_n)}{h_{T2} + D\cdot\tan(\alpha_n)}\right). \qquad \text{(A.3)}
\end{aligned}$$

In the same way, we can express the AOD α_n in terms of the AOA θ_n. The angle α'_n can be expressed in terms of the angle θ'_n according to (A.2). It is worth to mention that the terms h_{T1} and h_{R1} in (A.2) has to be replaced by h_{T2} and h_{R2}, respectively. Hence, we can write

$$\begin{aligned}
\alpha_n &= -\alpha'_n \\
&= -\pi - \arctan\left(\frac{h_{T2}\cdot\tan(\theta'_n)}{h_{R2}+D\cdot\tan(\theta'_n)}\right) \\
&= -\pi - \arctan\left(\frac{-h_{T2}\cdot\tan(\theta_n)}{h_{R2}-D\cdot\tan(\theta_n)}\right) \\
\alpha_n &= -\pi + \arctan\left(\frac{h_{T2}\cdot\tan(\theta_n)}{h_{R2}-D\cdot\tan(\theta_n)}\right). \qquad \text{(A.4)}
\end{aligned}$$

A.2Scattering Object Located Between the Transmitter and the Receiver

This case corresponds to the situation where the scattering object is located between the transmitter and the receiver. We first consider the situation where the scatter $S^{(n)}$ is on the left hand side of the street, as shown in Figure.A.3.

Based on Figure.A.3, the AOA θ_n can be expressed in terms of the AOD α_n and vice versa. We start first by expressing the AOA θ_n in terms of the AOD α_n. The angle β_n, illustrated in Figure.A.3, is supplementary to θ_n, then $\tan(\theta_n) = -\tan(\beta_n)$. Based on trigonometry rules, the quantity $\tan(\beta_n)$ can be expressed as $\tan(\beta_n) = h_{R1}/(D-x)$. On the other hand, $x = h_{T1}/\tan(\alpha_n)$.Substituting x in the expression of $\tan(\beta_n)$, we obtain $\tan(\beta_n) = (h_{R1}\cdot\tan(\alpha_n)/(D\cdot\tan(\alpha_n) - h_{T1}))$. Hence, the AOA θ_n can be expressed in terms of α_n as

$$\theta_n = \pi + \arctan\left(\frac{h_{R1}\cdot\tan(\alpha_n)}{h_{T1}-D\cdot\tan(\alpha_n)}\right) \qquad \text{(A.5)}$$

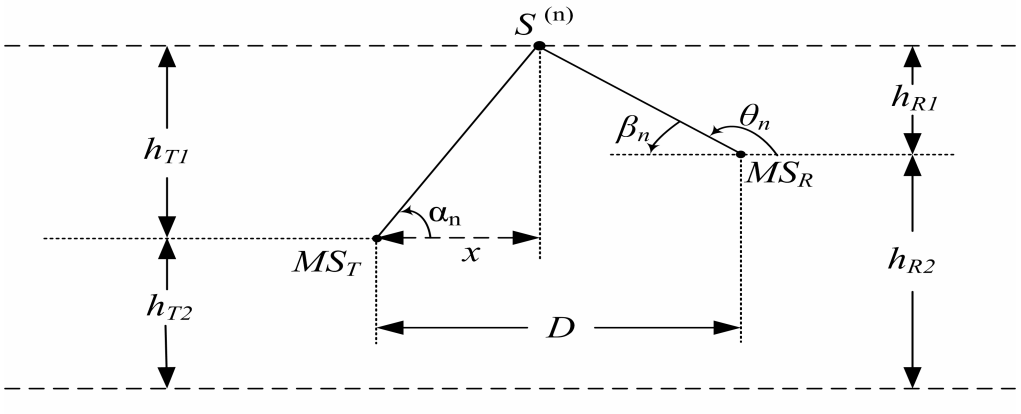

Figure A.3: Scenario of scatter between the transmitter and the receiver on the left hand side of the street.

Next, we express the AOD α_n in terms of the AOA θ_n. The amount $\tan(\alpha_n)$ is given by $\tan(\alpha_n) = h_{T1}/x$, while $\tan(\theta_n) = -h_{R1}/(D-x)$. Then, $\tan(\alpha_n) = h_{T1} \cdot \tan(\theta_n)/\left(D \cdot \tan(\theta_n) + h_{R1}\right)$. Hence, α_n can be expressed as

$$\alpha_n = \arctan\left(\frac{h_{T1} \cdot \tan(\theta_n)}{h_{R1} + D \cdot \tan(\theta_n)}\right) \tag{A.6}$$

In Figure.A.4, the scatter $S^{(n)}$ is located on the right hand side between the transmitter and the receiver. Based on this figure, a relationship between the AOD α_n and the AOA θ_n can be established. The bottom part of Figure.A.4 is fictive, it is only depicted to show that this case is symmetric to the situation represented in Figure.A.3. In fact, the angles α_n and θ_n can be expressed as $\alpha_n = -\alpha'_n$ and $\theta_n = -\theta'_n$. The angle θ'_n can be expressed in terms of α'_n according to (A.5), except that the terms $h_{T1}$and

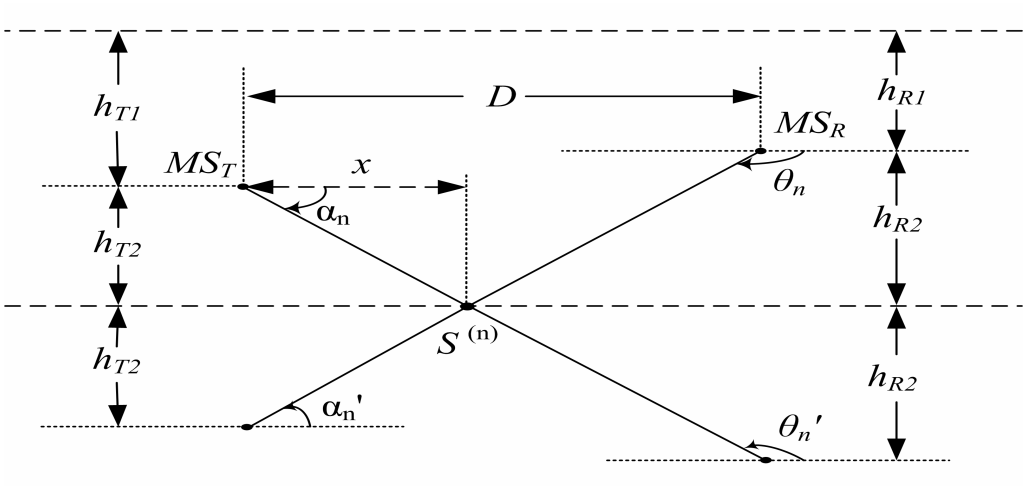

Figure A.4: Scenario of scatter between the transmitter and the receiver on the right hand side of the street.

h_{R1} has to be replaced by h_{T2} and h_{R2}, respectively. Hence, we can write

$$\begin{aligned}
\theta_n &= -\theta_n' \\
&= -\pi - \arctan\left(\frac{h_{R2}\cdot\tan(\alpha_n')}{h_{T2} - D\cdot\tan(\alpha_n')}\right) \\
&= -\pi - \arctan\left(\frac{-h_{R2}\cdot\tan(\alpha_n)}{h_{T2} + D\cdot\tan(\alpha_n)}\right) \\
\theta_n &= -\pi + \arctan\left(\frac{h_{R2}\cdot\tan(\alpha_n)}{h_{T2} + D\cdot\tan(\alpha_n)}\right) \qquad \text{(A.7)}
\end{aligned}$$

In the same way, we can express the AOD α_n in terms of the AOA θ_n. The angle α_n' can be expressed according to (A.6). It is worth to mention that the terms h_{T1}

and h_{R1} has to be replaced by h_{T2} and h_{R2}, respectively. Hence, we can write

$$\begin{aligned}
\alpha_n &= -\alpha'_n \\
&= -\arctan\left(\frac{h_{T2}\cdot\tan(\theta'_n)}{h_{R2}+D\cdot\tan(\theta'_n)}\right) \\
&= -\arctan\left(\frac{-h_{T2}\cdot\tan(\theta_n)}{h_{R2}-D\cdot\tan(\theta_n)}\right) \\
\alpha_n &= \arctan\left(\frac{h_{T2}\cdot\tan(\theta_n)}{h_{R2}-D\cdot\tan(\theta_n)}\right) \qquad \text{(A.8)}
\end{aligned}$$

A.3Scattering Object Located in Front of the Transmitter and the Receiver

This case corresponds to the situation where the scattering object is located in front of the transmitter and the receiver. We first consider the situation where the scatter $S^{(n)}$ is on the left hand side of the street, as shown in Figure.A.5.

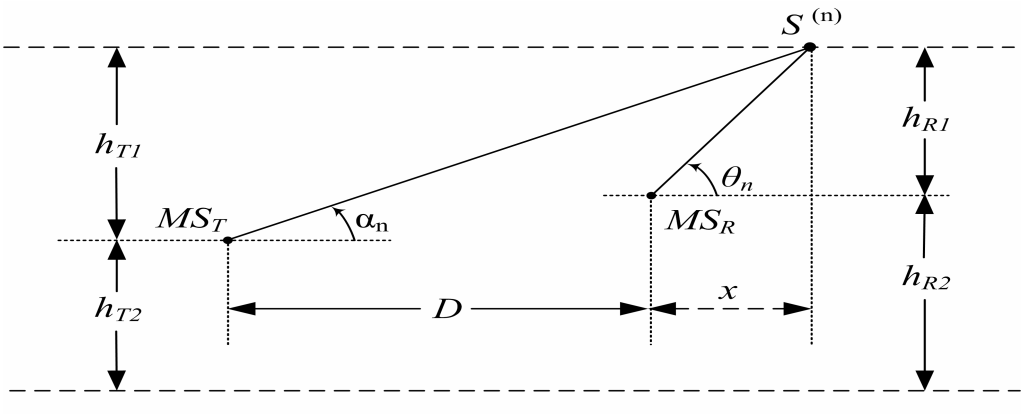

Figure A.5: Scenario of scatter in front of the transmitter and the receiver on the left hand side of the street.

Based on Figure.A.5, the AOA θ_n can be expressed in terms of the AOD α_n and vice versa. We start first by expressing the AOA θ_n in terms of the AOD α_n. Based on trigonometry rules, the quantity $\tan(\theta_n)$ can be expressed as $\tan(\theta_n) = h_{R1}/x$. On the other hand, the quantity $\tan(\alpha_n)$ can be expressed as $\tan(\alpha_n) = h_{T1}/(D + x)$. Substituting x in the expression of $\tan(\theta_n)$, we can express the AOA θ_n in terms of α_n as

$$\theta_n = \arctan\left(\frac{h_{R1} \cdot \tan(\alpha_n)}{h_{T1} - D \cdot \tan(\alpha_n)}\right) \tag{A.9}$$

The AOD α_n can be also expressed in terms of the AOA θ_n. The amount $\tan(\theta_n)$ is given by $\tan(\theta_n) = h_{R1}/x$, while $\tan(\alpha_n) = h_{T1}/(D + x)$. Hence, the AOD α_n can be expressed as

$$\alpha_n = \arctan\left(\frac{h_{T1} \cdot \tan(\theta_n)}{h_{R1} + D \cdot \tan(\theta_n)}\right) \tag{A.10}$$

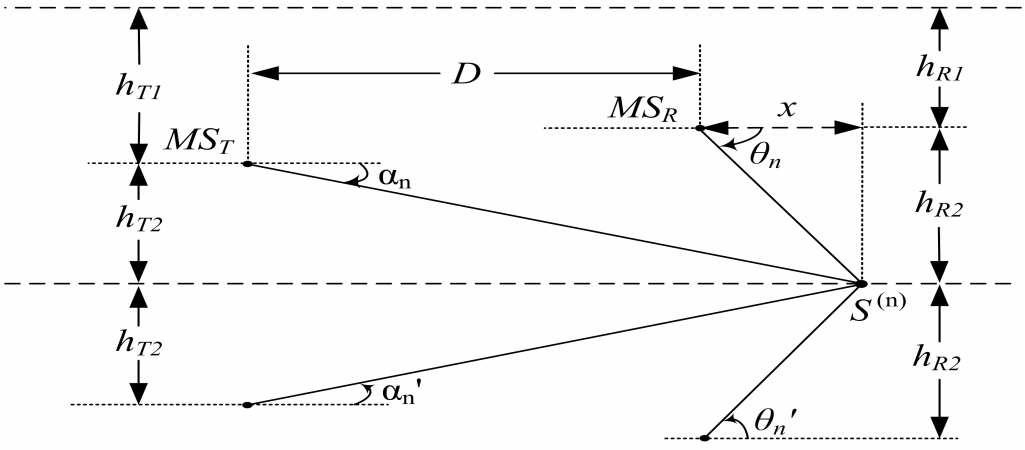

Figure A.6: Scenario of scatter in front of the transmitter and the receiver on the right hand side of the street.

in Figure.A.6, the scatter $S^{(n)}$ is located on the right hand side of the street in front of the transmitter and the receiver. Based on this figure, a relationship between α_n

and θ_n can be established. The bottom part of Figure.A.6 is fictive, it is only depicted to show that this case is symmetric to the situation represented in Figure.A.5. In fact, the angles α_n and θ_n can be expressed as $\alpha_n = -\alpha'_n$ and $\theta_n = -\theta'_n$. The angle θ'_n can be expressed in terms of α'_n according to (A.9). Note that the terms $h_{T1}$and h_{R1}, in (A.9), has to be replaced by h_{T2} and h_{R2}, respectively. Hence, we can write

$$\begin{aligned}
\theta_n &= -\theta'_n \\
&= -\arctan\left(\frac{h_{R2}\cdot\tan(\alpha'_n)}{h_{T2}-D\cdot\tan(\alpha'_n)}\right) \\
&= -\arctan\left(\frac{-h_{R2}\cdot\tan(\alpha_n)}{h_{T2}+D\cdot\tan(\alpha_n)}\right) \\
\theta_n &= \arctan\left(\frac{h_{R2}\cdot\tan(\alpha_n)}{h_{T2}+D\cdot\tan(\alpha_n)}\right)
\end{aligned} \tag{A.11}$$

In the same way, we can express the AOD α_n in terms of the AOA θ_n. The angle α'_n can be expressed according to (A.10). It is worth to mention that the terms h_{T1} and h_{R1} has to be replaced by h_{T2} and h_{R2}, respectively. Hence, we can write

$$\begin{aligned}
\alpha_n &= -\alpha'_n \\
&= -\arctan\left(\frac{h_{T2}\cdot\tan(\theta'_n)}{h_{R2}+D\cdot\tan(\theta'_n)}\right) \\
&= -\arctan\left(\frac{-h_{T2}\cdot\tan(\theta_n)}{h_{R2}-D\cdot\tan(\theta_n)}\right) \\
\alpha_n &= \arctan\left(\frac{h_{T2}\cdot\tan(\theta_n)}{h_{R2}-D\cdot\tan(\theta_n)}\right).
\end{aligned} \tag{A.12}$$

Hence, we can express the AOA θ_n in terms of the AOD α_n according to the relation

$$\theta_n = g(\alpha_n) = \begin{cases} -\pi + g_1(\alpha_n) & \text{if } -\pi \le \alpha_n \le -\arctan(\frac{h_{T2}}{D}) \\ g_1(\alpha_n) & \text{if} -\arctan(\frac{h_{T2}}{D}) \le \alpha_n \le 0 \\ g_2(\alpha_n) & \text{if } 0 \le \alpha_n \le \arctan(\frac{h_{T1}}{D}) \\ \pi + g_2(\alpha_n) & \text{if } \arctan(\frac{h_{T1}}{D}) \le \alpha_n \le \pi \end{cases} \tag{A.13}$$

where

$$g_1(\alpha_n) = \arctan\left(\frac{h_{R2}\cdot\tan(\alpha_n)}{h_{T2}+D\cdot\tan(\alpha_n)}\right) \tag{A.14}$$

$$g_2(\alpha_n) = \arctan\left(\frac{h_{R1}\cdot\tan(\alpha_n)}{h_{T1}-D\cdot\tan(\alpha_n)}\right) \tag{A.15}$$

while the AOD α_n can be expressed as

$$\alpha_n = h(\theta_n) = \begin{cases} -\pi + h_1(\theta_n) & \text{if } -\pi \le \theta_n \le -\pi + \arctan(\frac{h_{R2}}{D}) \\ h_1(\theta_n) & \text{if} -\pi + \arctan(\frac{h_{R2}}{D}) \le \theta_n \le 0 \\ h_2(\theta_n) & \text{if } 0 \le \theta_n \le \pi - \arctan(\frac{h_{R1}}{D}) \\ \pi + h_2(\theta_n) & \text{if } \pi - \arctan(\frac{h_{R1}}{D}) \le \theta_n \le \pi \end{cases} \tag{A.16}$$

where

$$h_1(\theta_n) = \arctan\left(\frac{h_{T2}\cdot\tan(\theta_n)}{h_{R2}-D\cdot\tan(\theta_n)}\right) \tag{A.17}$$

$$h_2(\theta_n) = \arctan\left(\frac{h_{T1}\cdot\tan(\theta_n)}{h_{R1}+D\cdot\tan(\theta_n)}\right). \tag{A.18}$$

Appendix B
Derivation of the Probability Density Function of the AOA

The AOA θ_n can be expressed in terms of the AOD α_n as $\theta_n = g(\alpha_n)$ according to (2.1) on page (16). Based on this relationship and since the expression of the PDF of the AOD α_n is given by (3.11), then the PDF of the AOA θ_n denoted by $p_{\theta_n}(\theta_n)$ can be derived. Using the transformation of random variable fundamental theorem, it is possible to express $p_{\theta_n}(\theta_n)$ as

$$p_{\theta_n}(\theta_n) = \frac{p_{\alpha_n}(\alpha_i)}{|g'(\alpha_i)|} \tag{B.1}$$

where $g'(\alpha_n)$ denotes the derivative of $g(\alpha_n)$, and α_i is the root of the equation $\theta_n = g(\alpha_n)$. For all value of θ_n the equation $\theta_n = g(\alpha_n)$ has one solution. In fact, for each emitted wave we obtain only one received wave. The location of the scattering object influence the expression of the function $g(\alpha_n)$, hence we need to consider different cases for the derivation of the PDF $p_{\theta_n}(\theta_n)$of the AOA θ_n.

First, we consider the case where the scatter is behind the transmitter and the receiver and on the left hand side of the street as shown in Figure.A.1 on page 88. For this case, the AOA θ_n can then be expressed as $\theta_n = g(\alpha_n) = \pi + g_2(\alpha_n)$, where $g_2(\alpha_n)$ is given by equation (2.3). This function has one root given by $\alpha_1 = \pi + \arctan\left(h_{T1} \cdot \tan(\theta_n) / \left(h_{R1} + D \cdot \tan(\theta_n)\right)\right)$. The slope $g'(\alpha_n)$ can be evaluated as

follow

$$\begin{aligned} g'(\alpha_n) &= g_2'(\alpha_n) \\ &= \frac{d}{d\alpha_n}\left[\arctan\left(\frac{h_{R1}\cdot\tan(\alpha_n)}{h_{T1}-D\cdot\tan(\alpha_n)}\right)\right] \\ &= \frac{1}{1+\left(h_{R1}\cdot\tan(\alpha_n)/\left(h_{T1}-D\cdot\tan(\alpha_n)\right)\right)^2}\cdot\frac{\left(1+\tan^2(\alpha_n)\right)\cdot h_{R1}\cdot h_{T1}}{\left(h_{T1}-D\cdot\tan(\alpha_n)\right)^2} \\ g'(\alpha_n) &= \frac{\left(1+\tan^2(\alpha_n)\right)\cdot h_{R1}\cdot h_{T1}}{\left(h_{T1}-D\cdot\tan(\alpha_n)\right)^2+\left(h_{R1}\cdot\tan(\alpha_n)\right)^2}. \end{aligned} \tag{B.2}$$

Before evaluating the amount $g'(\alpha_1)$, it is worth to remind that $\tan(\alpha_1)$ is given by $\tan(\alpha_1) = \left(h_{T1}\cdot\tan(\theta_n)/\left(h_{R1}+D\cdot\tan(\theta_n)\right)\right)$. Hence, $g'(\alpha_1)$ can be evaluated as follow

$$\begin{aligned} g'(\alpha_1) &= \frac{\left(1+\tan^2(\alpha_1)\right)\cdot h_{R1}\cdot h_{T1}}{\left(h_{T1}-D\cdot\tan(\alpha_1)\right)^2+\left(h_{R1}\cdot\tan(\alpha_1)\right)^2} \\ &= \frac{\left[1+\left(\frac{h_{T1}\cdot\tan(\theta_n)}{h_{R1}+D\cdot\tan(\theta_n)}\right)^2\right]\cdot h_{R1}\cdot h_{T1}}{\left[h_{T1}-D\cdot\left(\frac{h_{T1}\cdot\tan(\theta_n)}{h_{R1}+D\cdot\tan(\theta_n)}\right)\right]^2+\left[h_{R1}\cdot\left(\frac{h_{T1}\cdot\tan(\theta_n)}{h_{R1}+D\cdot\tan(\theta_n)}\right)\right]^2} \\ &= \frac{\left[\left(h_{R1}+D\cdot\tan(\theta_n)\right)^2+\left(h_{T1}\cdot\tan(\theta_n)\right)^2\right]}{\left(1+\tan^2(\theta_n)\right)\cdot h_{R1}\cdot h_{T1}} \\ &= \frac{\cos^2(\theta_n)\left[\left(h_{R1}+D\cdot\tan(\theta_n)\right)^2+\left(h_{T1}\cdot\tan(\theta_n)\right)^2\right]}{h_{R1}\cdot h_{T1}} \\ g'(\alpha_1) &= \frac{\sin^2(\theta_n)\left[\left(h_{R1}\cdot\cot(\theta_n)+D\right)^2+h_{T1}^2\right]}{h_{R1}\cdot h_{T1}} \end{aligned} \tag{B.3}$$

Hence, for the case shown in Figure.A.1, the PDF of the AOA is given by

$$\begin{aligned} p_{\theta_n}(\theta_n) &= \frac{p_{\alpha_n}(\alpha_1)}{|g'(\alpha_1)|} \\ &= \frac{1}{\Delta\alpha}\frac{h_{R1}\cdot h_{T1}}{\sin^2(\theta_n)\left[\left(h_{R1}\cdot\cot(\theta_n)+D\right)^2+h_{T1}^2\right]} \end{aligned} \tag{B.4}$$

Second, we consider the case where the scatter is behind the transmitter and the receiver and on the right hand side of the street as shown in Figure.A.2 on page 89. For this case, the AOA θ_n can then be expressed as $\theta_n = g(\alpha_n) = -\pi + g_1(\alpha_n)$, where $g_2(\alpha_n)$ is given by equation (2.2). This function has one root given by $\alpha_2 = -\pi + \arctan\left(h_{T2} \cdot \tan(\theta_n) / \left(h_{R2} - D \cdot \tan(\theta_n)\right)\right)$. The slope $g'(\alpha_n)$ is given by

$$g'(\alpha_n) = \frac{\left(1 + \tan^2(\alpha_n)\right) \cdot h_{R2} \cdot h_{T2}}{\left(h_{T2} + D \cdot \tan(\alpha_n)\right)^2 + \left(h_{R2} \cdot \tan(\alpha_n)\right)^2} \tag{B.5}$$

; hence, the amount $g'(\alpha_2)$ can be expressed as

$$g'(\alpha_2) = \frac{\sin^2(\theta_n)\left[\left(h_{R2} \cdot \cot(\theta_n) - D\right)^2 + h_{T2}^2\right]}{h_{R2} \cdot h_{T2}}. \tag{B.6}$$

Hence, for the case shown in Figure.A.2, the PDF of the AOA is given by

$$\begin{aligned} p_{\theta_n}(\theta_n) &= \frac{p_{\alpha_n}(\alpha_2)}{|g'(\alpha_2)|} \\ &= \frac{1}{\Delta\alpha} \frac{h_{R2} \cdot h_{T2}}{\sin^2(\theta_n)\left[\left(h_{R2} \cdot \cot(\theta_n) - D\right)^2 + h_{T2}^2\right]} \end{aligned} \tag{B.7}$$

Afterward, we consider the case where the scatter is between the transmitter and the receiver and on the left hand side of the street as shown in Figure.A.3 on page 91. For this case, the AOA θ_n can then be expressed as $\theta_n = g(\alpha_n) = \pi + g_2(\alpha_n)$. This function has one root given by $\alpha_3 = \arctan\left(h_{T1} \cdot \tan(\theta_n) / \left(h_{R1} + D \cdot \tan(\theta_n)\right)\right)$. The slope $g'(\alpha_n)$ is given by

$$g'(\alpha_n) = \frac{\left(1 + \tan^2(\alpha_n)\right) \cdot h_{R1} \cdot h_{T1}}{\left(h_{T1} - D \cdot \tan(\alpha_n)\right)^2 + \left(h_{R1} \cdot \tan(\alpha_n)\right)^2} \tag{B.8}$$

; hence, the amount $g'(\alpha_3)$ can be expressed as

$$g'(\alpha_3) = \frac{\sin^2(\theta_n)\left[\left(h_{R1} \cdot \cot(\theta_n) + D\right)^2 + h_{T1}^2\right]}{h_{R1} \cdot h_{T1}}. \tag{B.9}$$

Hence, for the case shown in Figure.A.3, the PDF of the AOA is given by

$$\begin{aligned} p_{\theta_n}(\theta_n) &= \frac{p_{\alpha_n}(\alpha_3)}{|g'(\alpha_3)|} \\ &= \frac{1}{\Delta\alpha} \frac{h_{R1} \cdot h_{T1}}{\sin^2(\theta_n)\left[(h_{R1} \cdot \cot(\theta_n) + D)^2 + h_{T1}^2\right]} \end{aligned} \tag{B.10}$$

Now, we consider the case where the scatter is between the transmitter and the receiver and on the right hand side of the street as shown in Figure.A.4 on page 92. For this case, the AOA θ_n can then be expressed as $\theta_n = g(\alpha_n) = -\pi + g_1(\alpha_n)$. This function has one root given by $\alpha_4 = \arctan\left(h_{T2} \cdot \tan(\theta_n) / \left(h_{R2} - D \cdot \tan(\theta_n)\right)\right)$. The slope $g'(\alpha_n)$ is given by

$$g'(\alpha_n) = \frac{(1 + \tan^2(\alpha_n)) \cdot h_{R2} \cdot h_{T2}}{(h_{T2} + D \cdot \tan(\alpha_n))^2 + (h_{R2} \cdot \tan(\alpha_n))^2} \tag{B.11}$$

; hence, the amount $g'(\alpha_4)$ can be expressed as

$$g'(\alpha_4) = \frac{\sin^2(\theta_n)\left[(h_{R2} \cdot \cot(\theta_n) - D)^2 + h_{T2}^2\right]}{h_{R2} \cdot h_{T2}}. \tag{B.12}$$

Hence, for the case shown in Figure.A.4, the PDF of the AOA is given by

$$\begin{aligned} p_{\theta_n}(\theta_n) &= \frac{p_{\alpha_n}(\alpha_4)}{|g'(\alpha_4)|} \\ &= \frac{1}{\Delta\alpha} \frac{h_{R2} \cdot h_{T2}}{\sin^2(\theta_n)\left[(h_{R2} \cdot \cot(\theta_n) - D)^2 + h_{T2}^2\right]} \end{aligned} \tag{B.13}$$

Let consider the case where the scatter is in front of the transmitter and the receiver and on the left hand side of the street as shown in Figure.A.5 on page 93. For this case, the AOA θ_n can then be expressed as $\theta_n = g(\alpha_n) = g_2(\alpha_n)$. This function has one root given by $\alpha_5 = \arctan\left(h_{T1} \cdot \tan(\theta_n) / \left(h_{R1} + D \cdot \tan(\theta_n)\right)\right)$. The slope $g'(\alpha_n)$ is given by

$$g'(\alpha_n) = \frac{(1 + \tan^2(\alpha_n)) \cdot h_{R1} \cdot h_{T1}}{(h_{T1} - D \cdot \tan(\alpha_n))^2 + (h_{R1} \cdot \tan(\alpha_n))^2} \tag{B.14}$$

; hence, the amount $g'(\alpha_5)$ can be expressed as

$$g'(\alpha_5) = \frac{\sin^2(\theta_n)\left[(h_{R1}\cdot\cot(\theta_n)+D)^2+h_{T1}^2\right]}{h_{R1}\cdot h_{T1}}. \tag{B.15}$$

Hence, for the case shown in Figure.A.5, the PDF of the AOA is given by

$$\begin{aligned} p_{\theta_n}(\theta_n) &= \frac{p_{\alpha_n}(\alpha_5)}{|g'(\alpha_5)|} \\ &= \frac{1}{\Delta\alpha}\frac{h_{R1}\cdot h_{T1}}{\sin^2(\theta_n)\left[(h_{R1}\cdot\cot(\theta_n)+D)^2+h_{T1}^2\right]} \end{aligned} \tag{B.16}$$

Finally, we consider the case where the scatter is in front of the transmitter and the receiver and on the right hand side of the street as shown in Figure.A.6 on page 94. For this case, the AOA θ_n can then be expressed as $\theta_n = g(\alpha_n) = g_1(\alpha_n)$. This function has one root given by $\alpha_6 = \arctan\left(h_{T2}\cdot\tan(\theta_n)/\left(h_{R2}-D\cdot\tan(\theta_n)\right)\right)$. The slope $g'(\alpha_n)$ is given by

$$g'(\alpha_n) = \frac{(1+\tan^2(\alpha_n))\cdot h_{R2}\cdot h_{T2}}{(h_{T2}+D\cdot\tan(\alpha_n))^2+(h_{R2}\cdot\tan(\alpha_n))^2} \tag{B.17}$$

; hence, the amount $g'(\alpha_5)$ can be expressed as

$$g'(\alpha_6) = \frac{\sin^2(\theta_n)\left[(h_{R2}\cdot\cot(\theta_n)-D)^2+h_{T2}^2\right]}{h_{R2}\cdot h_{T2}}. \tag{B.18}$$

Hence, for the case shown in Figure.A.6, the PDF of the AOA is given by

$$\begin{aligned} p_{\theta_n}(\theta_n) &= \frac{p_{\alpha_n}(\alpha_6)}{|g'(\alpha_6)|} \\ &= \frac{1}{\Delta\alpha}\frac{h_{R2}\cdot h_{T2}}{\sin^2(\theta_n)\left[(h_{R2}\cdot\cot(\theta_n)-D)^2+h_{T2}^2\right]} \end{aligned} \tag{B.19}$$

Finally, The PDF $p_{\theta_n}(\theta_n)$ of the AOA θ_n can be expressed as

$$p_{\theta_n}(\theta_n) = \begin{cases} \dfrac{1}{\Delta\alpha} \dfrac{h_{R2} \cdot h_{T2}}{\sin^2(\theta_n)\left[(h_{R2} \cdot \cot(\theta_n) - D)^2 + h_{T2}^2\right]} & \text{if} \quad -\pi \leq \theta_n \leq 0 \\ \dfrac{1}{\Delta\alpha} \dfrac{h_{R1} \cdot h_{T1}}{\sin^2(\theta_n)\left[(h_{R1} \cdot \cot(\theta_n) + D)^2 + h_{T1}^2\right]} & \text{if} \quad 0 \leq \theta_n \leq \pi. \end{cases} \tag{B.20}$$

ABBREVIATIONS

ACF	Autocorrelation Function
ADF	Average Duration of Fades
AOA	Angle of Arrival
AOD	Angle of Departure
DSRC	Dedicated Short Range Communication
FCC	Federal Communication Commission
ITS	Intelligent Transportation System
IVC	Inter-Vehicle Communications
LCR	Level Crossing Rate
LPNM	*Lp*-Norm Method
M2M	Mobile-to-Mobile
MAC	Medium Access layer
MIMO	Multi-Input Multi-Output
MMEA	Modified Method of Equal Area
NHTSA	National Highway Traffic Safety Administration
PDF	Probability Density Function
PHY	Physical layer
PSD	Power Spectral Density
SISO	Single-Input Single-Output
TCP	Transmission Control Protocol
UDP	User Datagram Protocol
USDOT	U.S. Department of Transportation
VSC	Vehicle Safety Communications
WAVE	Wireless Access for Vehicular Environment

Bibliography

[1] Peden, M., Scurfield, R., Sleet, D., Mohan, D., Hyder, A. A., Jarawan, E., Mathers, C., "World report on road traffic injury prevention," World Health Organization press, 2004.

[2] http://www.prevent-ip.org/.

[3] http://www.car-2-car.org/.

[4] http://www.its.dot.gov/.

[5] http://www-nrd.nhtsa.dot.gov/pdf/nrd-12/CAMP3/pages/VSCC.htm.

[6] Standard Specification for Telecommunications and Information Exchange Between roadside and Vehicle Systems- 5 GHz Band Dedicated Short Range Communications (DSRC) Medium Access Control (MAC) and Physical Layer (PHY) Specifications *ASTM E2213-03*, Sept. 2003.

[7] Wireless Access in Vehicular Environment (WAVE) in Standard 802.11 Information Technology Telecommunications and Information Exchange Between Systems, Local and Metropolitan Area Networks, Specific Requirements, Part 11: Wireless LAN Medium Access Control (MAC) and Physical Layer (PHY) Specifications, *IEEE 802.11p/D1.0,* Feb. 2006.

[8] Wireless Access in Vehicular Environments (WAVE) Channel Coordination, *IEEE P1609.4/D05,* Nov. 2005.

[9] Wireless Access in Vehicular Environments (WAVE) Networking Services, *IEEE P1609.3/D17,* Nov. 2005.

[10] Federal Communications Commission Amendment of the Commission's Rules Regarding Dedicated Short-Range Communication Services in the 5.850-5.925 GHz Band, *FCC 03-324. FCC Report and Order,* December 2003.

[11] R. B. Ertel, P. Cardieri, K. W. Sowerby, T. S. Rapport, and J. H. Reed, "Overview of spatial channel models for antenna array communication systems," *IEEE Personal Comm. Mag.(1998), 10-22.*

[12] J.J Blanz, P.W Baier, and P. Jung, "Aflexibely cofigurable statistical channel model for mobile radio systems with directional diversity," *Proc. 2nd ITG-Fachtagung Mobile communication'95*, Neu-Ulm, Germany, 1995, 93-100.

[13] M. Pätzold, U. Killat, F. Laue, and Y. Li, "On the statistical properties of deterministic simulation models for mobile fading channels," *IEEE Trans. Veh. Technol.,* vol. 47, no. 1, pp. 254–269, Feb. 1998.

[14] M. Pätzold, *Mobile Fading Channels.* Chichester: John Wiley& Sons, 2002.

[15] M. Pätzold and B. O. Hogstad, "A Space-time channel simulator for MIMO channels based on the geometrical one-ring scattering model," *Wireless Communication and Mobile Computing, Special Issue on Multiple-Input Multiple-Output (MIMO) Communications,* vol. 4, no. 7, pp. 727-737, Nov. 2004.

[16] A. S. Akki, and F.Haber "A statistical model of mobile-to-mobile land communication channels," *IEEE Trans. Veh. Technol.,* vol. 35, no. 1, pp. 2-7, Feb. 1986.

[17] A. S. Akki, "Statistical properties of mobile-to-mobile land communication channels," *IEEE Trans. Veh. Technol.,* vol. 43, November 1994.

[18] J. Maurer, T. Fügen, T. Schäfer, and W. Wiesbeck, "A new inter-vehicle communications (IVC) channel model," *IEEE Veh. Technol. Contf. (VTC'04),* Los Angeles, California, USA, Sept. 2004.

[19] C. S. Patel, G. L. Stüber, and T. G. Pratt, "Simulation of Rayleigh faded mobile-to-mobile communication channels," *in Proc. 58th IEEE Veh. Technol. Conf. (VTC'03),* Orlando, FL, USA. Oct. 2003., pp. 163-167.

[20] M. Pätzold, B. O. Hogstad, N. Youssef, and D. Kim, "A MIMO mobile-to-mobile channel model: Part I - The reference model," *in Proc. 16th IEEE Int. Symp. on Personal, Indoor and Mobile Radio Communications, PIMRC 2005,* Berlin, Germany, Sept. 2005.

[21] M. Pätzold, B. O. Hogstad, N. Youssef, and D. Kim, "A MIMO mobile-to-mobile channel model: Part II - The simulation model," *in Proc. 16th IEEE Int. Symp. on Personal, Indoor and Mobile Radio Communications, PIMRC 2005,* Berlin, Germany, Sept. 2005.

[22] M. Pätzold and B. O. Hogstad, "A wideband MIMO channel model derived from the geometric elliptical scattering model," *in Proc. 3rd Int. Symp. on Wireless Communication System, ISWCS'06, Valencia,* Spain, Sept. 2006, pp. 138–143.

[23] COST207: Proposal on channel transfer functions to be used in GSM testes late 1986. Tech. Rept. COST 207 TD(86)51 Rev. 3.COST, 1986.

[24] I. E. Telatar, "Capacity of multi-antenna Gaussian channels," *European Trans. Telecommun. Related Technol,* vol. 10, pp. 585-595, 1999.

[25] G. H. Foschini and M. J. Gans, "On limits of wireless communications in a fading environment when using multiple antennas," *Wireless Pers. Commun.,* vol. 6, pp. 311-335, 1998.

[26] R. Fletcher and M. J. D. Powell, "A rapidly convergent descent method for minimization," *Computer Journal,* vol. 6, no. 2, pp. 163–168, 1963.